Sensing water accumulation and transport in proton exchange membrane fuel cells with terahertz radiation

Decio Filipe Ferreira Alves de Lima

This Dissertation is submitted for the degree of **Doctor of Philosophy**

May 2022

Department of Engineering

Lancaster University

Dedicated to my son, Samuel

Copyright

Declaration

I declare that the work presented in this Dissertation is, to the best of my knowledge and belief, original and my own work. The material has not been submitted either in whole or in part, for any degree at this, or any other University. All major sources have been appropriately referenced.

X

Decio Alves de Lima

Acknowledgements

The path to completing a PhD degree is long, tumultuous, and certainly impossible to achieve without support and guidance from several people.

Primarily, I would like to express my sincere appreciation to my main supervisor Dr Hungyen Lin, for his strong introduction to the terahertz subject, tenacious enthusiasm, reassuring attitude, generous travel funding and various facilitated collaborations. Hungyen has had a major influence on my scientific career progress and is someone that I hold the utmost respect and gratitude for, as a true mentor. Secondly, I would like to express gratitude to my secondary supervisor, Dr Richard Dawson. I am truly honoured to have had the privilege of studying under Richard; his experience with fuel cells and general electrochemistry and his connections within the UK industry have been of immense importance to this PhD project. Richard's kindness and understanding were also major contributors to the realisation of this project and Dissertation, and I look forward to our continued collaborations at Lina Energy.

I would also like to acknowledge my third supervisor, Dr Rosa Letizia for kindly providing essential equipment for my research.

I would like to extend my appreciation to the staff of Lancaster University's Engineering Department. To the technical staff, Jonathan Gates, Joseph Cottam, Wellington Grosvenor, Malcolm Weightman, Nick Renninson, Peter Jones, Jess Fisher, Dr Ashley Jones, Mark Salisbury, Andrew Verden, Thomas Clayton and Andrew Baker for helpful discussions, valuable suggestions, part manufacturing and overall excellent support to my practical work throughout these years. A special word to Jono, Joe, and Mal for their friendship. To the administrative staff, Janet Wood, Kathryn Rucastle, Martin O'Connor, Laura Gracie and Rachael Venn for their kindness and assistance. Finally, I would like to the acknowledge the course supervisors and colleagues on the module that I tutored: Dr Vesna Najdanovic, Dr Tim Douglas, Dr Chris Tumilson and Mohamed Maher; it was great meeting and collaborating with you all.

During my tenure as a PhD student, I had the opportunity to collaborate with industrial partners, external researchers, lecturers, postdocs, fellow PhD students and undergraduate students who left a positive impact on my PhD experience. I would like to first acknowledge my colleague Dr Xiaoran Li for his immense help and useful advice on Matlab code development, as well as his kindness, camaraderie, positivity, and light-hearted attitude. I would also like to thank Dr Gaurav Gupta for fruitful discussions and valuable feedback on the last months of my PhD. To my colleagues Jordan Frow and George Ludlam, I appreciate all the assistance, friendship, and

wish you the best of luck in your own PhD endeavours. I would especially like to acknowledge Dr Riccardo Degl'Innocenti and his research group including Dr Xavier Romain, Yuezhen Lu and Abdullah Zaman for the opportunity to use their terahertz spectrometer and other optical components, along with the warm friendship and good moments that we shared. A special mention to Dr Harald Schlegl and Dr Bryan Williams for their assistance with practical work on Chapter 5 of this Dissertation, as well as their warm friendship and lovely conversations we had across these years. I would like to also express gratitude to Dr David Chau, Dr Tim Douglas, Sonia Kudlacik-Kramarczyk and Anna Drabczyk for our fruitful collaborations. Many thanks to our industrial partners at Johnson Matthey Fuel Cells, namely Dr Massimo Peruffo, Dr Jonathan Sharman, Dr Bethan Coulson, Dr Emily Nesling for continued collaborations, fruitful discussions, sample provision and hosting at your facilities in Swindon, Wiltshire. I also greatly appreciate Dr Sebastian Engelbrecht for his patience and assistance at the French-German Institute of Saint Louis in France. I would also like to thank James Wroe, Karl Cooper, Alvira Kumar, David Dare and Keir White for the rewarding experience of supervising their Dissertation projects.

On a personal level, my gratitude goes primarily to Sara Jacinto. Sara has been a loving girlfriend and best friend for over 10 years. Without your love, compassion, advice, and companionship every single day of this journey, none of this would be possible. And to Samuel, our first born, to whom this work is dedicated, thank you for being the shining light in our lives. I would also like to say a heartfelt thank you to Mum, Dad, Rita, and Luis for always believing in me, respecting my choices, and allowing me to follow my dreams. Last, but certainly not least, my deep appreciation goes to my friends Dimitri Zografos and Dr Lee Sae Jin. Your love and friendship carried me through dark times and allowed me to build up the courage to never give up on what I started here. Without you, this PhD project would not have been completed and this Dissertation would have never been written.

Abstract

Fuel cells are like batteries in the sense that they are electrochemical cells whose main components are two electrodes (anode and cathode) and an electrolyte material. They differ from most batteries as they require a continuous stream of fuel and oxidant, generating electricity and heat for as long as these are supplied. Perfluorinated sulfonic-acid ionomers such as Nafion are the most common proton exchange membrane material (solid electrolyte) whose structure underpins its unique water and chemical/mechanical stability properties. Pure hydrogen and air are typically used as the fuel and oxidant, respectively, and by-products are water and waste heat. Due to their high efficiency, low temperature operation and capacity to quickly vary their output to meet shifting demands, these fuel cells are attractive to the automobile industry, although they can also be used for stationary power production.

Water management is a prominent issue in proton exchange membrane fuel cell technology. Strategies in this topic must maintain a delicate balance between adequate hydration levels in the Nafion proton electrolyte membrane to maximise proton conductivity, and minimal flooding, which hinders mass transport to active sites. The complex nature of water transport in these fuel cells can be investigated via in situ or ex situ diagnostics with visualisation techniques such as neutron imaging or optical diagnostics. Despite the wealth of information provided by these techniques, they suffer from issues such as limited availability, excessive cost, limited sensitivity, and penetration depth.

Terahertz radiation has been growing in popularity for contactless and non-destructive testing across various industrial sectors, including pharmaceutical coating analysis, defect identification, and gas pipeline monitoring. The ability of terahertz waves to penetrate through dielectric materials such as plastics or ceramics combined with strong attenuation by liquid water provides the necessary contrast to image water presence in proton exchange membrane fuel cells and their components.

Motivated by the recent commercial availability of a compact terahertz source and video-rate terahertz camera, a simple terahertz imaging system in transmission geometry was realised. First, as a first step towards flooding inspection in an operating fuel cell, the feasibility of the imaging system for visualising and quantifying liquid water during an ambient air desorption process for Nafion membranes of a wide range of thicknesses – NRE-212 (50 μm), N-115 (127 μm), N-117 (180 μm) and N-1110 (254 μm) was investigated. It was demonstrated that the imaging system was able to quantify liquid water in the 25-500 μm thickness range, estimate

membrane weight change related to liquid water desorption, which correlated well against simultaneous gravimetric analysis and visualise the room temperature liquid water desorption process of a partially hydrated Nafion N-117 membrane.

Further work consisted in imaging water build-up inside an operating proton exchange membrane fuel cell using the terahertz imaging system, combined with high-resolution optical imaging. Using a custom-built, laboratory-scale, terahertz, and optically transparent fuel cell, two-phase flow phenomena of water accumulation and transport, such as membrane hydration, main droplet occurrence, water pool formation, growth, and eventual flush out by gases were imaged. Results of the terahertz agree with simultaneous optical imaging and electrochemical readings. To demonstrate the potential used of the proposed imaging modality, the effect of air gas flow rates on flooding was demonstrated.

Contents

List of Tables

List of Figures

List of Abbreviations and Acronyms

Abbreviation	Meaning
2D	Two dimensional
3D	Three dimensional
API	Active pharmaceutical ingredient
BD	Back diffusion
CL	Catalyst layer
CT	Computed tomography
CW	Continuous wave
DDR	Double-drift region
DVS	Dynamic vapour sorption
EIS	Electrochemical impedance spectroscopy
EOD	Electroosmotic drag
FET	Field-effect transistor
FPA	Focal plane array
GDL	Gas diffusion layer
GFC	Gas flow channels
GHz	Gigahertz
HOR	Hydrogen oxidation reaction
IMPATT	Impact ionisation avalanche transit-time diode
MEA	Membrane electrode assembly
MPL	Microporous layer
MRI	Magnetic resonance imaging
NMR	Nuclear magnetic resonance
OCV	Open circuit voltage
ORR	Oxygen reduction reaction
PCA	Photoconductive antenna
PEM	Proton exchange membrane
PEMFC	Proton exchange membrane fuel cell
PTFE	Polytetrafluoroethylene
QCL	Quantum-cascade laser
SDR	Singe-drift region

SEM	Scanning electron microscopy
SPEEK	Sulfonated poly(ether ether ketone)
TGA	Thermogravimetric analysis
THz	Terahertz
THz-TDS	Terahertz time-domain spectroscopy
TPI	Terahertz pulsed imaging
TPX	Polymethylpentene

1. Introduction

Hydrogen fuel cells are clean energy conversion devices, poised favourably to replace the traditional fossil fuel-based energy system. Proton exchange membrane fuel cells (PEMFCs) are considered one of the most promising technologies in the field, especially (but not limited to) vehicular applications. Water management is a key engineering challenge that inhibits widespread commercialisation. Current techniques on water visualisation are promising but expensive and not readily available. Terahertz (THz) radiation is an unexplored region of the electromagnetic spectrum for PEMFC applications. This introductory Chapter presents a brief background to PEMFCs and terahertz science and technology, along with the research motivation, Dissertation outline and novel contributions to the field.

1.1. Motivation

Economic historians agree that the onset of the Industrial Revolution between the mid-late 1700s to early 1800s is the most important event in the history of humanity since the domestication of animals and plants. However, the transition from hand production methods to machines, novel chemical manufacturing processes and coal-powered energy also brought major environmental impact, such as air and water pollution. In the 21st century, mounting environmental pollution problems, depletion of traditional fossil fuel reserves and public awareness of climate change drove demands for new, clean, and renewable energy sources to replace the traditional fossil fuel-based energy system. As a non-fossil fuel, clean and renewable energy source, hydrogen is expected to play a significant role in a future energy conversion paradigm.

Fuel cells are electrochemical devices that convert the chemical energy of a fuel into electricity via a pair of redox reactions with an oxidising agent (oxygen). If hydrogen is the fuel, water and waste heat are the only by-products. However, unlike other electrochemical cells such as batteries, fuel cells can achieve continuous energy output, if fuel and oxidant are supplied. Given their high efficiency, low noise, low emissions and lack of moving parts, fuel cells have been applied in a wide range of applications, including transportation, material handling, stationary, portable, and emergency backup power. In particular, PEMFCs has been profoundly studied in recent years as one of the most promising technologies in this subject, especially for vehicular applications, due to lower operating temperatures (60-80 °C) and fast start/stop cycles [1]–[4].

Despite solid technological advancements over the years, widespread adoption of PEMFCs has been plagued by several technical obstacles, including high cost of platinum catalysts, sluggish cathode kinetics and insufficient lifetime [5]. A particularly difficult challenge is the issue surrounding PEMFC water management [6]. The core mechanisms behind water production in PEMFCs are electrochemical generation at the cathode and droplet condensation from humidified inlet gases. The vast majority of PEMFCs incorporate Nafion, a perfluorinated sulfonic-acid ionomer, as the solid proton exchange membrane (PEM). Nafion is generally preferred because of its ability to efficiently conduct protons through a chemically inert, mechanically and thermally robust polymeric matrix, while inhibiting the transport of electrons and forming a physical barrier to prevent reactant mixing [7]. It is well known that the proton conductivity of Nafion is highly dependent on the degree of hydration [8]–[12], which affects

the efficiency of the electrochemical reaction. Failure to achieve a sufficient level of PEM hydration will lead to decreased proton conductivity, which in turn leads to cell performance losses and possible permanent material damage [13]. On the other hand, at high current densities and/or low gas stoichiometry, the cell's rate of water production will surpass the inlet gases' transport capacity, resulting in flooding. When a severe level of flooding is reached, liquid water clogs up the gas channels and completely fills the pores of the catalyst layer or gas diffusion layer (GDL). This results in mass transport limitations of reactant gases to active sites and decline of cell performance [14]. Several visualisation techniques, such as magnetic resonance imaging (MRI), neutron imaging, X-ray radiography and tomography, optical diagnostics, fluorescence microscopy, and infrared imaging have been applied extensively to perform in situ and ex situ studies of water distribution and transport dynamics in PEMFCs and its constituent parts [15]–[17]. However, various inherent downsides with these techniques include low frame rate, limited availability, and excessive cost, requiring significant cell modification, limited penetration depth and contrast.

Terahertz radiation, also known as T-rays or T-waves, occupy the region of the electromagnetic spectrum between 0.1 and 10 THz [18]. The neighbouring frequency ranges can also be characterised by their respective technologies. At lower frequencies lies the electronic regime of millimetre or microwave radiation, where solid-state devices based on electron transport are used to efficiently produce radiation. At higher frequencies, lies the optical regime, where active optical devices like semiconductor lasers and light-emitting diodes generate light based on optical fibres. The frequency ranges of these technologies do not overlap, causing the so-called "terahertz gap." However, many important breakthroughs in terahertz generation and detection technology in the late 1980s [19]–[22] decreased the barrier for terahertz researchers to access the "terahertz gap". Since then, table-top commercial terahertz devices have been developed and thus interest in this topic has increased exponentially.

Terahertz radiation travels in a line of sight, is non-ionising, and can penetrate through dielectric materials, such as plastics, textiles, paper, wood, and ceramics. Simultaneously, many biomolecules, proteins, explosives and narcotics also feature spectral features in the terahertz regime [23]. Liquid water is also one of the strongest absorbers of terahertz radiation: these electromagnetic waves are sensitive to intermolecular vibrations of the hydrogen bond [24]. These characteristics in turn make terahertz techniques attractive for a number of applications including pharmaceutical coating analysis, material characterisation, concealed weaponry detection, and cancer detection [25].

1.2. Dissertation outline

The present Dissertation is structured into six separate Chapters:

- **Chapter 1** introduces the background information, research motivation and key novel contributions to the field.
- **Chapter 2** expands on technical information about PEMFCs, especially focussed on water transport and accumulation mechanisms. Further, the field of terahertz science and technology is introduced, specifically terahertz time-domain spectroscopy (THz-TDS), continuous wave (CW) generation schemes and focal plane array (FPA) detection schemes, and industrial applications are displayed. Finally, it extensively reviews the current state of the art on liquid water visualisation techniques for PEMFCs. These techniques are classified in terms of their specific pros and cons, with particular focus on temporal and spatial resolutions.
- **Chapter 3** describes in detail the experimental procedures used to perform the work presented in this Dissertation. It addresses the lab-scale transparent fuel cell and gas delivery system, terahertz transmission imaging system setup, alignment, and calibration, simultaneous gravimetric setup, high-resolution optical imaging, and the entirety of data processing routines.
- **Chapter 4** demonstrates the feasibility of a novel terahertz imaging system based on a 0.1 THz impact ionisation avalanche transit-time (IMPATT) diode source and a FPA terahertz camera for direct water quantification and visualisation in hydrated Nafion PEMs, as an initial route towards liquid water inspection in fully operating PEMFCs. In particular, the system's sensitivity for water quantification against water with known layer thickness is validated, and water weight in a wide range of Nafion membranes is estimated across time, benchmarked against simultaneous gravimetric analysis. Finally, to assess the system's ability to spatially resolve water distribution, the dehydration profile of a partially hydrated Nafion membrane was imaged.
- **Chapter 5** presents the design progress of a terahertz and optically transparent PEMFC for flooding observations, where two distinct versions are discussed. Their components, electrochemical characterisation, testing protocols are discussed in detail. Most importantly, a similar terahertz imaging system was demonstrated for visualisation of two-phase flow patterns, including membrane hydration, main droplet occurrence, water pool growth and washout, as well as the effect of varying gas flow rates. The

results were successfully validated against simultaneous optical imaging and electrochemical readings.

- **Chapter 6** summarises and evaluates all the work that has been achieved during the PhD project, vital contributions, and findings. The potential problems are identified and recommendations for future work are discussed.
- **Appendix A** details the Matlab code listings developed for data processing during this Dissertation.

1.3. Original contributions

The contributions to the field in the content of this Dissertation are based on the demonstration of an imaging system based on a video-rate FPA terahertz camera and 0.1 THz IMPATT source, and corresponding algorithm for image processing for:

- Quantification and spatial visualisation of hydration levels in industry standard Nafion membranes, which correlated well with simultaneous gravimetric measurements.
- Observations of two-phase flow patterns in operating PEMFCs, which included membrane hydration, main droplet occurrence, water pool formation, growth, and flushing, along with investigating the effect of differing gas flow rates. The results were in accordance and complemented simultaneous high-resolution optical gauging and electrochemical readings.

To the author's best knowledge, this is the first time that terahertz imaging using FPAs terahertz cameras has been successfully applied in the field of water visualisation in PEMFCs. Whilst the author acknowledges that further research is required before widespread utilisation by Nafion PEM manufacturers, it fulfils the main objective of the PhD project and opens diverse avenues for applications. It has potential as a cost-effective complementary alternative as part of a future Nafion manufacturing quality control strategy, as well as to assess the effect of novel materials and configurations along with testing flooding mitigation strategies during PEMFC operation with high sensitivity.

The following publications were achieved on the course of this PhD:

Journal publications

D. F. Alves-Lima, R. Letizia, R. Degl'Innocenti, R. Dawson, H. Lin, "Quantitative video-rate hydration imaging of Nafion proton exchange membranes with terahertz radiation", *J. Power Sources*, vol. 450, pp. 227665, 2019, doi: 10.1016/j.powsour.2019.227665.

D. F. Alves-Lima, J. Song, X. Li, A. Portieri, Y. Shen, J. A. Zeitler, H. Lin, "Review of Terahertz Pulsed Imaging for Pharmaceutical Film Coating Analysis", *Sensors*, vol. 20, no. 5, pp. 1441, 2020, doi: 10.3390/s20051441.

S. Kudlacik-Kramarczyk, A. Drabczyk, M. Glab, **D. F. Alves-Lima**, H. Lin, T. E. L. Douglas, S. Kuciel, A. Zagorska, B. Tyliszczak, "Investigations on the impact of the introduction of the *Aloe vera* into the hydrogel matrix on cytotoxic and hydrophilic properties of these systems considered as potential wound dressings", *Mater. Sci. Eng. C*, vol. 123, pp. 111977, 2021, doi: 10.1016/ j.msec.2021.111977.

R. A. Mensah, S.-b. Jo, H. Kim, S.-M. Park, K. D. Patel, K. J. Cho, M. T. Cook, S. B. Kirton, V. Hutter, L. E. Sidney, **D. F. Alves-Lima**, H. Lin, J.-H. Lee, H.-W. Kim, D. Y. S. Chau, "The eggshell membrane: a potential biomaterial for corneal wound healing", *J. Biomater. Appl.*, vol. 36, no. 5, pp. 912-925, 2021, doi: 10.1177/08853282211024040.

D. F. Alves-Lima, B. M. Williams, H. Schlegl, G. Gupta, R. Letizia, R. Dawson, H. Lin, "Visualizing Water Inside an Operating Proton Exchange Membrane Fuel Cell with Video-Rate Terahertz Imaging", *Fuel Cells*, In press.

Conference publications

D. F. Alves-Lima, R. Letizia, R. Degl'Innocenti, R. Dawson, H. Lin, "Investigating liquid water distribution in Nafion polymer electrolyte membrane with terahertz imaging", *In Proceedings of the 2019 44th International Conference on Infrared, Millimeter and Terahertz Waves (IRMMW-THz)*, Paris, France, 1-6 September 2019, doi: 10.1109/IRMMW-THz.2019.8873813.

D. F. Alves-Lima, R. Dawson, H. Lin, "Terahertz imaging for proton exchange membrane fuel cell applications", *In Proceedings of H2FC Supergen Research Conference*, Nottingham, UK, 17-18 February 2020.

Z. Keskin-Erdogan, A. H. Liebenau, M. B. S. Aljaber, D. Vllasaliu, **D. F. Alves-Lima**, H. Lin, A. Meriluoto, J. Spencer-Fry, R. M. Day, D. Y. S. Chau, J. C. Knowles, "Development of

GelMA/GrowDex hybrid hydrogels for biomedical applications", *In Proceedings of the TERMIS EU Chapter Meeting*, Manchester, UK, 26-29 May 2020.

R. A. Mensah, S. -B. Jo, H. Kim, S. -M. Park, K. D. Patel, K. -J. Cho, M. T. Cook, S. B. Kirton, V. Hutter, L. E. Sidney, **D. F. Alves-Lima**, H. Lin, J. -H. Lee, H. -W. Kim, D. Y. S. Chau, "The in vitro and in vivo characterisation of decellularized chicken eggshell membrane for translational regenerative applications", *In Proceedings of the TERMIS EU Chapter Meeting*, Manchester, UK, 26-29 May 2020.

D. F. Alves-Lima, H. Schlegl, B. M. Williams, R. Letizia, R. Dawson, H. Lin, "Observing liquid water build-up in proton exchange membrane fuel cells using terahertz imaging and high-resolution optical gauging", *In Proceedings of the 2020 45th International Conference on Infrared, Millimeter, and Terahertz Waves (IRMMW-THz)*, Buffalo, NY, USA, 8-13 November 2020, doi: 10.1109/IRMMW-THz46771.2020.9370456.

D. F. Alves-Lima, H. Schlegl, B. M. Williams, R. Letizia, R. Dawson, H. Lin, "Simultaneous terahertz imaging and optical gauging of water build-up in a PEMFC", *In Proceedings of the European Fuel Cell Forum: Low Temperature Fuel Cells, Electrolysers & H_2 Processing*, Lucerne, Switzerland, 29 June – 2 July 2021.

X. Li, **D. F. Alves-Lima**, R. Degl'Innocenti, R. Dawson, H. Lin, "Extracting the dielectric relaxation of water in thin Nafion membrane by terahertz spectroscopy", *In Proceedings of the 46th International Conference on Infrared, Millimeter, and Terahertz Waves (IRMMW-THz)*, Chengdu, China, 29 August – 3 September 2021, doi: 10.1109/IRMMWTHz50926.2021.9567642.

A. Zaman, N. W. Almond, Y. Lu, X. Romain, **D. F. Alves-Lima**, H. Lin, O. Burton, J. Alexander-Webber, S. Hofmann, T. Mitchell, J. D. P. Griffiths, H. E. Beere, D. A. Ritchie, R: Degl'Innocenti, "Graphene-based External Optoelectronic Terahertz Modulators for High Speed Wireless Communications", *In Proceedings of the 14th UK-Europe-China Workshop on Millimetre-Waves and Terahertz Technologies (UCMMT)*, Lancaster, UK, 13-15 September 2021, doi: 10.1109/UCMMT53364.2021.9569931.

2. Sensing water presence in PEMFC: Literature review

Balanced water management strategies are critical for optimum PEMFC performance and durability. In-situ water visualisation can be achieved using techniques such as MRI, X-ray radiography, or optical diagnostics, each with their own pros and cons. Terahertz radiation offers an attractive alternative to image flooding in transparent PEMFCs due to its inherently high sensitivity towards liquid water. Thus, this Chapter will expand on basic concepts of PEMFCs, terahertz science and technology, and review state of the art liquid water visualisation techniques for PEMFCs, to establish a foundation for the experimental work presented later into the Dissertation.

2.1. Introduction

Water plays an important role in PEMFC operation: Nafion PEM requires hydration to operate and hence lab-scale reactant inlet streams are humidified [26] , but at the same time, water is a by-product of the electrochemical half-reaction at the cathode and therefore must be swiftly removed to prevent cell flooding and reactant starvation at active electrocatalyst sites [27]. Commercial fuel cells can be self-humidifying, but the addition of water-retaining additives leads to agglomeration, mechanical brittleness, and high ohmic resistance [28] .Liquid water transport in an operating PEMFC is a challenging phenomenon to study due to the opaque nature of traditional GDL and bipolar plate materials. For water fault diagnosis, various methods exist such as the assessment of pressure drop [14], electrochemical impedance spectroscopy (EIS) [29], residence time distribution [11, 12]. However, one of the main drawbacks of these techniques is that they provide an indirect assessment of the entire operating fuel cell and do not allow the location the faults to be determined.

Critical insights into the complex physical phenomena involving liquid water condensation and transport within the PEMFC can also be provided by imaging techniques, but these have drawbacks including excessive costs, limited availability and limited contrast and penetration in the PEMFC.

Terahertz radiation can penetrate through dielectric materials, such as polymers, but is strongly absorbed by polar materials, such as liquid water, which motivates the use of terahertz sensing for non-destructive monitoring of water presence in PEMFCs and their components.

In this chapter, an overview of PEMFC basic concepts, particularly focused on water accumulation and transport, as well as on terahertz science and technology, including terahertz instrumentation and industrial applications will be provided. This will then be followed by a literature review of the most common liquid visualisation techniques in PEMFCs: MRI, neutron imaging, x-ray radiography and tomography, optical diagnostics, and infrared imaging.

2.2. PEMFC

Fuel cells are comparable to batteries differing in the fact that fuel cell requires a continuous feeding of fuel and oxidant to operate in contrast to batteries that already have the chemicals stored inside. Therefore, fuel cells have the advantage of theoretically being capable of producing electricity if there is fuel supply. Individual cells often produce insufficient voltage, so they are stacked in series to meet the specific demands for their various applications. William

Grove is credited for the first fuel cell demonstration in 1839, a device named "gas battery". However, only in the next century fuel cells would remerge, as NASA decided to develop them in the 1960's for space missions. Since then, fuel cells found applications in a myriad of fields, such as vehicles, stationary and mobile power generation, sensors. Fuel cells are classified according to type of electrolyte and fuel used and include alkaline fuel cell, phosphoric acid fuel cell, molten carbonate fuel cell, solid oxide fuel cell and PEMFC [32]. Due to high efficiency, silent operation, low environmental impact, few moving parts, potential independence from carbon-based fuels, amongst other advantages, many regard fuel cells to be at the forefront of a revolution in the electricity industry [33].

PEMFCs are low temperature fuel cells, poised as the best candidates for powering automobiles. As the name implies, they incorporate a solid proton exchange or polymer electrolyte membrane, and the standard material for PEMs is Nafion [7]. First developed by DuPont, Nafion comprises a polytetrafluoroethylene (PTFE) backbone with perfluorinated-vinyl-polyether side chains containing sulphonic acid end groups, which are responsible for Nafion's proton conducting properties. It is also widely used due to its excellent thermal and chemical stability.

In an archetypical PEMFC, hydrogen fuel is fed to the anode where it is oxidised on an electrocatalyst, usually platinum, to protons and electrons (Figure 2.1). The hydrogen oxidation reactions (HOR) are represented by:

$$H_2 \rightarrow 2H^+ + 2e^-, E^o = 0\ V, {}^{dE^o}/_{dT} = 0\ mV\ K^{-1} \quad \text{[34] (2.1)}$$

The newly formed electrons flow through an external circuit, creating the electricity output of the PEMFC. The protons migrate through the PEM to the cathode, where they react with inlet oxygen and electrons to produce water molecules and heat, also catalysed via platinum electrocatalyst. The oxygen reduction reaction (ORR) is given by:

$${}^{1}/_{2}\, O_2 + 2H^+ + 2e^- \rightarrow\ H_2O, E^o = 1.2291\ V, {}^{dE^o}/_{dT} = 0 - 0.8456 mV\ K^{-1} \text{ [35] (2.2)}$$

In PEMFCs, the ORR has significantly slower reaction kinetics than the HOR, and responsible for most polarisation losses in the cell. It is the bottleneck of PEMFC technology, especially for fuel cell cars. The overall reaction is represented by:

$$H_2 + {}^{1}/_{2}\, O_2 \rightarrow\ H_2O, E^o = 1.2291\ V, {}^{dE^o}/_{dT} = 0 - 0.8456 mV\ K^{-1} \quad (2.3)$$

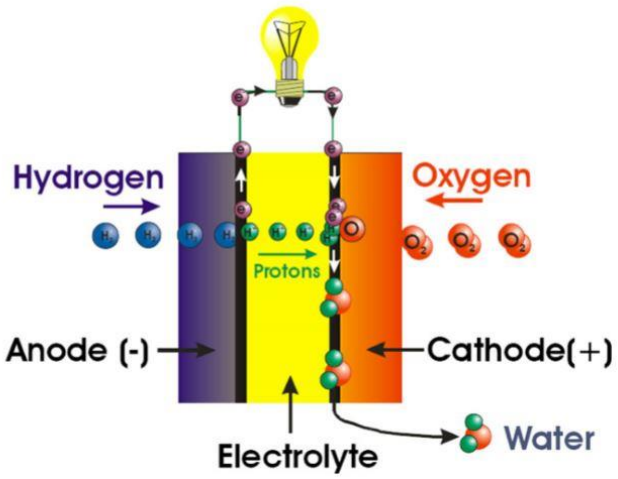

Figure 2.1 – Proton exchange membrane fuel cell diagram. Adapted from [33]***.***

PEMFC single-cell assemblies are composed of the following parts (Figure 2.2):

- PEM. Allows for proton conduction between electrodes while preventing electronic conduction, which could lead to short-circuiting the fuel cell. Furthermore, it also separates the reactants preventing parasitic side reactions. However, high associated costs of Nafion PEMs pave the way for alternative membrane material such as graphene oxide, sulfonated poly(ether ether ketone) (SPEEK), polybenzimidazole and carbon nanotubes [36], [37]. The PEM, along with the catalyst and gas diffusion layers, make up the membrane electrode assembly (MEA).
- Catalyst layers (CL). Consisting of a porous layer of electro-catalyst on each side of the PEM, where the half reactions will occur. The usual electrode material is platinum on carbon support, known for its catalytic properties [32], [38], [39], even though there is research on non-precious metal catalyst for PEMFC [40], given platinum's high cost. Kinetically, the ORR is slower than the HOR and therefore platinum loadings are as low as 0.05 $mg_{Pt}.cm^{-2}$ in the latter [41] and as high as 0.4 $mg_{Pt}.cm^{-2}$ in the former [42].
- Gas diffusion layers (GDL). The role of the GDLs is ensuring consistent and uniform reactant gas feeding to the CLs through the gas flow channels, providing structural integrity to the MEA, allowing for electron and heat transport and facilitating water removal from the MEA [43], [44]. The typical materials for GDLs are carbon paper or cloth, treated with PTFE to prevent water blockage of the pores, therefore enhancing reactant transport to the CLs [45]. Usual PTFE loadings ranges from 5 to 30%, although 20% is described as the optimised value [46], [47]. In certain applications, a thin microporous layer (MPL) is incorporated at the interface between the GDL and CL. The pore size in the MPL is in the

range of decimals of µm while in the GDL is in the tens of µm [48]. It has been shown that MPL integration has a positive effect on MEA flooding, but the underlying mechanisms are still subject of debate [48], [49].

- Bipolar/end plates. Endplates have machined-through gas flow channels on one side, to deliver the reactant streams evenly to the catalytically active areas, and a flat surface on the other side. In the case of stacks, bipolar plates are used where gas flow channels are found on both sides of the plates. The function of this component is to ensure mechanical support to the cell/stack, provide uniform compression across the cell/stack, prevent gas/liquid leakage and, in the case of bipolar plates, electrically connect the individual cells. Graphite is the most commonly used material due to its chemical stability and low electrical resistivity even though other materials are being researched to overcome some drawbacks of graphite (high cost, low mechanical strength) such as stainless steel, brass and polymeric composites [50]–[52].
- Gaskets, screws, nuts, current collectors, and other auxiliary hardware to ensure overall cell tightness and stability and electron conduction.

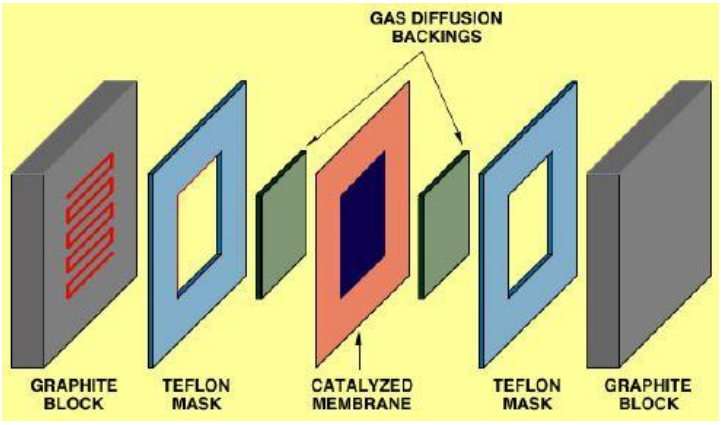

Figure 2.2 – Schematic description of PEMFC components. Adapted from [32].

A critical aspect in PEMFC operation is its water management. Water is a product of the electrochemical reaction and must be removed efficiently because of deleterious effects of accumulation, which will be described further into this report. However, due to the operating conditions of the cell and the nature of its components, water transport happens through a myriad of different mechanisms, which are complex and the relevance and effects of each one of them are still debated amongst scientists. Furthermore, it is vital to point out that water management is a large topic, and its description is an overview of the most important points.

Firstly, in Figure 2.3, water transport mechanisms across the PEM are the following:

- Electroosmotic drag (EOD). In this type of fuel cell, protons flow from the anode to the cathode side of the cell by electromotive forces across the membrane. Neighbouring water molecules are dragged along, since in aqueous media protons do not exist as isolated species and tend to associate with water molecules to form the hydronium (H_3O^+) compound [53]. This is considered the main water transport mechanism.
- Back diffusion (BD). As mentioned above, electrochemical water production occurs on the cathode side of the cell, so this region tends to have a bigger water content than the anode side. This causes a gradient across the membrane and shifts the water flux towards the anode side [53].

In addition, water transport across the GDL is achieved mainly by pressure driven hydraulic permeation, diffusion and evaporation [53].

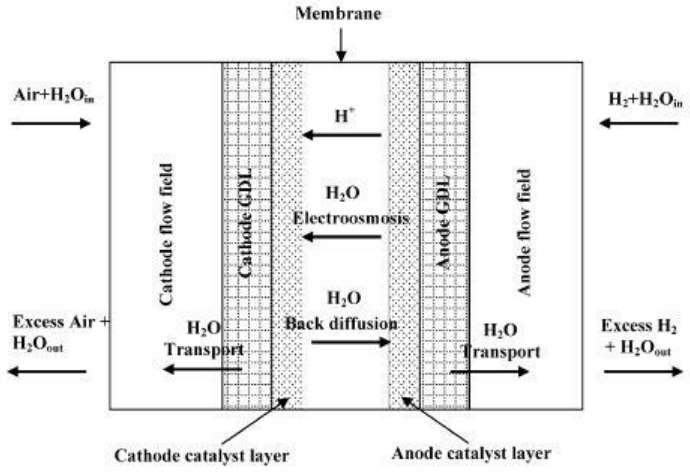

Figure 2.3 - Illustrative overview of water transport mechanisms in a PEMFC. Adapted from [48]**.**

The reversible voltage (E_r) refers to the theoretical maximum cell potential, assuming cell ideal behaviour i.e. cell voltage is independent of the current drawn, and can be calculated from the following equation:

$$E_r = -\frac{\Delta G}{nF} \tag{2.4}$$

Where ΔG refers to the change of Gibbs free energy of the overall reaction (J mol^{-1}), n is the number of electrons transferred (in this case, 2) and F is the Faraday constant (96485 C mol^{-1}). However, even when operating the PEMFC on open circuit voltage (OCV), E_{OCV}, i.e. PEMFC is disconnected from the load and therefore zero current is drawn, the output is lower than the

theoretically determined. This effect arises from parasitic side reactions due to fuel crossover and electron conduction across the membrane (internal currents) [54]. Consequently, the operating fuel cell voltage (E_{cell}) is determined by equation (2.5):

$$E_{cell} = E_{OCV} - E_{irrev} \tag{2.5}$$

Figure 2.4 presents a sample current-voltage curve (known as polarisation curve) for a PEMFC. Polarisation curves are a common way to assess performance at an operating point. A potentiostat linearly sweeps the current while measuring the voltage.

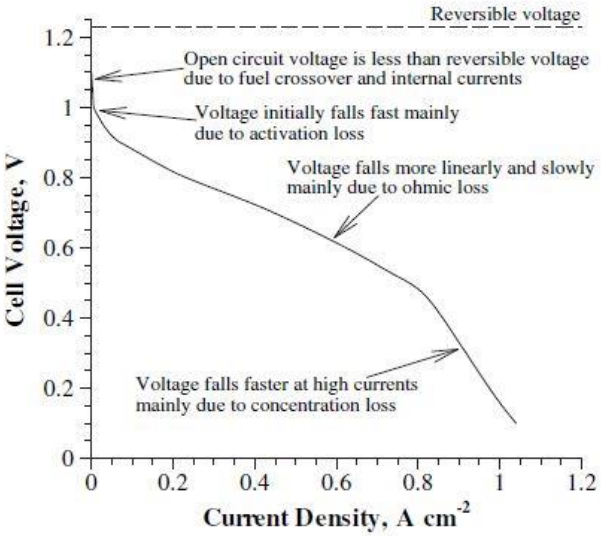

Figure 2.4 - Example of a polarisation curve. Adapted from [54]**.**

E_{irrev} refers to the irreversible potential losses during fuel cell operation, which can be represented as a sum of three factors:

$$E_{irrev} = \upsilon_{act} + \upsilon_{ohm} + \upsilon_{conc} \tag{2.6}$$

Where υ_{act}, υ_{ohm}, and υ_{conc} refer to voltage losses due to the activation, ohmic and concentration polarisation, respectively. These are the three main underlying mechanisms behind the shape of the polarisation curve [55].

Activation polarisation relates to the kinetics of the electrochemical reaction. There is a certain activation energy, associated with the slowest step of each electrochemical half reaction, which must be overcome, and voltage loss happens as a result. This type of polarisation loss in a PEMFC is associated mostly with the ORR. As seen in Figure 2.4, this mechanism dominates

the low current density part of the graph and amounts to 0.1 to 0.2 V of loss in this part of the spectrum [56]. Equation (2.7) represents the anode and cathode activation polarisation:

$$v_{act} = \frac{RT}{nF\alpha} \ln\left(\frac{i}{i_0}\right) \tag{2.7}$$

Where R is the ideal gas constant (8.314 J mol^{-1} K^{-1}), T is the temperature (K), α is the charge transfer coefficient, i and i_0 are current density and exchange current density (A cm^{-2}).

Ohmic polarisation refers to the natural resistance to charge flow of the fuel cell components, which leads to voltage losses. All the cell components contribute to this effect, including the GDL, CL, PEM and bipolar/endplates [56]. The ohmic losses are predominant in the intermediate region of the graph and can be expressed as:

$$v_{ohm} = i(R_{electronic} + R_{ionic} + R_{contact}) \tag{2.8}$$

Where $R_{electronic}$, R_{ionic} and $R_{contact}$ (Ω) are electronic, ionic, and contact resistance, respectively. Inefficient removal of product water from the CL/GDL interface causes flooding and hinders mass transport of the gaseous reactants to these catalytically active areas in a phenomenon known as concentration polarisation. This happens across the entire range of the current density but gets especially relevant at the higher end of the spectrum [57]. Concentration polarisation is described by equation (2.9):

$$v_{conc} = \left(\frac{RT}{nF}\right) ln\left(1 - \frac{i_L}{i_L - i}\right) \tag{2.9}$$

Where i_L represents the limiting current (A), which depends on process conditions. In Figure 2.5a, examples of polarisation curves at different flooding levels are shown. At high current densities, the rate of water production usually exceeds the rate of water purging which leads to accumulation (flooding) and issues on the mass transport of reactants to CLs. The graph demonstrates that the more severe the flooding issue, voltage drops associated with concentration polarisation are sharper and occur earlier in the current density range. Furthermore, Figure 2.5b shows the voltage output of a PEMFC operating at constant current density. As mentioned before, if enough water builds-up during operation, it will block gas delivery to catalyst sites, which will cause the negative spikes in voltage output. Eventually, as time goes on, inlet gases will build-up enough pressure to flush the blocking water out, which will cause to a positive spike in the voltage and, after a period, will stabilize to its standard value. This fluctuation causes unstable, unreliable and inconsistent cell performance [48]. Additionally, it is important to note that flooding is not a CL/GDL interface exclusive

occurrence, but also happens on every other cell component, for a myriad of reasons e.g. operating conditions and cell component design.

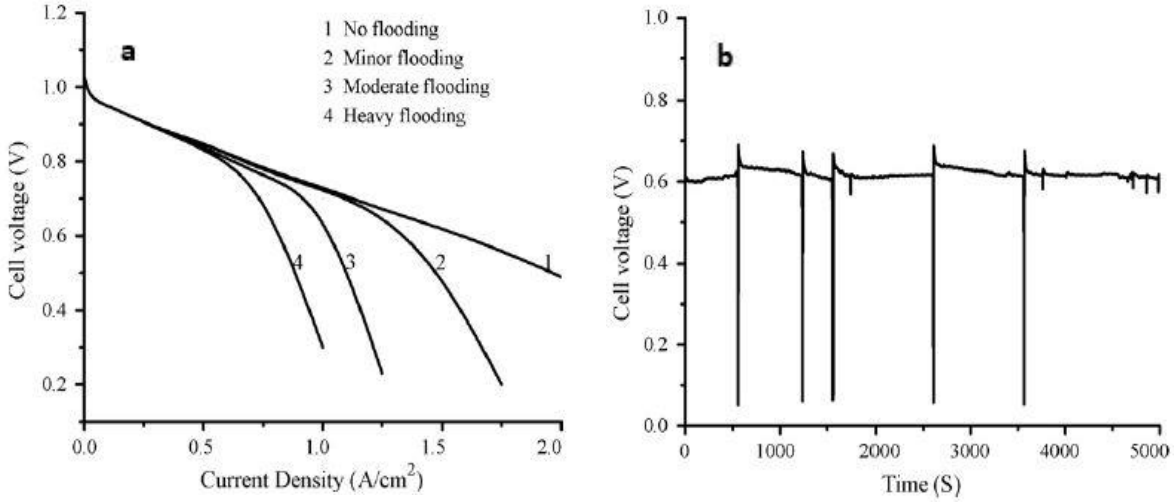

Figure 2.5 – Effects of concentration polarisation on PEMFC performance: (a) Polarisation curves of escalating levels of PEMFC flooding; (b) PEMFC voltage output during constant current density operation. [48]

The previous paragraphs focussed on the importance of efficient removal of water to prevent flooding in the PEMFC and all its negative effects. Nevertheless, there is a different aspect to water management, one that requires keeping moisture inside the cell. Nafion, as PEM material, has the intrinsic ability of being able to conduct protons and not allow transport of electrons. Nevertheless, it is widely accepted in the PEMFC literature, that Nafion needs a good level of hydration in order to achieve proper proton conduction [12], [27], [58], [59]. Evidence of linear relation between proton conductivity and amount of water in Nafion can be found on Figure 2.6. Furthermore, membrane drying due to faulty operating conditions and/or local hotspots can lead to material damage e.g. pinholes [60].

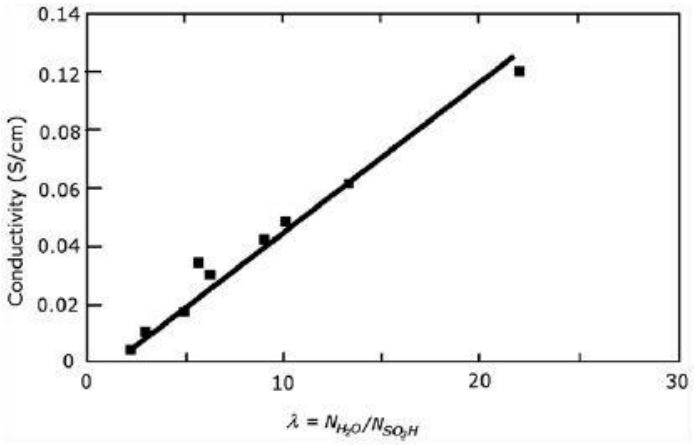

Figure 2.6 – Nafion membrane proton conductivity vs water content, at 30°C. Adapted from [61]**.**

Consequently, inlet gases go through a humidification process prior to entering the cell to ensure appropriate water content in the membrane at all times during PEMFC operation [62]. This introduces an additional source of water besides the electrochemical production, which implies that inlet relative humidity (RH), temperature and pressure need careful control to achieve good balance between the conditions.

2.3. Liquid water visualisation in PEMFC

2.3.1. Magnetic resonance imaging

MRI is type of a non-invasive and non-destructive imaging modality that uses strong magnets to produce two-dimensional (2D) or 3D contrast images. MRI is widely known to the public as a medical diagnostic tool, although it has other applications in engineering and physical sciences. It was developed by Lauterbur and Mansfield in the 1970s [63], who applied the concept of nuclear magnetic resonance (NMR), first discovered by Rabi [64], and expanded to liquids and solids by Bloch and Purcell decades earlier [65], to produce images of living animals. NMR relates to the quantum mechanical magnetic properties of certain atomic nuclei with non-zero spin moment, most commonly the hydrogen nuclei, hence the term ^{1}H-NMR. Hydrogen atomic nuclei are excited by a strong static magnetic field and radio frequency pulses, resulting on split nuclear spin energy levels, with the majority aligning with the magnetic field (lower energy level). The radio frequency signal excites the atomic nuclei to higher energy levels (opposed to the magnetic field) and their subsequent relaxation resonates at a detectable characteristic frequency. The signal amplitude then correlates to the amount of hydrogen and water molecules in the sample [17]. The phase and frequency of the signal are used to generate images through spatially encoding and selection methods such as single-scan multidimensional experiments, pure shift and selective refocusing experiments [66].

In the context of PEMFC, MRI can be a useful tool for in situ investigation of water distribution during fuel cell operation, given the capacity of detecting liquid water molecules through optically opaque components. The procedure was first described in 2004 [67], where MRI was used to display spatially resolved hydration levels in a 340 μm thick PEM inside an operating fuel cell. Through-plane images of the fuel cell revealed less hydration on the anode side of the membrane, which was attributed to the dominance of the EOD for water transport across the PEM. Further, by increasing the current load on the cell, the water content in the PEM

decreased proportionally to the increase ohmic resistance, as seen in Figure 2.7. In the same year, in-plane visualisation of water distribution in PEMFC components using MRI was also demonstrated [68]. Water transport phenomena were observed such as transient water obstructions in gas flow channel, non-uniform PEM hydration, pooling outside of O-ring seals and diffusion of water from the MEA into the surrounding Nafion structure, the latter for the first time.

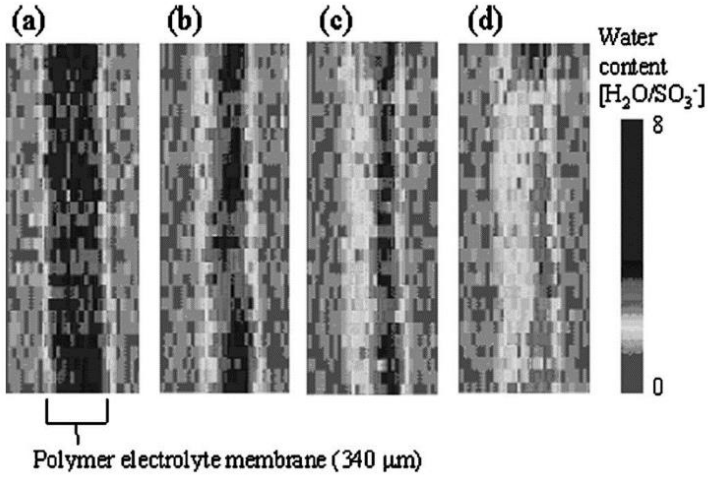

Figure 2.7 – Water content in the membrane under fuel cell operation with (a) 0, (b) 89, (c) 178 and (d) 267 mA/cm^2. The spatial resolution is 25 μm along the direction from the anode to the cathode. Adapted from [67]***.***

MRI was used to study the feasibility of a novel PEMFC design with direct liquid water feed to the PEM [69]. It was found that direct liquid water injection to the PEM led to approximately 40% increase in cell voltage, from decreased ohmic resistance. Additionally, resulting images showed PEM dehydration near the gas inlets being partially mitigated by the liquid water supply and localised membrane deformation due to swelling. The dynamics of water transport and accumulation inside the PEM were also further studied with MRI, by investigating the effect of different PEM materials [70], [71], PEM thickness [72], cell temperature, relative humidity and current density [71], [73], [74].

In a group of systematic in situ studies on in-plane water distribution in PEM [75]–[77] during operation, it was reported that gas flow configurations highly influenced water content and performance of the fuel cell. Particularly, counter-flow configurations resulted in a uniform water distribution while co-flow configurations caused PEM dehydration near the gas inlets. This behaviour is also observed in a study using a PEMFC with 6 cm^2 area [78], where, in a co-flow configuration, progressive water accumulation occurred close to the outlets, while inlets remained dry. This build-up takes place within both the membrane and gas flow channels.

In addition, initial accumulation of liquid water in the cathode is beneficial to the fuel cell's performance, possibly due to rehydration of membrane areas dried by the reactant gases [75]. MRI was also employed for in situ imaging a PEMFC over 11 h of continuous operation with constant load [79]. In-plane 2D images showed the formation of a dehydration front on the PEM surface that propagated slowly, starting from gas inlets and towards gas outlets (Figure 2.8).

Finally, a hydrogen-deuterium exchange system was used as a method to improve MRI contrast when analysing water distributions in a PEM during fuel cell operation under steady state conditions [80]. Particularly, alternating the fuel supply between hydrogen and deuterium gases enables the visualisation of redistribution of water from wet or flooded conditions in the PEM. Measurements with MRI to date have revealed a wealth of valuable insight regarding the water accumulation and transport, on the PEM and gas flow channels. Compared to competing technologies, MRI is sensitive to hydrogen-containing compounds such as water, uses non-ionising radiation and can penetrate optically opaque structures. However, disadvantages include relatively limited spatial resolution and acquisition rates (400x25 μm^2 and 50 s [67]), limited sensing volume, invasiveness, due to requiring replacement of magnetic materials in the fuel cell (nonmagnetic acrylic flow fields [78]), reduced size of the magnet-core for fuel cell housing and significant interference caused when the cell is operated at high current densities [17]. Additionally, MRI machines are usually stationary, requiring a central facility to operate, and their cost is in the order of hundreds of thousands of pounds.

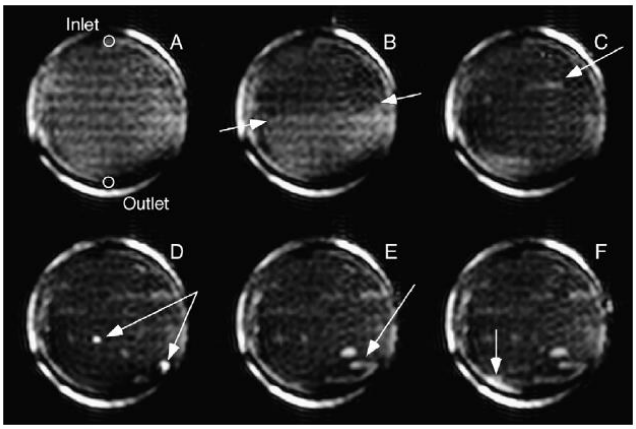

Figure 2.8 – Selected MR images showing water in an operating fuel cell over a ~12h period. Images were acquired at (a) the start of the experiment and after (b) 66, (c) 164, (d) 290, € 473, and (f) 678 min. The fuel and oxidant inlet and outlet are labelled. Arrows point to regions showing flooding, expect for arrows in (b), which highlight the position of the dehydration front that moved from the inlet to outlet. Adapted from [79].

2.3.2. Neutron imaging

Neutron imaging is a non-invasive and non-destructive technique that uses neutron beams to investigate the interior of many materials and engineering components, generating 2D or 3D images [81]. It was first used successfully in the late 1930s, shortly after the discovery of the neutron by James Chadwick in 1932 [82]. Since then, neutron imaging has been applied successfully in several fields such as engineering, biology, archaeology, metallurgy and geoscience [83]. Contrast in neutron images is based on the attenuation properties of the varied materials that compose the sample under test, like x-ray radiographs. However, while X-rays interact with electrons, neutrons interact with the atom's nuclei. This condition can be exploited for PEMFC research since the method has high sensitivity for hydrogen containing compounds, such as water, and can penetrate through common fuel cell materials, such as stainless steel or graphite. The main issue with neutron imaging lies in the scarcity of state-of-the-art neutron sources available for PEMFC applications, with most research reported in the literature being conducted at the Paul Scherrer Institut at Villigen, Switzerland, the National Institute of Standards and Technology's Center for Neutron Research at Gaithersburg, MD, USA, the Penn State Breazeale Nuclear Reactor at State College, PA, USA, the Laboratoire Léon Brillouin at the Orphée Nuclear Reactor in Saclay, France, the CONRAD/V7 facility of the Hahn-Meitner Institute Berlin (BER II research reactor) in Germany, the Neutron Radiography Facility of the Korea Atomic Energy Research Institute at Hanaro, South Korea, and JRR-3 at Tokai, Japan [16].

The earliest reports of neutron imaging for in situ investigation of liquid water accumulation and transport in PEMFC were in 1999 [84] to determine the water distribution in the PEM of a PEMFC, and in 2002 where significant water build-up was observed on the anodic flow channels of the PEMFC [85]. Furthermore, in 2004, several neutron images were acquired to create a movie that provided real-time qualitative of water production, transport and removal throughout the cell [86]. This work also demonstrated the capacity of differentiating flow field water content and PEM/GDL water content.

Since these first demonstrations, neutron imaging has been used to investigate several aspects of water management, such as the effect of different flow field geometries and GDL materials [15], [87]. In [88], neutron radiographs revealed that continuous serpentine channel geometry is more effective at water transport than discontinued interdigitated fingers. On the other hand, another study showed that straight flow fields perform better than serpentine flow fields, due to the high accumulation of liquid water in the corners and consequently gas bypassing the

flow field [89]. The authors also reported that carbon cloth GDLs tended to accumulate less water than carbon paper GDLs. In a following paper employing neutron imaging to investigate water accumulation in a PEMFC with interdigitated flow field [90], which, amongst several findings, showed that GDL layers accumulate water until a critical water mass is reached (approximately 44.2% of available void volume). At this point, product water is removed from the cell at a similar rate in which it is produced. It was also reported that flooding occurs mainly in the outlet channels, while ohmic resistance mean value and temporal fluctuations are proportional to hydration in the membrane and GDL. Neutron imaging experiments were also performed in a relatively large 50 cm^2 active area PEMFC with seven different flow-field patterns [91], based on multiple serpentines, to investigate the effect on varying land size, channel size and land to channel ratio (L:C). Their results indicate that decreasing L:C ratios also decreases overall liquid water in the cell, with L:C ratios smaller than 2:3 considered optimal. They also found that increasing the channel-GDL interfaces, and thus increasing the number of serpentine channels results in higher water accumulation in the fuel cell. Serpentine corners are spots with significant water accumulation and thus less channels result in less turns and corners, which in turn result in less water in the cell. This water build-up at the serpentine corners is also observed in [92], [93]. Neutron radiographs were also used in PEMFCs operating in a cross flow pattern [94] and featuring triangular channels [95], the former displayed. The authors found that BD was prevalent even when using a 180 µm thick PEM, and that triangular channels retained less water, respectively. Recently, neutron imaging was employed to investigate slightly unorthodox PEMFC designs, such as open-cathode and planar air-breathing (Figure 2.9) [96], [97].

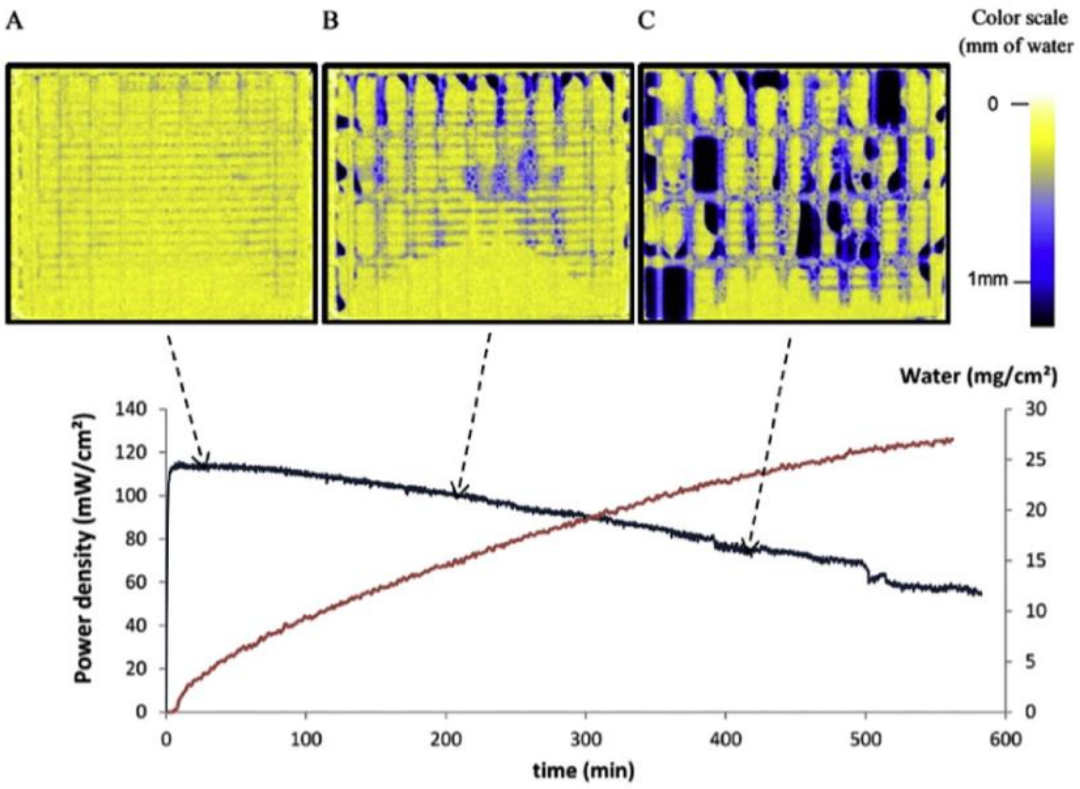

Figure 2.9 – Evolution of power density, water pattern and water accumulation in flooding conditions at 0.7 V operation. The cell numbering from cell 1 to cell 10 from the right to the left of the picture. Adapted from [97]**.**

The influence of operating conditions and material degradation on water management in PEMFC has also been studied with neutron imaging [15], [87]. In particular, it was used to investigate the water content in an operating PEMFC under varying conditions of current density and temperature [98]. They reported that liquid water content increased proportionally to the cell temperature, due to the evaporation of accumulated water at higher temperatures. In a later publication [99], these authors further found that higher cathode inlet gas flowrates resulted in lower water content due to increased water slug and droplet shearing. Neutron imaging is also employed to validate a theoretical model that predicts the location of preferential water accumulation in the cathode, without external humidification of the cathode gas [100]. It was found that, even under a dry cathode supply, water accumulation on the cathode still dominates over the anode. Additionally, this technique is used to study the impact of water accumulation on diffusive limitations in a PEMFC supplied with intermittent short pulses of Helox (79% H_2, 21% O_2) or pure O_2, in between the normal air supply [101]. The authors reported that water accumulation in the channels near the GDL interface have the highest impact on voltage losses related to bulk diffusion. Recently, the effects of GDL degradation (Figure 2.10) and carbon corrosion in the cathode on the water transport and distribution in PEMFC were also studied with neutron imaging [102], [103].

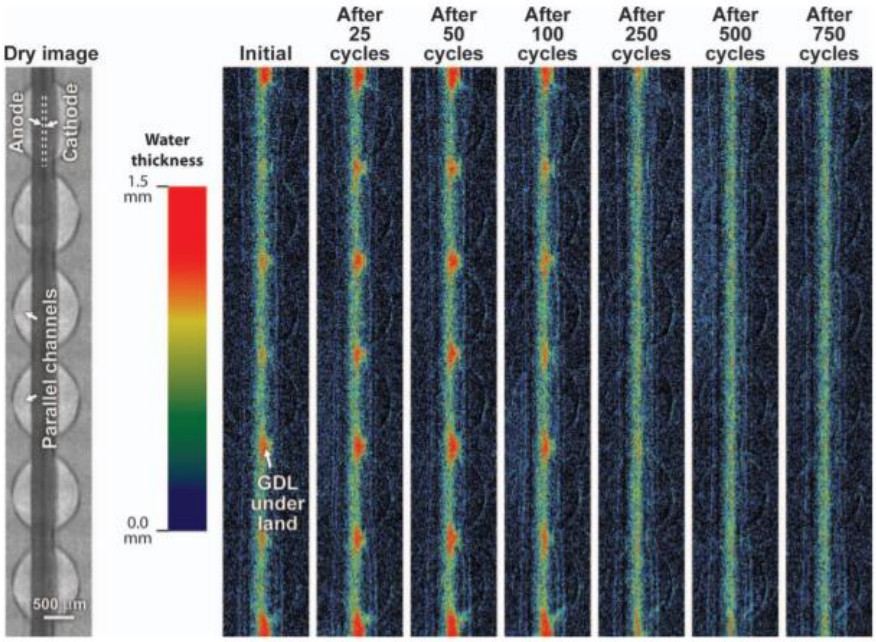

Figure 2.10 – Colourised water-thickness images for a PEMFC at 0.6 V, after progressively greater numbers of potential cycles. 80°C, 100% inlet RH, 1.5/2.5 L/min H_2/air. Adapted from [103]**.**

Neutron imaging has attracted considerable attention in this field, despite its excessive cost and limited availability, with only a couple of facilities capable of performing it worldwide. This attention stems from the sharp contrast achieved towards liquid water and excellent penetration through fuel cell components made of aluminium, graphite, or stainless steel. The use of neutron imaging for water management studies has been extensively demonstrated in the literature with great success, such as the effect of different fuel supply strategies, operating conditions, materials and more advanced studies with simultaneous mass transport loss measurements [83]. Furthermore, sub-10 µm spatial resolution [104] and frame rates up to 100 Hz [105] have been achieved, although not simultaneously. Such high resolution and frame rate would allow for visualisation of microscale droplet transport in a fuel cell, with reported time scales of milliseconds [15]. Despite all the advantages, the inflated cost of this technique means that it is unlikely to be used on a routine basis and applied to perform specific experiments and extract information otherwise not available to more accessible and economical methods.

2.3.3. X-ray radiography and tomography

X-ray radiography is a non-invasive and non-destructive imaging technique using X-rays, a form of ionising radiation, to inspect the internal structure of a sample by generating 2D images.

These images can be further combined via computer processing to produce 3D in a procedure known as computed tomography (CT). X-ray techniques are very well known for their use in medical radiology and airport security, but they also find a myriad of other applications, such as welding inspection [106] and non-intrusive cargo scanning [107]. X-rays were discovered by Wilhelm Röntgen in 1895 [108] and their use for medical imaging was first achieved a year later, in 1896 [109]. To produce an image, a beam of X-rays travels through the sample, and are contrast is based on the X-rays interaction with the electronic clouds of the atoms in the sample. Attenuation depends on material density and composition, so contrast is based on their variation across the sample. Additionally, radiographs can be taken in multiple directions and compiled to create a three-dimensional image (Computer tomography or CT).

In the last decade, high power synchrotron X-ray imaging has been applied to investigate liquid water transport inside PEMFCs. Synchrotron x-ray radiography was used to study water transport behaviour in PEMFC, with high spatial (3 μm) and temporal resolution (5 s) [110]. The authors identified an eruptive water transport mechanism where water droplets present at the GDL pores eject into the gas flow channel and merge into a single drop (Figure 2.11). In a later study, water accumulation through-plane profile in a PEMFC was analysed [111]. It was found that water accumulation in the PEMFC is highly dependent on current density and regions with significant observable build-up were in the gas flow channel/GDL interface and in the MPL. Additionally, synchrotron x-ray technology was employed to take radiographic images and perform micro-CT of an acrylic PEMFC with dry inlet gases [112]. Spatial resolution was 4.8 μm and temporal resolution was 1 s and 60 min for a full tomogram. The authors were able to visualise swelling in the 50 μm Nafion® membrane due to water uptake. In addition, through the tomogram, they were able to see microscopic formation of droplets in the GDL. The feasibility of GDLs featuring transversal pinhole arrays was also studied with X-ray radiography [113]. Temporal and spatial resolution were 12 μm and 1 s, respectively. Radiographs showed preferential water accumulation in the pinhole arrays and more uniformity in water content across the GDL. In contrast, pinhole absent GDLs showed more heterogeneous distribution, which the authors attributed to the GDL's pore distribution. A quantitative study on transient water accumulation in different PEMFC components (GDL and MEA) [114] showed very different water spatial distribution, overall water content and saturation time in each GDL with the cathode flooding after 21 minutes of operation. Spatial resolution was 1 μm. The effect of MPL thickness on water distribution was investigated [115]. Temporal and spatial resolution were 3 s and 10 μm. This study reinforces the idea of the MPL's positive impact on PEMFC flooding by reducing liquid build-up at the MPL/CL interface. An important

discovery is that thicker MPLs also reduce liquid build-up at the MPL/GDL interface. The authors went on to conclude that a GDL made from MPL microporous material could be remarkably effective in water management.

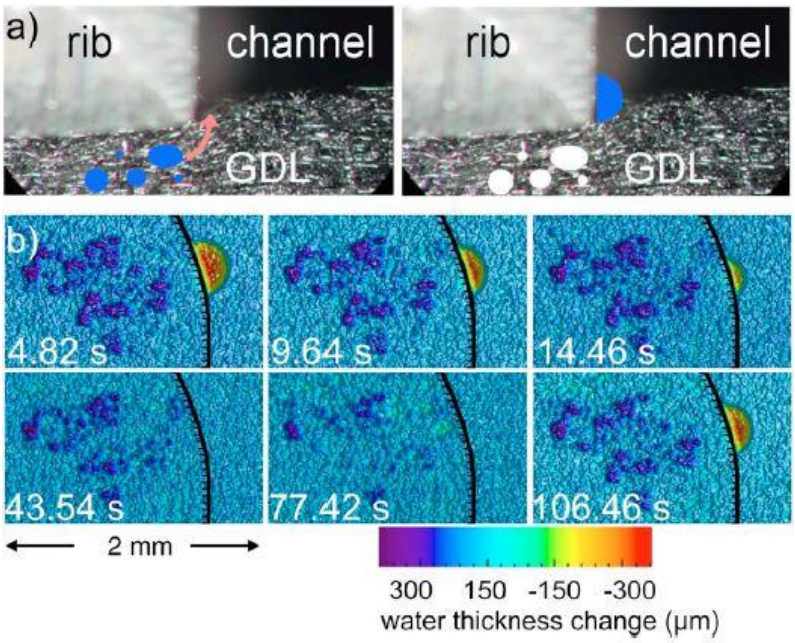

Figure 2.11 - Eruptive water transport from the GDL. (a) Schematic illustration of the eruptive process: water (blue) moves from the GDL pores to the gas flow channel through the channel/rib/GDL interface. (b) Radiographs normalized to the picture before eruption: dark blue and purple regions indicate GDL regions where droplets were before eruption and red to green where the droplets travelled and assembled into a cluster. Adapted from [110]***.***

X-ray radiography is a powerful technique with high temporal and spatial resolution that can provide details on microscale droplet formation and transport in the GDLs, giving it an important advantage over other techniques. However, papers in the literature are often based on synchrotron x-ray sources, which are expensive and have limited availability [15]–[17], [116]. In addition, image contrast is not very strong, since x-rays have limited sensitivity to hydrogen [15] and x-ray's penetration is restricted in dense or high atomic number materials [116].

2.3.4. Optical diagnostics

The idea of photography (capturing an image with visible light) has been described since antiquity and the invention of the first modern camera is credited to Nicéphore Niépce in the early 1800s. Nowadays, optical photography is widely employed in various fields of science, manufacturing, art, and mass communication. In the context of PEMFCs, optical photography

has been employed extensively for liquid water transport and accumulation studies and flooding diagnostics in transparent PEMFCs [117]–[127] and flow fields [121], [125], [128]–[131].

In a 2003 study [117], liquid water transport was visualised in the cathode gas channel of a transparent PEM fuel cell operating at 30 °C. It was found that a hydrophilic cathode GDL resulted in increased current density, which was attributed to a more uniformly hydrated membrane. A further study [127] on the effects of varying GDL materials and hydrophobicity showed that PEMFCs with hydrophilic GDLs were more susceptible to flooding in the cathode gas channel. Furthermore, optical diagnostics of water droplet formation on the anode [123] revealed that hydrophobic GDLs caused droplets to form on the gas channel walls (Figure 2.12) while in hydrophilic GDLs droplets wicked from the channel to the GDL. Additionally, critical hydrostatic pressure head for liquid water breakthrough for several GDL materials has been studied [130]. Finally, water droplet emergence from the GDL surface and behaviour has been investigated [120]. The authors observed physical transport phenomena such as preferential droplet emergence locations, film formation along the channels and channel clogging.

For the purpose of the effect of process conditions and PEMFC design of flooding, the benefits of high oxidant flow rates for water removal were demonstrated, although it resulted in faster PEM dehydration [126]. Flooding in the cathode gas channels of PEMFCs was also examined under parallel, interdigitated and cascaded flow field configurations [124]. The authors observed that, at ambient conditions (25 °C and 1 bar), parallel configuration was the most vulnerable to significant water accumulation, resulting in the worst performance of the three fuel cells. They also observed water presence at downstream locations caused by diminished gas flowrates. Additionally, by observing flooding patterns in the cathode gas channels of a transparent PEMFCs [132], patterns of single-phase flow, droplet flow, film flow and slug flow were identified. Water droplets that emerge from underneath the saturated GDL eventually contact with neighbouring droplets to form a wavy-motion film. In turn, the films eventually grow and accumulate into a slow-moving slug. Additionally, more exotic studies employed optical diagnostics to correlate flooding to temperature distribution [118] and mitigate flooding with a water absorption layer [122].

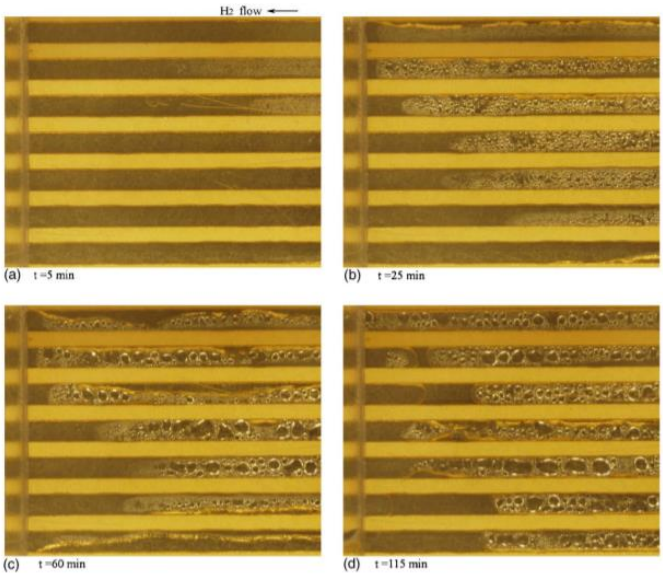

Figure 2.12 – Sequential images of water droplets and films in the anode. PTFE-proofed carbon paper is used as anode GDL. The view is in the outlet portion of the flow field. Adapted from [123]**.**

Optical diagnostics coupled with fluorescence microscopy can provide insights into the ex-situ microscale transport of liquid water and droplet formation across the GDL. By injecting a dye solution through a GDL, preferential pathways for liquid water transport were identified through the opaque, fibrous structure (Figure 2.13) [133] [134]. Additionally, the effect of GDL compression was investigated [129] [134]. The authors found that damage caused by compression led to localised regions of hydrophilic surfaces, which in time resulted in dynamic and interconnected network of water pathways within the GDL.

Optical diagnostics is the most widespread water visualisation technique for transparent PEMFCs, which can provide critical information on two-phase flow phenomena and the impact of parameters such as GDL structures, flow field configurations and process conditions on water transport and accumulation inside gas flow channels. These insights are collected using cost effective devices with high spatial resolution and frame rate which are universally available and simple to set-up and operate. However, incorporation of transparent windows may prove to be challenging and even undesirable for certain studies, as it significantly affects surface chemistry of the channels and the actual phenomenon under study. Additionally, the lack of contrast of visible light towards liquid water and droplet condensation on the transparent windows can lead to misinterpretation of the results [17]. Finally, coupling with fluorescence microscopy is attractive for ex situ studies of water transport inside the GDL, but is yet to be demonstrated in an operating PEMFC.

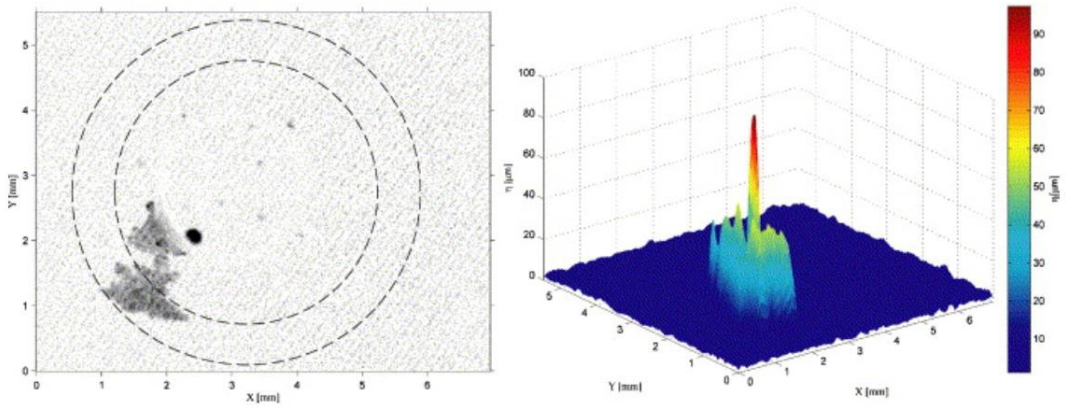

Figure 2.13 – Digital images from fluorescence microscopy showing the evolution of water transport after 7 seconds. The image to the left has been inverted for clarity, with the areas compressed by the O-ring shown as the area between the concentric dashed circles. To the right, there is a three-dimensional rendering of signal intensity. Adapted from [134]**.**

2.3.5. Infrared imaging

Infrared light is a form of electromagnetic radiation with situated broadly within the frequency band between 430 THz and 0.3 THz. It was discovered by Sir William Herschel in 1800, and finds applications in spectroscopy, night vision and thermography. Research on infrared imaging for PEMFC has been typically focused on the latter to obtain temperature distributions [118], [135]–[138]. In particular it has been used to find localised hotspots due to reaction heat in the GDL and MEA [118] [137] and sub-zero water dynamics including phase change (Figure 2.14) [135] [136]. For flooding diagnostics, it has been performed using an infrared camera with 5 μm pixel resolution and 30 Hz frame rate, where a water film and condensation in both anode and cathode channels could be observed [139]. Despite having a low level of development in this topic and the requirement for a transparent fuel cell, infrared imaging could become a powerful flooding diagnostic tool due to inherent sensitivity to the vibrational motions of intermolecular bonds in water molecules combined with modern infrared devices with high spatial resolution and frame rate. However, this sensitivity also means that infrared beam attenuation in environments with large water contents will be limited, compromising the feasibility of the technique. Additionally, all matter above the absolute zero emit infrared radiation, and at PEMFC typical operating temperature of approximately 80 °C and 100-200 °C for high temperature PEMFCs [140] background noise from surrounding emissions can be a significant source of uncertainty.

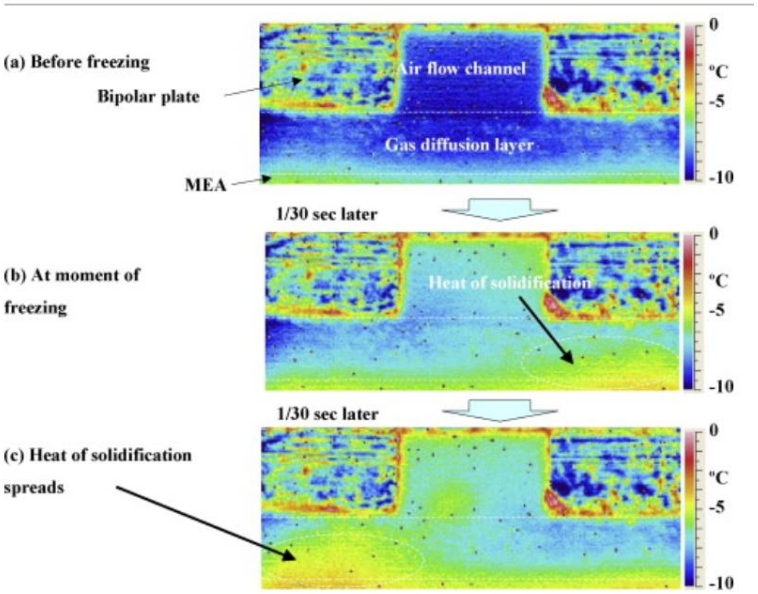

Figure 2.14 – Infrared images inside PEMFC cross-section: (a) before freezing, (b) at moment of freezing, and (c) 1/30 s after freezing. Adapted from [136]***.***

2.4. Terahertz radiation

Terahertz radiation is situated between the infrared and microwave regions of the electromagnetic spectrum. The terahertz region is commonly defined to include the band of frequencies ranging from 0.1 to 10 THz, where 1 THz corresponds to 10^{12} Hz. In terms of other frequently used units, this range corresponds to the following: wavelength λ (0.03-3 mm); wavenumber k (3.3-334 cm^{-1}); period τ (0.1-10 ps); photon energy E (0.4-41 meV) and temperature T (4.8-478 K) [141], as shown in Figure 2.15.

The terahertz frequency band is often referred to as the "Terahertz gap" owing to the limited accessibility by optical, thermal and electronic techniques commonly employed in adjacent frequency bands [142]. At lower frequencies (microwaves), radiation is generated using oscillating circuits based on high-speed transistors and at higher frequencies (infrared) it is generated via semiconductor lasers based on optical fibres. However, transistors and other solid-state electronics are theoretically limited at about 300 gigahertz (GHz) and semiconductor lasers can only be extended down to about 30 THz [25], [143].

Terahertz shares properties with neighbouring infrared and microwave bands. Like infrared and microwaves, terahertz light is non-ionising and travels in a line a sight. Further, terahertz penetrates through a wide range of dielectric materials, such as clothing, paper, plastics, with typically less penetration depth compared to microwaves [25]. However, terahertz has limited penetration through water and metals. A corollary of the former condition is that terahertz

radiation has limited penetration through fog, clouds and suffers from high atmospheric absorption due to the presence of water molecules in the atmosphere. This caused significant hindrance on early terahertz funding and interest [144]. Nevertheless, the peculiar nature of field-matter interactions induced by terahertz radiation makes it a promising regime for investigation of the natural world. Many compounds possess very specific electromagnetic resonances arising from their molecular structure, such as vibrational and rotational modes, lying in the terahertz region [145].

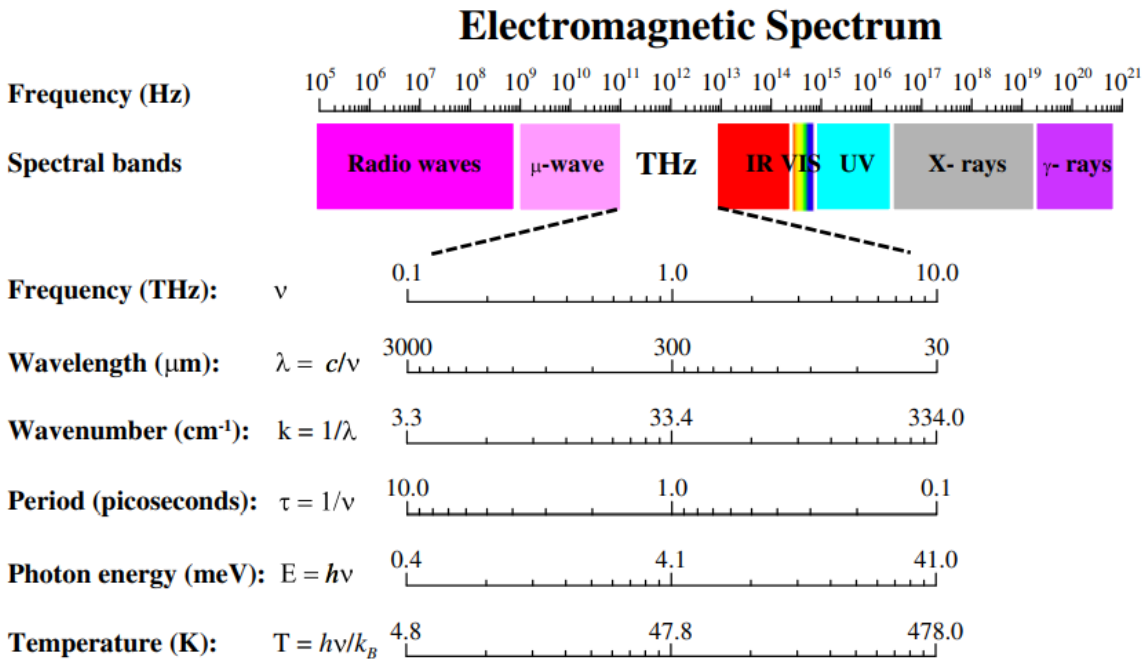

Figure 2.15 – The terahertz band of the electromagnetic spectrum. Adapted from [141]**.**

From a historical perspective, investigations within the terahertz frequency range were restricted for a long time to niche scientific environments, such as synchrotron facilities and free electron lasers, with few relevant scientific applications due to the massively bulky nature and unwieldy cost of these facilities. The advent of terahertz science as an emerging domain can be certainly connected to the mainstream availability of cost-effective generation devices and techniques, which can be traced back to the demonstration of the first laser in 1960 by Theodore Mainman [146]. Many important breakthroughs were achieved in the terahertz fields such as the first demonstration of mode-locked lasers [147] and the development electrical discharge and optically pumped terahertz gas lasers [148], [149] in the 1960s, followed by terahertz generation via nonlinear optics [150], [151] in the 1970s, but the field remained relatively small across the 1980s. However, in the late 1980s, a new spectroscopic tool was established when methods were developed for using ultrafast laser sources to both generate and

detect freely propagating terahertz pulses [19]–[22]. This proved to be a major revolution in the field, as it dramatically lowered the barrier for new researchers, especially with the decreasing cost and complexity of commercial femtosecond laser systems. Since then, the popularity of terahertz has increased tremendously, evidenced by the exponential growth of publications mentioning “terahertz” in their contents (Figure 2.16) [152].

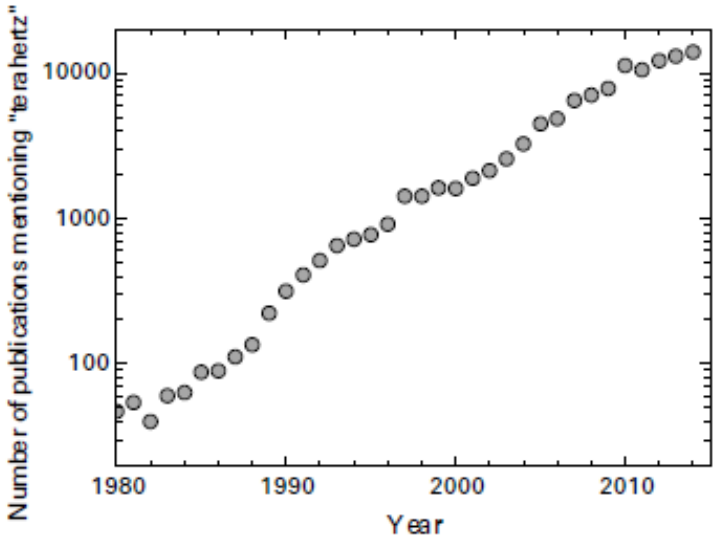

Figure 2.16 – The yearly number of publications mentioning “terahertz” in their contents. Adapted from [152]**.**

Amongst the many realisations of terahertz techniques, two major types of systems can be distinguished: narrowband systems, commonly known as CW systems and broadband systems, which mainly consist of THz-TDS [153].

THz-TDS systems are unique in their way of measurement. Other spectroscopic techniques such as Infrared-Visible-Ultraviolet spectrometers or vector network analysers perform measurement directly in the frequency domain, while Fourier Transform Infrared spectroscopy measures indirectly in the time-domain via interferometry. In contrast, THz-TDS systems are based on the generation and coherent detection of sub-picosecond pulses of electromagnetic radiation, which are broadband in nature, and measure the amplitude and phase changes caused by the sample material directly in the time-domain, in both reflection and transmission geometries. This allows for the extraction of optical properties such as refractive index, permittivity and absorption coefficient without the need for Kramers-Kronig transformation [154], as well as spectroscopic analysis of chemical compositions, and thickness and depth information of layered structures. For these reasons, THz-TDS is a versatile technique and the leading measurement modality in this portion of the electromagnetic spectrum [155].

On the other hand, CW systems use single-frequency or small bandwidth CWs of THz radiation to measure a sample material's properties, based on the signal amplitude variations. Although CW systems usually don't yield depth, frequency-domain or time-domain information like the THz-TDS systems, they are the first choice when sharp spectral features are of interest and a frequency resolution < 50 MHz is desired [155]. Additionally, the complexity of the optics can be greatly reduced when compared to THz-TDS systems, resulting in faster measurements and devices with reduced size and cost [156]. CW terahertz radiation can be generated using electronic sources such as Gunn, IMPATT and resonant tunnelling diodes or optically by photo mixing [157].

2.4.1. Terahertz systems

Terahertz time-domain spectroscopy

THz-TDS can be performed in reflection or transmission geometry. In both modes, the absorption coefficient and refractive index can be calculated from the time delay and attenuation of individual frequency components.

The main components of a THz-TDS system include a terahertz emitter, a terahertz detector, an ultrafast (femtosecond) laser source, a beam splitter, a delay line and sets of collimating and focusing lenses and parabolic mirrors. Typical THz-TDS system in both transmission and reflection geometries are shown in Figure 2.17a and Figure 2.17b, respectively. The emitter is usually a photoconductive antenna (PCA) consisting of a micro-antenna fabricated on a semiconductor substrate with a short carrier lifetime, such as GaAs. The detector is usually another PCA or a non-linear crystal such as ZnTe that favours optical polarisation in one direction. Any femtosecond laser can be used if its photon energy is higher than the bandgap of the semiconductor substrate [144]. For low temperature grown GaAs, titanium:sapphire or Erbium-doped fibre laser are adequate [155]. During operation, the laser initially emits a short pulse in the femtosecond range. The ultrafast optical pulse is divided by the beam splitter into a pump beam and a probe beam. The former optically excites the THz emitter (biased PCA), thus emitting a picosecond THz pulse which is then collimated and focused onto a sample using sets of optical lenses and parabolic mirrors. The transmitted or reflected pulse is then collected and focused onto the THz detector, which is an unbiased PCA, for laser gated terahertz detection [158]. By rapidly sweeping a mechanical delay line, the transient terahertz electric field can be traced out, thereby reconstructing the entire THz waveform in the time-domain.

The advantages of this sampling approach are excellent reproducibility, low jitter, and low noise at the cost of slow measurement speed. Opto-electronic delay methods are less popular but can provide extremely fast data acquisition, although at a reduced signal-to-noise ratio. The time-resolved THz pulse can be easily converted into a wideband THz spectrum via Fourier transform [159], as seen in Figure 2.18. Nowadays, commercial THz-TDS instruments are relatively compact, robust, flexible and comparable in price to other types of optical instrumentation, such as spectrometers and Raman systems, and suitable for installations in an industrial environment [160]. Examples of these devices are the MenloSystems TERA K15, Toptica TeraFlash pro or the Hubner Photonics T-SPECTRALYZER®. Specifications on these devices include a spectral range of 5-6 THz spectral range, 90 dB dynamic range and 1.2 GHz THz frequency resolution.

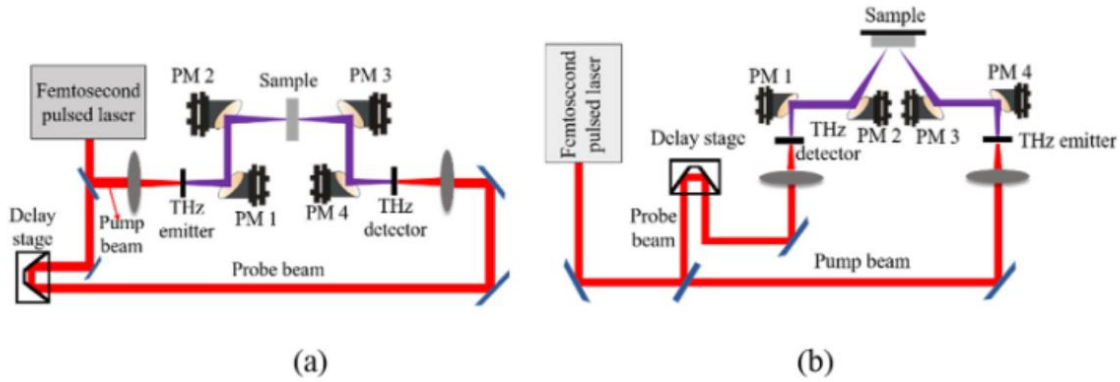

Figure 2.17 – Typical THz-TDS systems in (a) transmission and (b) reflection geometries. PM stands for parabolic mirror. Adapted from [161]**.**

A critical development for making THz-TDS systems more practical for industrial applications, is to move away from free-space optics, where the femtosecond laser is guided and focused using optics, to fibre optic coupled devices. The main challenge is maintaining the short pulses and sufficient power through the fibre optic. An example application of fibre-coupled THz sensors is in-line quality control of a pharmaceutical tablet coating process [162].

Terahertz continuous wave generation systems

CW terahertz light can be generated via solid-state devices, optical devices, or a combination of both.

Quantum-cascade lasers (QCLs) are semiconductor lasers operating under different physical principles than traditional semiconductor diode lasers [163]. The latter achieve emission through electron-hole recombination between the conduction and the valence band, thus the

emission wavelength is dependent upon the bandgap energy of the material. QCLs can output radiation with high power at long wavelengths through a combination of both quantum and cascade effects: QCL's emission wavelength is decoupled from the bandgap energy by forming sub bands in the conduction band, allowing for stimulated emission to occur within the conduction band itself. This process is known as intersubband transition [164]. When combined with a sloped potential bias, a single electrode can cascade through the quantum well structure and emit multiple photons. QCLs were first proposed in 1971 [165] and first demonstrated in 1994 [163]. The first terahertz QCL was demonstrated in 2002 [166], operating at 50 K, 4.4 THz and 2 mW.

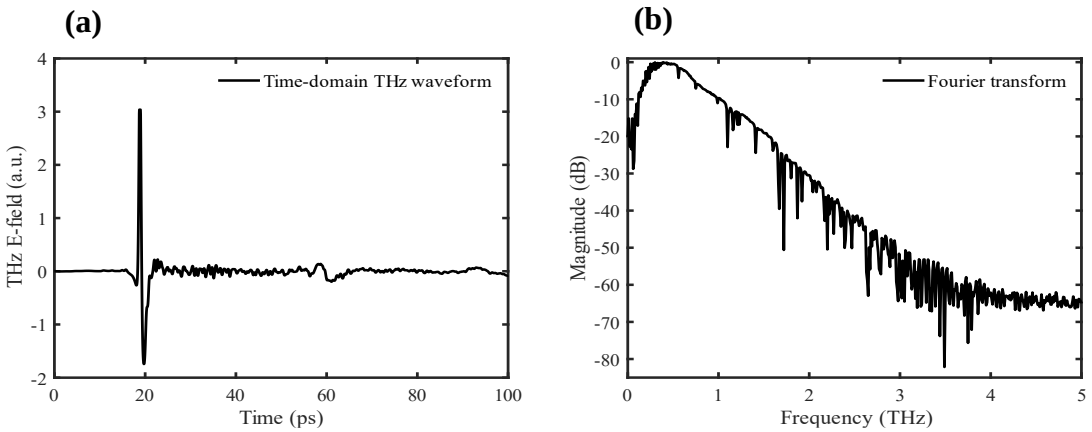

Figure 2.18 – (a) Raw THz waveform in the time-domain and (b) corresponding Fourier transform in the frequency-domain.

Photo mixing combines optics and electronics to generate terahertz waves, where two CW lasers of slightly detuned frequencies are overlapped in a photo mixer, usually an ultra-fast semiconductor material such as GaAs, which outputs terahertz waves by means of an antenna. The main advantage of photo mixing is that the output frequency is the high tunability achieved by changing the frequency difference between the lasers. On the other hand, the main disadvantage of this method is the low output power compared to other CW techniques. Extensive overview on this subject can be found in [157].

Parametric conversion uses optical means to generate highly tunable (0.7-3 THz) CW terahertz waves by pumping a non-linear optical crystal (e.g. $LiNbO_3$) by a nanosecond pulsed laser, producing polariton scattering [167].

Frequency multipliers are an electronic technique for obtaining CW terahertz waves, where the frequency of a driver source, such as Gunn oscillators, is multiplied in a nonlinear device, such as a Schottky diode [168], to generate a higher-order harmonic (multiple) of the input frequency. General details on this can be found in [169].

CW terahertz emitters can also be based on IMPATT technology. IMPATT diodes have been around since the 1960s [170] and are the leading solid-state devices for microwave and millimetre-wave generation [171]. These diodes are reverse biased to produced electron-hole pairs in the depleted region of a semiconductor and contain either a single-drift region (SDR), consisting of a single p-n layer or a double-drift region (DDR), consisting of a p^+-p-n-n^+ multilayer structure [172]. The DDR is superior to the SDR because the two drift zones enable higher drift zone voltages that allow for higher direct current to radio-frequency conversion efficiency and higher radio-frequency power output [171], [172]. The transit time is the time taken for the carriers to cross the depletion layer, and the thicknesses, materials and doping levels of the semiconductor layers are chosen based on the transit time required to obtain a particular frequency [171], [172]. Devices operating at approximately 100 GHz commonly use Si as the semiconductor material [172]. At terahertz frequencies it was found that GaAs, Si, InP, 4H-SiC and Wz-GaN have been explored for semiconductor materials in IMPATT devices, the latter two being the best candidates to potentially generate terahertz radiation up to 5 THz [171]. Figure 2.19 displays a 0.1 THz IMPATT diode-based THz emitter, operating at 10 mW output power and commercialised by Terasense Inc., based in CA, USA, which is the main terahertz source used in the experimental work conducted as a part of this Dissertation.

Figure 2.19 - 0.1 THz Terasense terahertz emitter, based on IMPATT diode technology.

Terahertz cameras

In imaging applications, terahertz FPA cameras provide a faster alternative to raster scanning (point by point scanning over a large area) that allows real-time imaging study of transient processes over a large area but can come at the price of decreased sensitivity compared to THz-TDS spectrometers. The source of illumination can be a broadband pulse [173]–[175] or narrowband CW [176].

THz imaging with microbolometer arrays, whose array elements infrared microbolometers made of vanadium oxide, has been demonstrated [177]. For illumination, a CO_2 laser was used, although QCL has also been demonstrated. Institutions such as CEA-LETI, Institut National d'Optique, and Swiss Terahertz are actively developing microbolometer-based FPAs.

Other array elements include field-effect transistor (FET)-based cameras [178], Schottky barrier diodes [179], [180], pyroelectric crystals [181]–[183], microelectromechanical systems [184] and superconducting films [185]. In particular, FET-based cameras, whose detection scheme is based on terahertz wave interaction with plasma oscillations in the transistor's channels, are considered as the most promising technique for mass adoption [186].

In the experimental work for this Dissertation, the Tera-256 model detector from Terasense was used (Figure 2.20). It consists of a terahertz FPA camera consisting of an array of 16x16 pixels, with each pixel having dimensions of 1.5x1.5 mm. Its function is like a charge-coupled device camera and is fabricated from a GaAs high-mobility hetero-structure, with the imaging sensor mounted on a single wafer. It detects terahertz radiation by using a two-dimensional electron system. Incoming terahertz radiation is received by an antenna, and this induces plasma oscillations in the heterostructure. If the terahertz frequencies match the plasma oscillation frequency, a large drop in the AC potential across the depletion region of the semiconductor results in high values of rectified induced current. This enables a high response in the detectivity at the plasma frequency [187]. At room temperature, the Tera-256 detector has a responsivity of 50 kV/W, and a noise-equivalent-power (NEP) of 1 $nW/Hz^{0.5}$. Exact details into the manufacturing of the Tera-256 model detector are not given on the company's website, however, they may be similar to detectors designed by Muravev and Kukushkin [188].

Figure 2.20 – Terasense Tera-256 terahertz FPA camera.

2.4.2. Industrial applications

Pharmaceutical coating analysis

One of the foremost applications of terahertz technology occurs in pharmaceutical manufacturing. film coating on solid oral dosage forms, especially for tablets, is typically performed as the last steps of secondary manufacturing value chain. Coatings are usually applied to cores such as tablets or pellets and in cases small particles such as crystals. Functional coating can be used to ensure colour uniformity, light protection, taste masking, protect the active pharmaceutical ingredient (API) against the acidic environment of the stomach or the gastric mucosa against an aggressive API, and to prolong API release. Coating thickness are important especially for functional coatings. A minimum thickness and the absence of cracks are required to ensure gastro resistance of a dosage form. Defects in the coating can lead to dose dumping can lead to spontaneous release of the drug leading to possible toxic side effects. For the last fifteen years, terahertz pulsed imaging (TPI) has received a rapid growth in the level of scientific interest to assess pharmaceutical coating quality. Figure 2.21a shows a schematic diagram of a TPI instrument.

Imaging of pharmaceutical dosage forms using THz radiation is suitable because most coating materials do not exhibit any distinct spectral features while being semi-transparent to terahertz radiation. This therefore makes it possible to conduct non-destructive imaging at depth. In a standard measurement, the terahertz pulses that are incident on the tablet surface will penetrate through the underlying coatings. At each coating interface or abrupt change in refractive index between drug particles and excipient matrix, a portion of the terahertz pulse reflects to the detector. This in turn provides the necessary contrast to differentiate between structural layers or subsurface structures within the tablet. Film coating thickness is determined by the separation of adjacent reflection peaks in the processed signal, given by $d = c\Delta t/(2n)$, where d is the coating thickness, c is the speed of light, Δt is the peak separation time and n is the refractive index of the coating material. The refractive index can be estimated either from the strength of the primary reflection using Fresnel's equations [189], an independent measurement using techniques such as X-ray microtomography [190] or precisely using THz-TDS, for determining the absolute film coating thickness. An example of a 3D coating thickness image is displayed in Figure 2.21b.

TPI has been used for several types of off-line measurements, such as coating morphology, density, and drug release analysis, as well as defects identification. In the pioneering work by

Fitzgerald et al. [191], TPI was used to analyse coating thickness of commercially available ibuprofen tablets. By raster scanning the terahertz beam across a 1 x 1 mm square section of the tablet at 50 µm steps, TPI was able to resolve different coating layers, measure overall thicknesses, and distinguish between single- and multicoated tablets from different manufacturers. These results were in good agreement with destructive optical microscopy measurements. The success of this work led to the development of TPI for surface imaging of arbitrary shaped tablets automatically [192]. This in turn provided information on the spatial and statistical distribution of coating thickness for a wide range of products such as film-coated tablets, sugar-coated tablets, multi-layered controlled release tablets and soft gelatine capsules. TPI was also used to image delayed release tablets, which aim to control the site of drug release, for example oesophagus, intestine or colon, where average coating thickness correlated well against dissolution behaviour under simulated gastric pH conditions [193]. A number of studies have also taken advantage of TPI to penetrate through the coating structures to identify coatings defects in sustained-release coats, which allows for a predetermined API release rate for extended time period, first demonstrated by Ho et al. [194]. This work has been extended to detecting cracks between layers in bilayer tablets [195] and in coatings stored at high temperatures (60-70°C) [196], revealing structural defects in enteric coatings (prevent dissolution or disintegration in gastric environment) [197] and resolving air gaps to assess adhesion quality between core and coatings in calendered tablets [198]. An extensive overview of studies on TPI for pharmaceutical coating applications can be found in [199].

(a) **(b)**

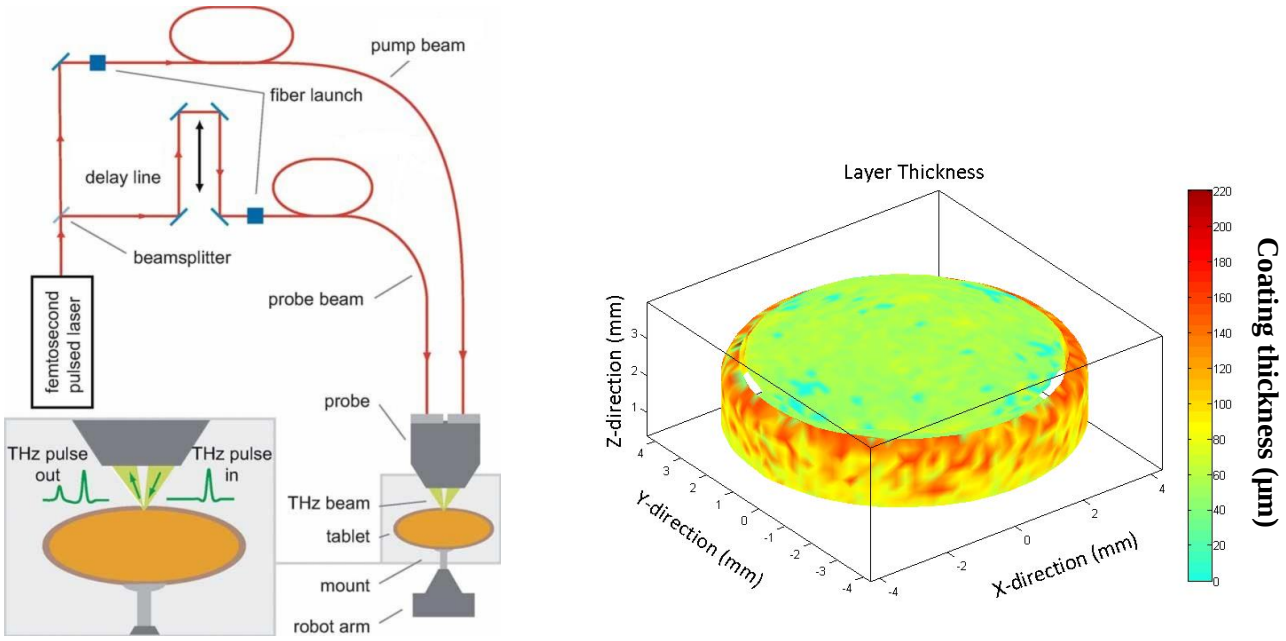

Figure 2.21 – (a) Schematic of terahertz pulsed imaging (TPI). (b) Three-dimensional (3D) coating thickness image of one face and centre band of a biconvex tablet. The coating layer is thicker on the centre band than on the top face of the tablet. The false colour bar refers to the coating layer thickness, in µm scale. Adapted from [192]***.***

Liquid water detection and mapping

Researchers who are unfamiliar with terahertz technology typically first learn two basic facts concerning the propagation of terahertz: it does not penetrate easily through metals nor polar molecules such as water. While these facts do pose some limitations for terahertz technology, for example when it is applied for wireless communications [200], [201], most materials which absorb moisture are semi-transparent, such as plastics [202] or paper [203].Thus, there is a high contrast between "hydrated" and "dry" areas of the material, which enables detection and diffusion mapping of the liquid using terahertz sensing.

Paper

The moisture content of paper is an important parameter in its fabrication process. The quality of the paper is strongly determined by the drying process which requires online monitoring of the moisture content during paper production [203]. Non-uniform distribution of moisture and high moisture content affect the shrinkage and strength properties of the paper and can induce a myriad of problems including tearing, curling, wrinkling or fracturing of the paper [204]. In the paper industry, currently implemented technologies for moisture sensing do not yield spatially resolved information on moisture distribution, and, given that dry paper has low terahertz absorption, terahertz sensing can be a solution.

Laboratory studies demonstrated diagnosing moisture content [203], simultaneous measurements of thickness and moisture [205], [206] and multiple parameter estimation (including moisture content) [207]–[211]. In general, authors were able to spatially resolve water content in paper sheets using raster scanning terahertz imaging (Figure 2.22a) [203] and distinguish vacuum-dried paper, common dry paper and paper after exposure to ambient moisture with THz-TDS [205]–[207] (Figure 2.22b). Vassilev et al. [212] demonstrated a prototype terahertz sensor operating at 0.2 THz for in-line contactless measurement of water content in paper at the drier stage of a paper making machine. The sensor measured water content over an area of 4 cm^2 and the observed variations in moisture content agreed well with data from a simultaneous microwave resonator sensor as well as off-line laboratory measured samples of the paper.

Wood

Wood has also been investigated with terahertz techniques, although it is less transparent to hertz waves than paper due in part to the larger thickness of samples and a stronger contribution from scattering. The monitoring of moisture in wood timbers is an important manufacturing parameter, since excess moisture accelerates the wood's degradation, while low levels of moisture in timbers can improve the material's mechanical strength. Inagaki et al. [213], [214] has developed a method for simultaneous moisture content and density using THz-TDS, by correlating them to real and imaginary components of complex permittivity from four different species (aspen, birch, hemlock and maple). Furthermore, an example of water mapping in wood using terahertz imaging with a CW source and a FPA detector [215] is shown in Figure 2.23. Here, a 14.2 mm thick spruce sample is injected with 1.55 g of water into an area of about 3.5 cm^2, highlighted by an arrow in the THz false colour image (Figure 2.23b). As the sample dries at room temperature, it slowly loses 90% of the injected water. THz techniques have also been used to detect orientation of the aligned fibres [216]–[218] as well as beetle [219] and termite damage [220]–[222].

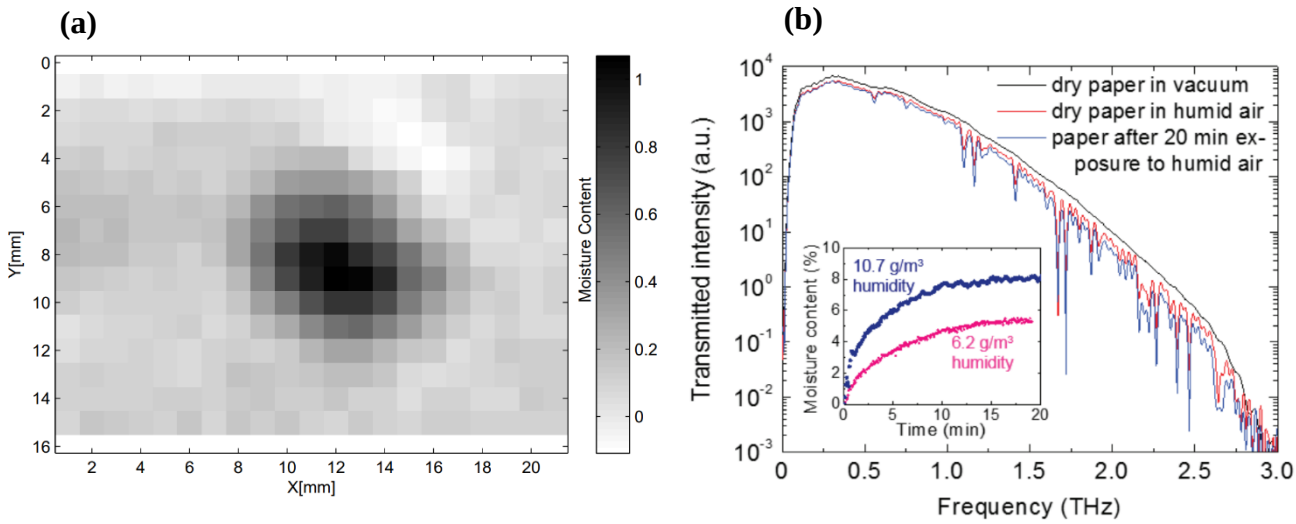

Figure 2.22 – (a) Raster scanned transmission image through 80 g/m² paper at 0.6 THz showing the distribution of water in terms of moisture content (absolute values of kg water per kg fibre). Adapted from [203]***. (b) Terahertz frequency domain spectra of dry 280 g/m² paper in vacuum and humid air, as well as moist paper in humid air. The inset shows the moisture content of paper absorbing atmospheric humidity at two humidity levels as a function of time. Adapted from*** [207]***.***

Leaves

Water is an essential component in the physiological process of plants, which participates in the various activities such as hydrolysis, photosynthesis, transpiration and nutrient transport [223], [224]. The detection of leaf water content and distribution is of high importance for numerous aspects in plant science, including physiological condition, irrigation management,

and drought stress [225]. Much research attention has been directed towards terahertz imaging and sensing techniques [226], such as THz-TDS [227], confocal microscopy [228] and QCL [229]. These recent technologies can help us obtain non-invasive, fast, and reliable assessments of leaf hydration status. terahertz radiation is particularly promising thanks to the high water absorption coefficient and the relatively low absorption coefficient of the leaf dry-matter content [230], [231]. The particularly long wavelength makes this type of radiation relatively insensitive to scattering from leaf dry mass; consequently, terahertz imaging has proven to be an effective tool for non-invasive monitoring of plant water content [232]–[234]. Moreover, terahertz imaging can be used for mapping water density in single leaves [228], [235], for carrying out time-lapse studies on leaf and trunk hydration dynamics [236], [237], and for monitoring plant drought stress response [238]. Other spectral methods such as infrared spectroscopy [239], [240] and hyperspectral spectroscopy [241] are currently used to obtain a large amount of useful information (i.e. water data), but their approach is indirect where they require particular wavelengths or combinations of indices in order to obtain a strong correlation with actual water data. Particularly, Cumis et al. [228] exemplified the high resolution capability of a terahertz confocal microscope based on a QCL source by imaging a fresh green leaf, shown in Figure 2.24a. The original terahertz picture is seen in Figure 2.24b, and a close-up of the highlighted region is shown in Figure 2.24c, where the veins and other details can be seen with high definition.

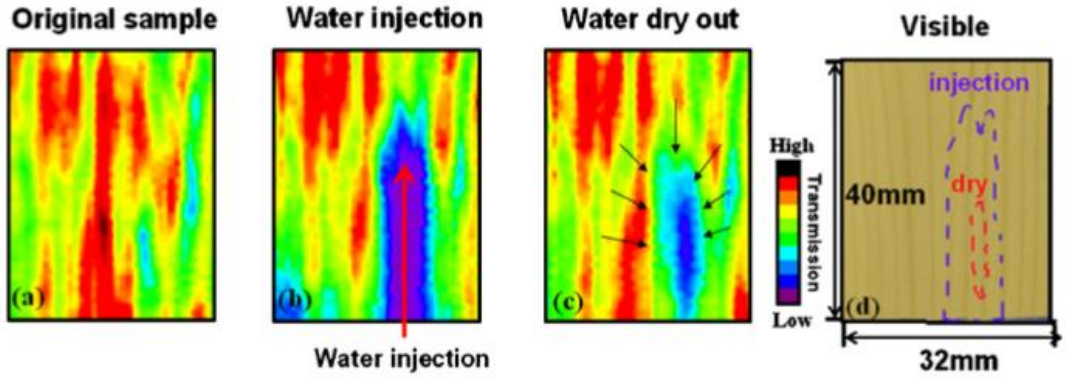

Figure 2.23 – (a) THz transmission image of the spruce wood sample. (b) Same sample after localised injection of water. (c) THz imaging after sample loses 90% of injected water by weight. (d) Visible image of sample. Adapted from [215]**.**

PEMFC related systems

Although terahertz sensing is unknown in the field of PEMFCs and other electrochemical systems, a few studies were performed that explore this perspective. Nemes et al. [242]

developed a terahertz-transparent three electrode cell to perform spectroelectrochemistry of a SnO_2 thin film. Spectroelectrochemistry couples spectroscopic and electrochemical measurements to identify chromic changes as a function of applied chemical potential [243]. Using THz-TDS, they demonstrated a decrease in terahertz transmission under a variety of bias voltages corresponding to potentials where SnO_2 conduction bands are potentiostatically filled. This highlights the unique ability of THz radiation to distinguish between mobile and nonmobile electrons, which can be particularly useful in semiconductor material studies.

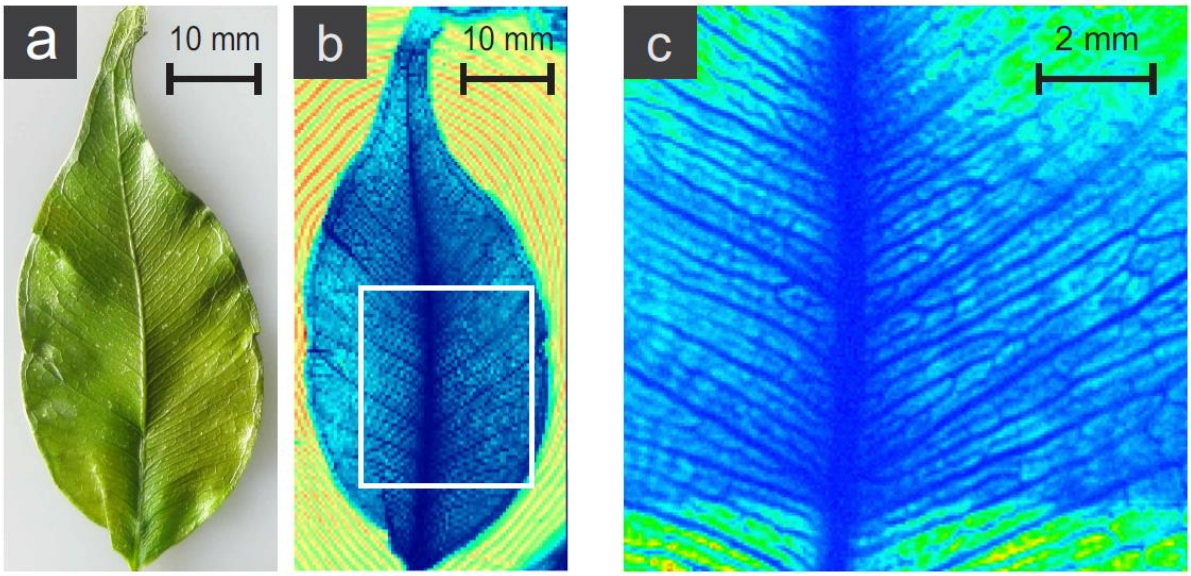

Figure 2.24 – (a) Photograph of a fresh leaf. (b) Confocal terahertz image of the same leaf with intensity levels referring to a wide chromatic range, to highlight the veins. The measurements covered an area 1.8 mm x 3.2 mm and 90x160 pixels were recorded. (c) The rectangular white frame in panel (b) is imaged again with more points (200x200 pixels), to obtain a high-resolution close-up of the leaf: the considerable number of details shows the noteworthy capabilities of the instrument. Adapted from [228].

Yurchenko and Zaytsev [244] fitted the complex dielectric data of Nafion in the 0.15-1.5 THz frequency range from THz-TDS, using a double-Debye model. Based on this pioneering work, Ray and Devi have published several studies on the hydration dynamics in PEMs using THz-TDS [245]–[248]. These compared the water retention properties of Nafion compared to other PEM materials such as silica meso-structured cellular foam, meso-structured aluminosilicate with hexagonal network and SPEEK-based membranes. Additionally, they found that UV light exposure improved water retention in SPEEK membranes, to a degree higher than industry standard Nafion. Finally, the authors were able to quantitatively measure water thickness in a Nafion membrane using THz-TDS during a room temperature water desorption process, which correlated well to gravimetric measurements, and distinguish different water modes (bulk, bound and free) inside the Nafion membrane (Figure 2.25a). On a different perspective,

Hagiwara et al. [249] developed a terahertz chemical microscope, based on reflection geometry THz-TDS, to visualise chemical reactions in PEMFCs by measuring variations in terahertz intensity caused by chemical or surface potential changes.

Thamboon and Buaphad et al. [250], [251] employed femtoelectron-based CW terahertz reflection imaging to image liquid water in 2 mm wide flow channels of non-operating PEMFCs, shown in Figure 2.25b. An obvious contrast between water-filled and air-filled channels can be observed.

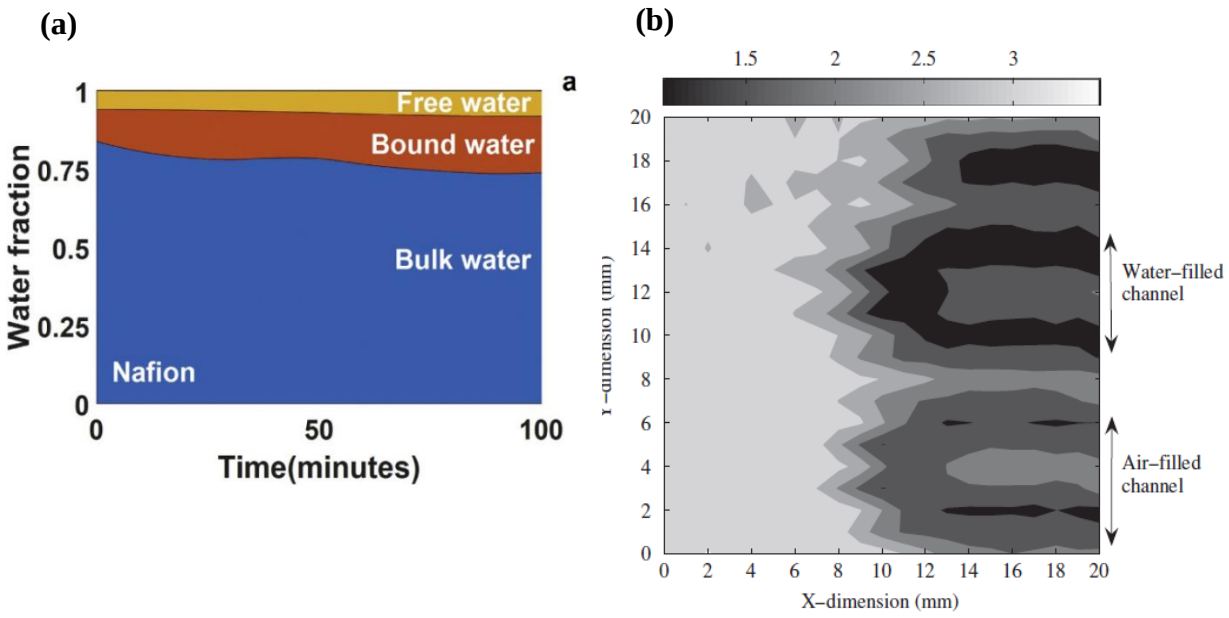

Figure 2.25 – (a) Relative water fractions for Nafion showing the relative fraction of bulk, bound and free water in hydrated membranes with time when the membrane is placed in ambient atmosphere. Adapted from [247]***. (b) THz raster-scanned image of machined channels filled with water and air in a non-operating PEMFC. Adapted from*** [251]***.***

2.5. Summary

Adequate water management strategies are critical to guarantee that the PEMFC reaches and maintains optimal performance, by ensuring sufficient supply of reactant gases to electrocatalyst sites and that the Nafion PEM stays sufficiently hydrated. Water accumulation and transport inside a PEMFC can be characterised by visualisation techniques, and the key techniques have been thoroughly reviewed in this Chapter. In sum, MRI, neutron imaging, and x-ray imaging/tomography techniques can image through visually opaque components such as the GDL and flow channels [110], thus providing in-situ information on liquid water transport in traditional fuel cells. However, main restrictions to these techniques are underpinned by equipment availability and frame rate, with the example of MRI requiring 50 s to acquire an

image. Optical diagnostics and infrared imaging can visualise liquid water through modified transparent PEMFCs and provide information on two-phase flow regimes in the gas channels [132] at relatively high frame rate and spatial resolutions (30 Hz, and 5 μm, respectively). A key drawback is the opacity of common PEMFC components in the visible and infrared portion of the electromagnetic spectrum. Additionally, the lack of contrast of visible light towards liquid water and limited infrared penetration through samples with high water content are significant hindrances to the development of these techniques. Considering this literature review, it is concluded that there is a necessity for a simple and compact technique that can diagnose flooding with adequate beam penetration and water sensitivity, thus maximising contrast with background PEMFC components. Terahertz radiation is known to be non-ionising, travels in a line of sight, and can penetrate dielectric materials, such as clothing, polymers, and ceramics. Most importantly, terahertz frequencies present absorption bands due to hydrogen bonding, and thus terahertz light is sensitive to water presence. This contrast motivates the use of terahertz sensing for flooding diagnostics in PEMFCs. The recent availability of terahertz cameras based on FPA and compact CW systems such as the IMPATT diode allow for video-rate imaging at terahertz frequencies. This allows to circumvent the necessity of terahertz imaging via raster scanning using more traditional pulsed or CW systems.

3. Experimental methodology

The detailed description of experimental methodology is vital to any scientific study. It ensures the credibility of research, the reproducibility of the experimental methods and guides the reader on how the research is conducted and organised. Therefore, this Chapter will describe in detail the materials, methods and techniques used over the course of the PhD work presented in this Dissertation.

3.1. Introduction

The present Chapter will start by describing the terahertz and optically transparent PEMFC, the reactant gas delivery system and operating conditions for the performed experiments. Secondly, the terahertz transmission imaging system will be detailed, including initial setup and assembly, alignment, and calibration. Additionally, the development of a setup for simultaneous terahertz and gravimetric measurements along with an explanation on data processing algorithms will be reported. Finally, both the hardware and data processing algorithms for the high-resolution optical imaging are also detailed.

3.2. Lab-Scale PEMFC

The experimental setup is shown in Figure 3.1. Grade N5.5 (99.9995% purity) hydrogen (BOC, UK) and compressed air were supplied as gaseous reactants. The flow rates were regulated by mass flow controllers (MCS Series, Alicat Scientific, USA). Both reactant gases were humidified prior to entering the fuel cell by bubbling through deionised water inside in-house fabricated humidification vessels at room temperature and pressure. Assuming saturated conditions inside the humidification vessels [252], reactant gases have a relative humidity of 100%. Antoine's equation is a correlation between water vapor pressure (P^*) and temperature (T) for pure substances:

$$log_{10}(P^*) = A - \frac{B}{C+T} \tag{3.1}$$

where A (6.20963), B (2354.731) and C (7.559) are component specific constants [253]. According to this equation, and assuming saturated conditions inside the humidifiers, the water vapor pressure at 25 ºC is $3.17*10^3$ Pa. Moreover, Dalton's law defines that the total pressure of a non-reactive gas mixture (P_{total}) as a summation of the partial pressure of each species (P_i):

$$P_{total} = \sum_{i=1}^{n} P_i \tag{3.2}$$

Dalton's law can also be expressed using the mole fraction of a gas (x_i):

$$x_i = \frac{P_i}{P_{total}} \tag{3.3}$$

Knowing this, the molar fraction of water is 0.031 mol water per 1 mol hydrogen/air. The weight fraction (w_{H2O}) can be calculated according to the following:

$$w_{H2O} = x_{H2O} * \frac{M_{H_2O}}{M_{gas}} \quad (3.4)$$

where M_{gas} is the molar mass of either gas (2 g/mol for hydrogen and 28.97 g/mol for air). From these calculations, the weight fraction of water in air/hydrogen (i.e. absolute humidity) is 2% (w/w) and 28% (w/w), respectively. Electrochemical measurements of the PEMFC were made using a SP-240 potentiostat (BioLogic, France).

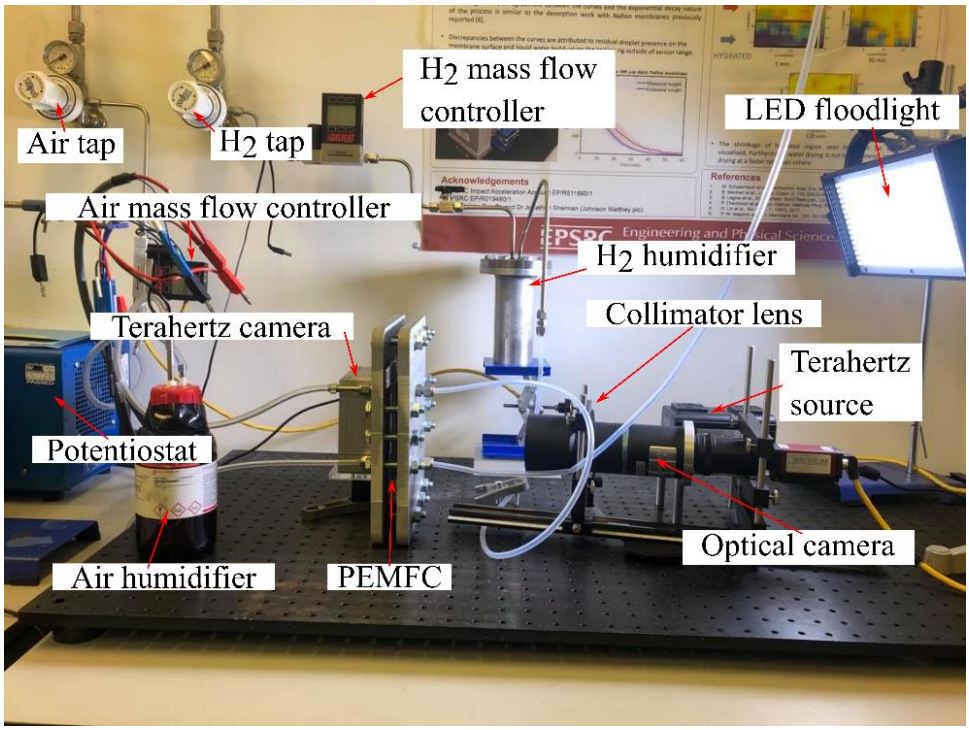

Figure 3.1 – Photograph of the experimental setup.

Figure 3.2 shows the schematic of the PEMFC design used in these studies. The single serpentine flow channels were machined into 1 mm-thick stainless-steel plates with a channel width of 5 mm, length of 100 mm, equally spaced by ribs, with a width of 5 mm. These flow fields also served as current collectors for the PEMFC. The reason for a comparatively wider flow channel than conventional counterparts (≤ 1 mm) is to ensure that water build-up can be imaged by the setup in this feasibility study accounting for diffraction from channel edges, which can distort the measurement. Two terahertz and optically transparent acrylic windows are placed on top of the flow fields to allow for beam transmission through the PEMFC. The fuel cell used a non-laminated membrane electrode assembly that comprise a PEM sandwiched between gas diffusion electrodes (GDE) and GDLs. The incorporation of the GDLs on top of the GDEs is to assist in contacting the gas flow channels and active areas, which can be particularly difficult in a large area fuel cell. The PEM used was a 0.05 mm-thick, Nafion NRE-

212 perfluorinated ion-exchange membrane (Alfa Aesar, UK) and the GDEs were woven carbon cloth substrates with 0.3 mg cm^{-2}, 40% (anode) and 0.5 mg cm^{-2}, 60% (cathode) platinum loading on Vulcan carbon support catalyst with 100 cm^2 area (Fuel Cell Store, USA). The GDLs were Toray carbon papers (TGP-H-090) with 5% (w/w) polytetrafluoroethylene (PTFE) wet proofing (Fuel Cell Store, USA). The Nafion NRE-212 membrane was activated by boiling for 1 h in sulphuric acid and then 1 h in deionized water. This is performed to ensure that positive ions that might be present in the sulfonic acid terminations are replaced with protons. This activation procedure is known to improve membrane water content and proton conductivity [254]. Rubber and PTFE gaskets were used between each of the components for adequate sealing. The complete unit was pressed together using aluminium compression plates and a torque of 15 N m was applied across the assembly (Figures 3.2c-d). For water visualisation, a cut-out of 2.4x2 cm^2 was made on the optical and terahertz opaque layers (compression plates, flow fields, GDEs and GDLs) at the U-turn closest to the outlet (Figure 3.2b). This location was selected for known susceptibility to water accumulation in single serpentine configurations [127], [255], [256]. It is important to note the absence of catalyst/diffusion layers there, so water being visualized is not generated locally, instead generated elsewhere in the fuel cell and emerging from downstream accumulation.

Three experiments were conducted over 300 min at a current density of 0.04 A cm^{-2} in this investigation. The operating conditions of these tests are listed in Table 3.1. The listed flowrates for inlet gases were selected due to stable and repeatable operation of the fuel cell under these circumstances. Furthermore, the stoichiometries were selected to ensure that excess reactant gases are fed into the PEMFC to compensate for the custom-built PEMFC modifications (large channel size, transparent cut-out). These values were chosen based on prior works on visualizing water accumulation in PEMFCs [257]. The cell operated at ambient conditions of temperature and pressure (~ 25 °C and 101.325 kPa) during all experiments. These conditions were selected to maximize water condensation inside the PEMFC, in turn maximizing the potential to image water with the proposed setup. Additionally, these experiments were performed to visualize two-phase flow phenomena under different air inlet conditions. Between each of these experiments, dry air and hydrogen were blown inside the PEMFC through the cathode and anode channels, respectively for approximately 5 min at an open-circuit voltage. Whilst we understand that this would result in electrode degradation over time [258], this was necessary to remove any residual water left inside, ensuring reproducible initial conditions between experiments.

Table 3.1 - Operating conditions of the performed experiments.

Experiment no.	Inlet flow rate / cm^3/min		Stoichiometry		Relative humidity (%)	Absolute humidity (%)		Temperature (ºC)
	H_2	Air	Anode	Cathode		H_2	Air	
Exp. 1	60	300	2.2	3.9				
Exp. 2	60	400	2.2	5.2	100	28	2	25
Exp. 3	60	500	2.2	6.9				

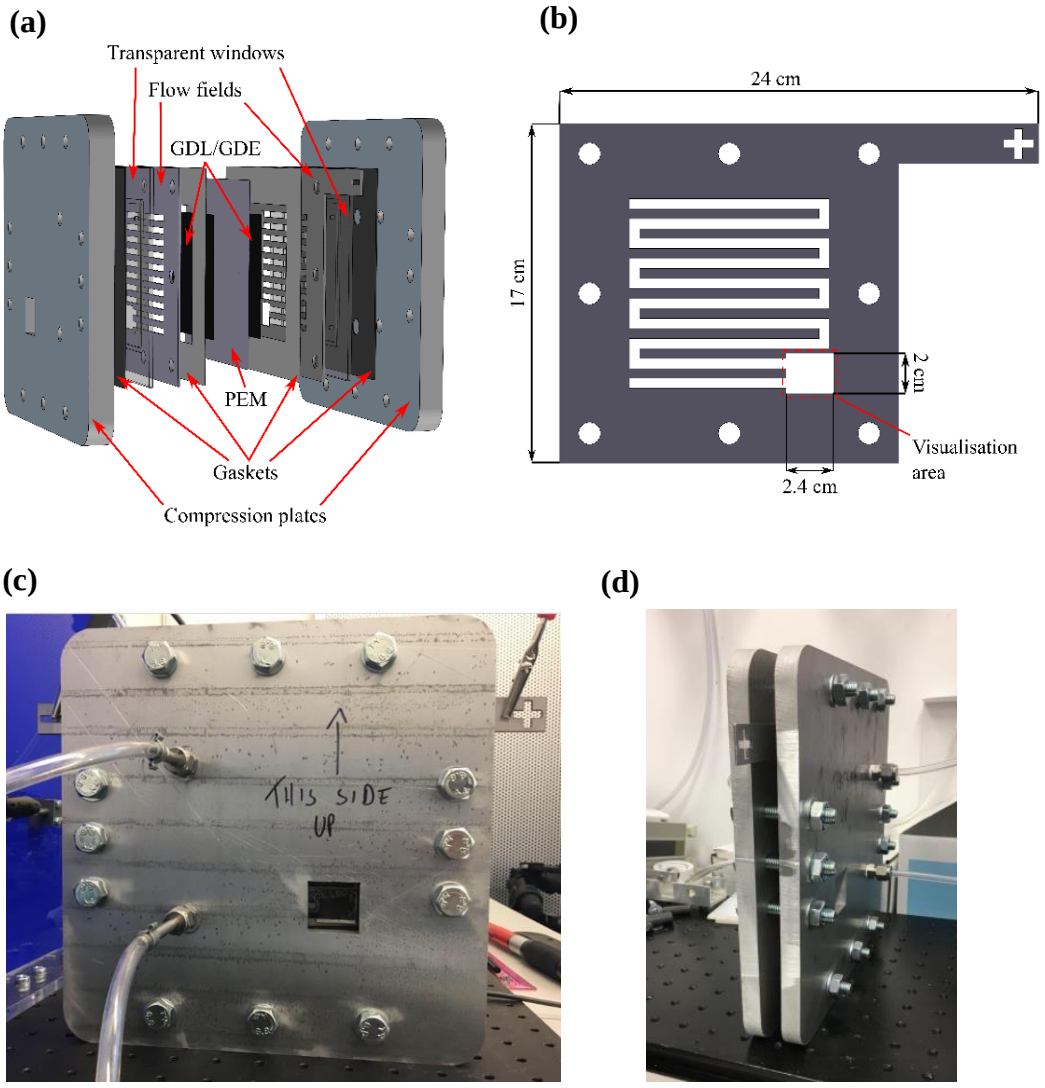

Figure 3.2 - (a) Schematic of the transparent PEMFC. (b) Top view of the flow field plate with highlighted visualisation area. Photographs depicting the (c) front and (d) side views of the PEMFC.

3.3. Terahertz transmission imaging

3.3.1. Materials

The core research described in this Dissertation is based on terahertz video-rate imaging. This was chosen due to terahertz's radiation sensitivity towards liquid water and semi-transparency over common materials, coupled with the imaging system's capacity to capture large areas at video-rate. The imaging system was based on an IMPATT diode narrowband terahertz source, operating at 100 GHz and 100 mW output power (Terasense Inc., USA), a standard gain horn antenna (Mi-Wave, FL, USA) and a 16x16 focal plane array terahertz camera with 1.5 mm pixel size and sensitivity in the 50-700 GHz frequency range (Terasense Inc, USA). The terahertz camera is connected to the PC via USB cable and controlled by Terasense proprietary software. The Terasense software displays the 16x16 pixel array, along with options on exposure time, gamma correction and white/black filters (Figure 3.3). The image is displayed with scaled colours in a jet colourmap. This means that low (< 0.1), average (~ 0.5) and high (1) detected terahertz intensity will be shown as blue, yellow, and red colours, respectively. Furthermore, specific pixels and areas can be selected, and their value or average value respectively will be displayed on the screen.

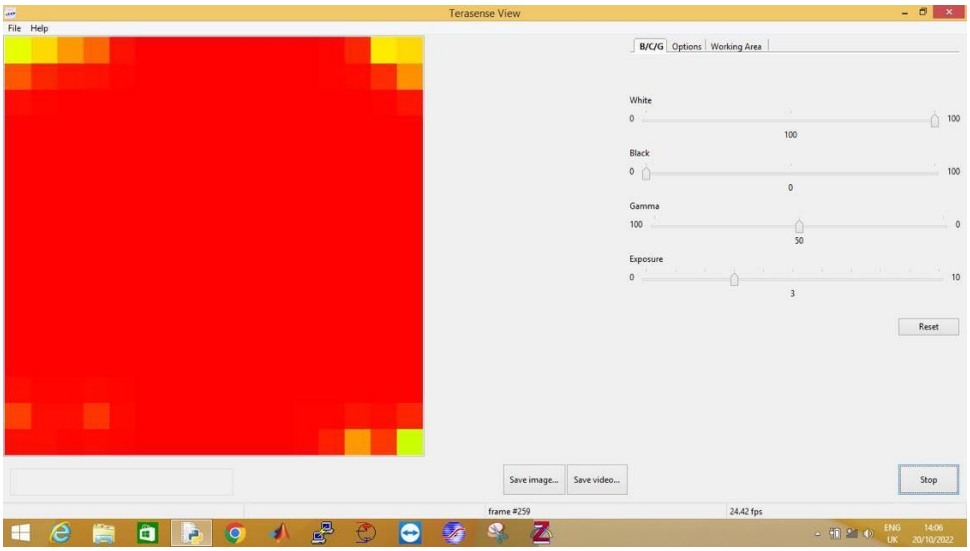

Figure 3.3 – Terasense camera software.

A polymethylpentene (TPX) plano-convex lens with 50.8 mm diameter and 100 mm focal length (Thorlabs Inc., UK) was used for beam collimation. Miscellaneous optomechanical components, such as posts, post holders, irises, clamping forks, and brackets (Thorlabs Inc.,

UK), were used for alignment, calibration, and physical support of imaging devices. Bespoke parts such as aluminium rails and plastic frames were also designed and manufactured in-house for securing samples and physically support imaging devices. The full optical assembly was mounted on an aluminium breadboard (Thorlabs Inc., UK).

3.3.2. Source and camera alignment

To fully exploit the capabilities of the video-rate terahertz camera, it is ideal to achieve a collimated beam that is the same size as the focal plane array. This will allow for each pixel to provide spatial information on water content in the measured samples, as opposed to a focused beam, which condenses information into a single point measurement.

The first step was to elevate the IMPATT source, positioning it on top of a laser-drilled acrylic slab supported by four posts. These posts were bolted to the breadboard. The height of the platform was adjusted depending on the sample's requirements. When turned on, the source emits a divergent terahertz beam through the antenna. To collimate the beam, the TPX lens was positioned one focal length (100 mm) away from the source. The lens and antenna must be well centred and perfectly parallel with each other. The resulting collimated beam is similar in size to the collimating lens.

Secondly, the terahertz camera must be aligned with the collimated terahertz beam. This is achieved by aligning the centre of the camera and the TPX lens with a tape measure. The initial goal was to achieve a complete array of pixels displaying bright red colour.

In similar fashion to the terahertz source, the FPA camera was secured in a laser-drilled acrylic slab. However, in this case the post assembly was such that the camera could be precisely moved in all directions. The edges of the terahertz beam were determined by moving the camera from left to right, and up and down. When the perimeter of the beam is reached, the positions of the four beam corners (left, right, up, down) are noted down and this information is used to put the terahertz camera at the centre of the beam.

The last step is to ensure that the beam is travelling in a straight line from source to camera. This was achieved by placing two irises about 200 mm apart from each other and slightly opening their apertures. The collimating lens height and orientation can be adjusted to ensure that the pixels that correspond to the irises' apertures are bright red. Additionally, these pixels must become increasingly blue as the aperture is closed.

3.3.3. Calibration

Upon ensuring that the terahertz beam is collimated, straight and aligned with the terahertz camera, it is necessary to understand the optimal distance between source and camera. This is coupled with investigating the accuracy of these terahertz imaging devices for measuring material's properties. Beer-Lambert law relates light attenuation to material properties according to Equation 3.1:

$$I/I_0 = exp^{-\alpha d}$$

where I_o and I are the reference (free space beam path) and sample (measured material in the beam path) light intensities, respectively, d is sample thickness. The distance between the imaging devices is varied from 200 to 600 mm with 10 mm increments. A rectangular slab of acrylic, which has a known absorption coefficient (α) at 100 GHz of 0.5 cm^{-1} [259], is then placed in the beam path. The optimal distance was found in the range between 380-400 mm, where the measurement relative terahertz intensity (I/I_0) was the closest to the theoretical value.

3.3.4. Liquid cell

A custom-made liquid cell, which can confine water to a predefined thickness, is used to assess the system's ability to quantify liquid water. The cell is made from 8 mm thick and 50x50 mm^2 area stainless steel compression plates with rectangular cut-outs with 15x10 mm^2 area. They are fitted with terahertz transparent 4 mm thick and 45x45 mm^2 area acrylic [260] windows and spacers of thicknesses between 6 to 500 µm (Specac, UK; Davis Industrial Plastics, UK). The liquid water is delivered to the inside of the cell with the help of a syringe through an inlet with a one-way membrane tightly fitted into a machined cavity in the compression plate. The water fills the volume delimited by the spacer and comes out through an outlet tube on the other side of the compression plate. This allows the liquid water with the desired thickness to stand in the terahertz beam path. An exploded view of the liquid cell's components is shown in Figure 3.4.

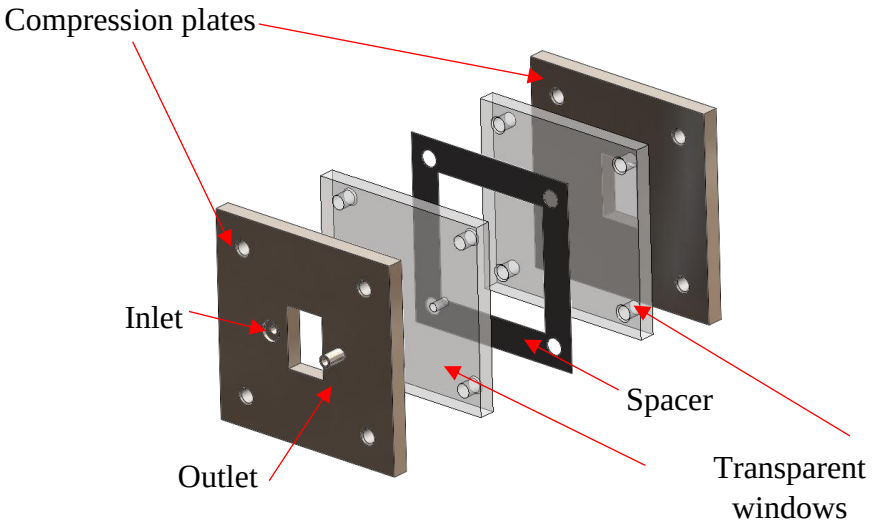

Figure 3.4 - Schematic of the liquid cell's components in exploded view.

3.3.5. Simultaneous gravimetric setup

Upon acquiring the knowledge that this terahertz imaging system could quantify water thickness, the next step was to study the water presence in Nafion membranes. Table 3.2 lists the Nafion membranes of varying complexity and thickness used in these studies:

Table 3.2 – Summary of the Nafion membranes used in the study

Commercial name	Manufacturing process	Thickness (µm)	Supplier
NRE-212	Dispersion cast	50	Alfa Aesar (Lancashire, UK)
N-115	Extruded film	127	Fuel Cell Store (TX, USA)
N-117	Extruded film	180	Alfa Aesar (Lancashire, UK)
N-1110	Extruded film	254	Fuel Cell Store (TX, USA)

The membranes were measured as received, without further treatment. The dry membranes were cut into square patches (~70x70 mm^2) and their weight and terahertz intensity images were acquired after drying for 1 hour in a laboratory oven (Carbolite ELF 11/14) at 105°C. The dry membranes were then equilibrated with deionised water at 80 °C in order to enhance water

uptake [261], as seen in Figure 3.5, after which excess surface water was removed with paper wipes [262].

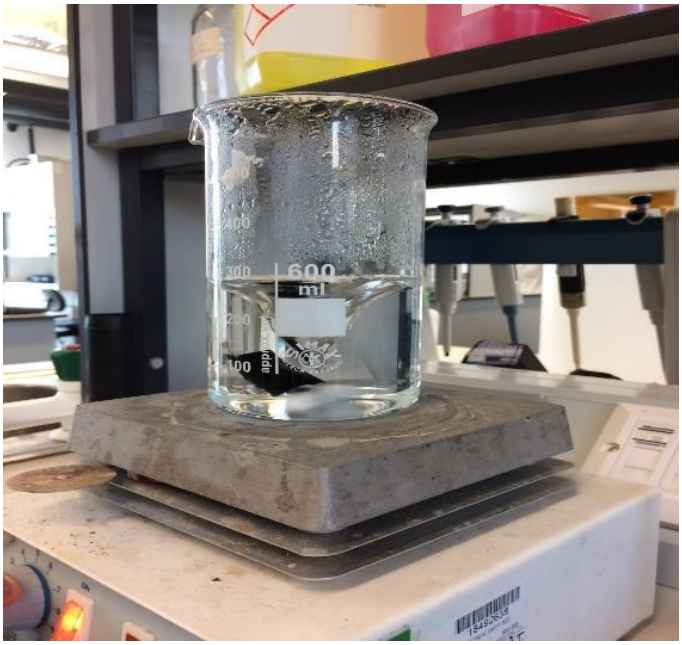

Figure 3.5 – Membrane equilibration with distilled water at 80°C inside a borosilicate beaker.

To understand the scope of the terahertz technique for water quantification in Nafion membranes, the experimental setup went through a series of developments which will be chronologically described in this Section. The goal was to benchmark terahertz estimated water weight against gravimetric measurements. The weight balance used (Kern PCB 350-3) had mg resolution and was connected to a PC for automatic data acquisition at 4 Hz rate. Initially, these techniques were performed separately: a hydrated sample was attached to an acrylic sample holder with binder clips and positioned in the terahertz beam path. Figures 3.6a-b shows a cross sectional diagram and photograph of the sample holder with mounted samples. Afterwards, the samples were rehydrated, and their weight monitored with the balance with a 1-minute sampling time. For this preliminary measurement, Nafion NRE-212 was selected due to its simplicity and lack of reinforcements or additives.

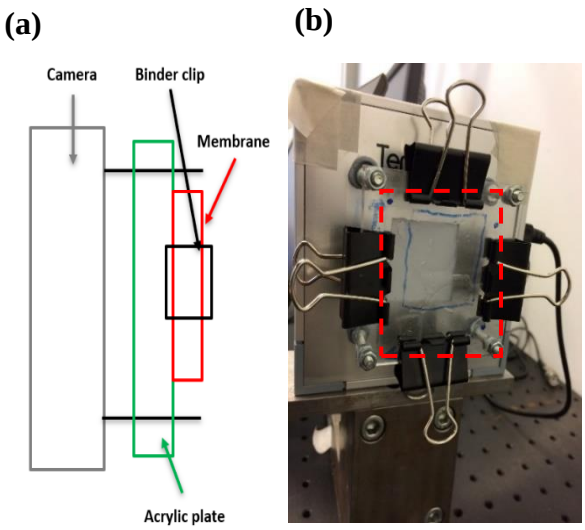

Figure 3.6 – (a) Cross sectional diagram and (b) photograph of the tested Nafion NRE-212 mounted on the sample holder. The highlighted area refers to the membrane location.

Following this, it was decided to perform the measurements simultaneously, both to achieve a closer association of the distinct sets of results and improve the credibility of the study. Figure 3.7a displays the first setup developed for simultaneous experiments. The sample holder consists of an acrylic plate attached to a nylon threaded rod, which is hanging from a hollow aluminium bar. To increase the air/membrane interface and prevent accumulation of droplets on its surface, the acrylic plate featured a cut-out, as shown in Figure 3.7b. The assembly is placed on the balance, stabilised by a 100 mg counterweight. The samples are then hydrated and attached with binder clips. Nafion NRE-212 was also selected for the reasons stated above.

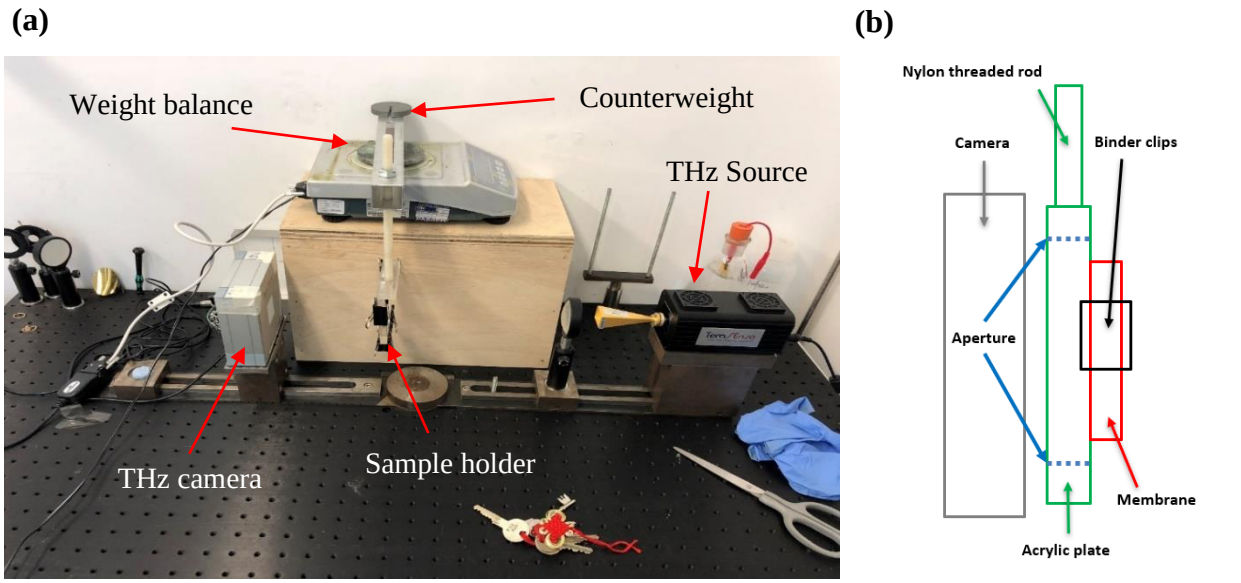

Figure 3.7 – (a) Photograph of the first setup developed for simultaneous terahertz and gravimetric measurements and (b) cross section diagram of the sample holder.

The setup shown in Figure 3.7 was unstable due to the suspended nature of the sample holder. To improve this, a new setup was developed (Figure 3.8a). The structure was simply rearranged by reducing the size of the aluminium hollow bar and nylon threaded rod, allowing it to be positioned firmly on the balance with the aid of the counterweight. In this experiment, the collection of standard Nafion membranes described in Table 3.2 was measured. The hydrated sample was held in place to the sample holder with binder clips (Figure 3.8b) to dehydrate at room temperature.

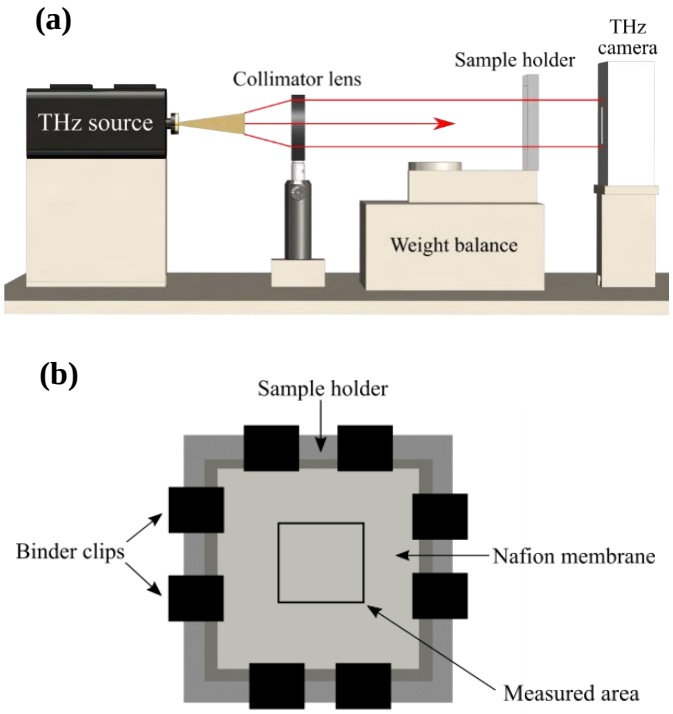

Figure 3.8 - (a) Schematic of the terahertz imaging system for simultaneous gravimetric analysis (b) Front view of the sample holder featuring Nafion sample, binder clips, and area used for terahertz measurements.

3.3.6. Data processing

Hydration imaging in Nafion PEMs

The typical output of the terahertz camera is a video, captured at 30 Hz frame rate. The terahertz intensity images were extracted from the video and analysed using Matlab (Mathworks, Inc., MA, USA), using an in-house developed code for frame extraction and conversion from double-precision RGB to single-precision grayscale images. The developed Matlab code is available on Appendix A.1.

The extracted frames are represented in false colours, with individual pixels representing light

intensities between values of 0 (total absence of light, black) and 1 (total presence of light, white). As mentioned previously, Beer-Lambert Law relates light attenuation to material properties according to Eq. (3.5):

$$I/_{I_o} = exp^{-\alpha d} \tag{3.5}$$

where I_o and I are the reference and sample light intensities, respectively, d is sample thickness and α is the material absorption coefficient (mm^{-1}) – taking on a value of 11 mm^{-1} as the average between 9-13 mm^{-1} at 25°C at 100 GHz [24], [263]–[266] for liquid water, and used for calculation purposes in this Dissertation. Using Beer-Lambert law, water thickness in the area corresponding to a single pixel (d_{pixel}) can be estimated. The measured intensity from the dried membrane is used as the reference measurement to remove the effect of the Nafion membrane, thus isolating the response of absorbed liquid water. The estimated water thickness in each pixel (d_{pixel}), can be used to estimate water weight in each pixel, EW_{pixel}:

$$EW_{pixel} = A_{pixel} d_{pixel} \rho \tag{3.6}$$

where A_{pixel} and ρ correspond to pixel area and water density of at 1 g/cm^3 at 25°C, respectively. Equation (3.7) gives the estimated water weight (EW) in the entire membrane area:

$$EW = \frac{A_{membrane}}{A_{camera}} \sum_{pixel=1}^{196} EW_{pixel} \tag{3.7}$$

To avoid edge effects of the membrane and beam interference from the binder clips used to clamp the sample, a 24x24 mm^2 (size of the FPA camera) middle portion of the sample (A_{camera}), shown in Figure 3.8b, whose edges are 18 mm away from the binder clips is imaged. The selected area corresponds to the terahertz camera's size. The outermost rows and columns of pixels were discarded for liquid water weight estimation across the Nafion membranes due to random fluctuations observed in free space measurements. Therefore, only the 14x14 remaining pixel matrix (196 pixels) was selected in the Matlab code. However, these discarded pixels are shown in in Chapter 4 figures to provide visual evidence of the camera's fluctuating edge effects but were not used in the respective analysis. In addition, the first term on Equation (3.7) extrapolates these results to the entire membrane area ($A_{membrane}$), assuming uniform water content distribution across a vertically mounted sample.

The gravimetric water weight (W_{H2O}) is calculated using Eq. (3.8):

$$W_{H_2O} = W(t) - W_{dry} \tag{3.8}$$

where $W(t)$ is the sample weight at a given time t and W_{dry} is the dry sample weight.

Observations of liquid water accumulation in a PEMFC

Similar to the hydration imaging data processing, the raw data output comes as a video and video frame extraction and post-processing were performed using Matlab. The developed Matlab code is available in Appendix A.2. Imaging data was acquired over the entire operational cycle of the fuel cell (300 min) with 1 min sampling time, resulting in three hundred data points. On each extracted video frame, the data is represented in false colours where individual pixel values range from 0 to 1, proportionally to the amount of terahertz light detected. Image resolution has been improved via bilinear interpolated shading (Gouraud shading) using an inbuilt Matlab function. It minimises the pixelated appearance shown in Figure 3.3, resulting in a smoother appearance that is easier to relate to optical images. In order to avoid edge effects from the PEMFC structure and imaging noise caused by random fluctuations in pixel values [267], the outermost rows and columns of pixels of the raw image data were excluded. Thus, data analysis was focused on the resulting 14x14 pixel matrix. Figure 3.9 shows examples of pre-analysis terahertz images of the PEMFC transparent cut-out. Figure 3.9a refers to the initial frame (0 min) where the cut-out is dry without current density applied, while Figure 3.9b shows a flooded state. The central region with visibly high intensity of terahertz transmission (black) in Figure 3.9a corresponds to the transparent cut-out. The data analysis was focused on the lower half of the region (white) where the majority water accumulation was expected. This accumulation can be observed by dimmer pixels in Figure 3.9b. The low intensity values at the bottom row are due to the edge of the cut-out.

Terahertz images are processed as difference images, using the Figure 3.9a as a reference to subtract away the background. The mean change in terahertz intensities, $I(t)$, across the area at a given time t is calculated as:

$$I(t) = \left. \sum_{pixel=1}^{N} (I_0 - I_{pixel}) \right/ N \tag{3.9}$$

where N is the total number of pixels, I_{pixel} and I_0 are the sample and reference light intensities in each pixel. For the sake of clarity, it is important to note that as a direct result of Equation (3.9), water presence in terahertz difference images is characterized by high terahertz intensity, in contrast to Figure 3.9b. To illustrate this, Figures 3.9c-d shows post-processed Figure 3.9a-b images. As expected, Figure 3.9c's pixel values equal zero while Figure 3.9d underlines the

water response. High intensity pixels under the highlighted area in Figure 3.9d are related to edge effects at the edge of the cut-out.

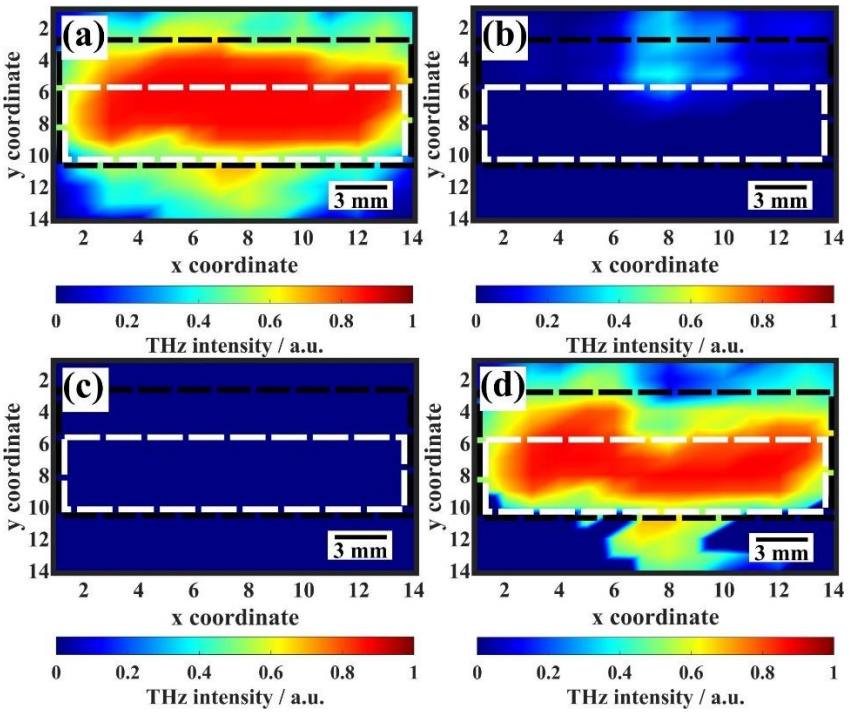

Figure 3.9 – Pre- and post-processed terahertz false colour images of the (a), (c) dry and (b), (d) flooded PEMFC transparent cut-out. Highlighted regions represent the overall cut-out and analysed area, respectively.

3.4. High-resolution optical imaging

3.4.1. Materials

The optical imaging system is based on an IMT-CAM-028 high-resolution optical camera incorporating an IM-LENS-MT051 material testing lens (Imetrum, UK). To ensure adequate illumination in the optical images, the experimental setup was illuminated constantly using an external LED floodlight. These devices are connected to a desktop PC for data acquisition. The IMETRUM proprietary software allows for control of the optical devices and data capture.

3.4.2. Data processing

The standard output from the optical camera is a video, captured at 0.2 Hz frame rate. The video frame extraction and post-processing were performed using Matlab. Data was collected over 300 min of operation, at a 5 s sampling time resulting in 3,600 data points. Image

segmentation was used, which took approximately 0.5 s per frame. To improve the processing speed, frame rate of the video was down sampled by a factor of four, resulting in approximately 900 frames analysed in approximately 7.5 min. The analysis had two distinct goals: identify and track deformation of the exposed PEM (due to swelling) and the upper boundary of the accumulating water pool. These are related to PEM hydration and PEMFC cathode flooding, respectively. These are achieved by firstly identifying an appropriate point in the video where the swelling deformation first becomes visible and localizing the initial deformation point using intensity-based thresholding. This gave an initial reference point, which is tracked throughout the following frames using a pre-determined stopping point, when the deformation is no longer observable. This resulted in a 3D point cloud, which is converted into a probability map to reconstruct the deformation region. The area of the deformation is calculated as number of pixels. The second task is more challenging that requires repetitions due to the varying nature of the apparent contour on the upper boundary of the water pool. This is caused by the occurrence of distinct water transport processes, such as droplet condensation and movement across the visible window, which may overlay the water pool region and hinder boundary tracking. Here, a graph search approach is utilized that seeks to find the strongest vertical change in intensity while minimizing the length of the boundary contour. The initial frame corresponding to the main droplet appearance is identified and a seed point is placed. For clarity, this refers to the water droplet that will eventually grow into a substantial water pool, rather than condensation on the transparent window. From this point, the boundary is traced using the model and the seed point for the next frame is determined automatically. In cases where the segmentation is deemed to have failed due to artefacts, these segmentations are removed, and subsequent frames reinitialized. Finally, the full video segmentation is realized by combining the results from each frame, using bicubic interpolation for any removed frames. The upper boundary of the water pool is then quantified as the relative change in the mean horizontal position of the boundary to mitigate the impact of noise. The area recognized as liquid water is calculated as the number of pixels below the boundary but lying within the annotated frame. For clearer representation, both areas (PEM swelling, cathode water pooling) were normalized against the overall number of analysed pixels (~ 980,000 pixels). Thus, the optical area in subsequent comparison figures is represented as a percentage of pixels considered to be water presence in the analysis region.

3.5. Summary

In this Chapter, the complete details on experimental methodology for the studies performed in this PhD project are presented. The terahertz imaging system on its own and coupled with simultaneous gravimetric measurements and ensuing data processing algorithms were realised for hydration imaging in PEMs and flooding observations in PEMFCs. For the latter topic, a high-resolution optical imaging and data processing algorithm was also developed. Finally, a terahertz transparent PEMFC capable of normal operation and electrochemical production of water and its accompanying gas delivery system were accomplished.

4. Hydration imaging in Nafion PEMs

Nafion membranes are considered the industry standard electrolyte material for proton exchange membrane fuel cells. These membranes require adequate hydration to reach high proton conductivity. The high sensitivity of terahertz radiation to liquid water enables contrast to be observed for inspecting water presence in Nafion electrolyte membranes.

This Chapter evaluates the feasibility of a simple, compact terahertz imaging system for visualising and quantifying liquid water during an ambient air desorption process for Nafion membranes of a wide range of thicknesses and characteristics, as a first step towards water visualisation in a fully operating PEMFC.

4.1. Introduction

The most common material for PEM is a perfluorinated ionomer copolymer known as Nafion, consists perfluorovinyl ether groups terminated with sulfonate groups incorporated onto a PTFE backbone [268]. Liquid water uptake is known to enhance proton conduction in Nafion membranes [12], [58], [59]. In addition, homogenous hydration aids in maintaining uniform membrane impedance, where protonic current is similar across all the PEM area. Failure to achieve this will result in protonic current gradients, localised hotspots (as internal resistance increases) and pinhole formation, possibly resulting in PEMFC failure [269]. Achieving uniform PEM hydration during operation is challenging, as regions of the membrane near the gas inlets tend to be dehydrated due to an increased gas pressure but become increasingly humid because of downstream water transport with the reactant gas. Thus, water management is a crucial part of PEMFC operation: Nafion PEM requires hydration to operate and hence reactant inlet streams are humidified [26], but at the same time, water is a by-product of the electrochemical half-reaction at the cathode and therefore must be swiftly removed to prevent cell flooding and reactant starvation at active electrocatalyst sites [27].

In the context of off-line water sorption and desorption dynamics in Nafion membranes, techniques such as dynamic vapour sorption, differential scanning calorimetry, electrochemical impedance spectroscopy and confocal micro-Raman spectroscopy have been used [270]–[284]. Additionally, the different modes of water (free, bound, etc.) inside Nafion membranes can also be probed using broadband dielectric spectroscopy [285], [286] . Although these are sensitive measurements for sensing water content in Nafion membranes, with µm resolution in the case of Raman spectroscopy, they cannot spatially resolve liquid water distribution over large areas at video-rate. Additionally, they may require detailed sample preparation, calibration models, or specialised equipment with temperature and humidity control.

Measurements using terahertz radiation in fuel cell-related studies have demonstrated the sensitivity to many different phenomena, including visualisation of liquid water in flow channels [250], [251] and hydration monitoring in PEMs [248]. However, these studies are performed with single-point THz-TDS and thus unsuitable to image an entire section of a PEM. Raster scanning can be a solution to image water spatial distribution, but it can assume to several minutes pending on integration time and scanned area size. Therefore, it will not be able to portray an accurate real-time spatial distribution of water in a Nafion membrane exposed to ambient air.

In this chapter, the feasibility of a terahertz transmission imaging system based on a terahertz FPA camera and a 0.1 THz IMPATT terahertz source for direct water visualisation and quantification in Nafion PEMs, as an initial route towards liquid water inspection in fully operating PEMFC is investigated. First, the development of the experimental procedure will be explained, followed by presentation of results obtained and accompanying discussion, and ending with a summary. In particular, the terahertz system's sensitivity for water quantification is validated against known water thickness, and then water weight in a wide selection of Nafion membranes is estimated across time, benchmarked against gravimetric analysis. Finally, to assess the system's ability to spatially resolve water distribution across a Nafion membrane, the desorption profile of a partially hydrated Nafion membrane at room temperature was imaged under ambient conditions.

4.2. Results and discussion

4.2.1. Terahertz liquid water quantification

To assess the ability of the proposed terahertz imaging system to estimate liquid water thickness in the membrane, terahertz intensity images of the 'dry' and 'hydrated' liquid cell for a range of spacer thicknesses were acquired and compared. Figure 4.1 shows the intensity images for the 50 µm spacer where there is a clear difference between the two images in the highlighted region of interest, corresponding to the liquid cell's aperture. As expected in the presence of liquid water, intensity of terahertz transmission is notably reduced due to water absorption thus leading to lower detected values resulting in visibly 'dimmer' values on the image in Fig. 4.1b. For quantification purposes, pixel values in the 3x4 pixels region of interest at the centre of the high transmission zone in dry (Fig. 4.1a) and hydrated states (Fig. 4.1b) are selected and compared.

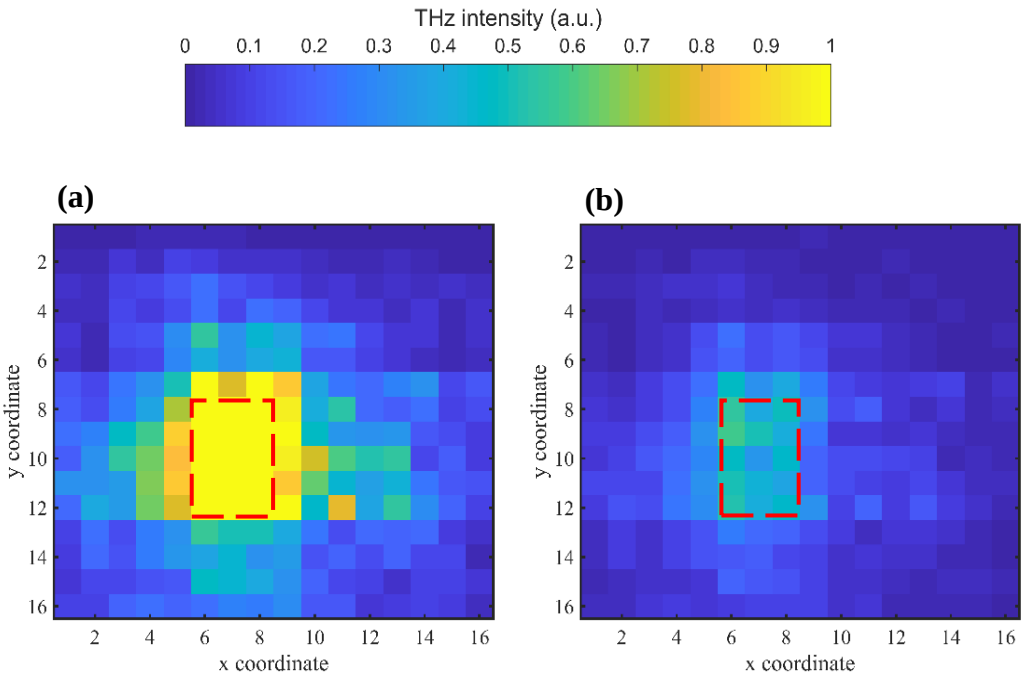

Figure 4.1 – Terahertz false colour images of the (a)'dry' and (b) 'hydrated' liquid cell of spacer thickness 50 µm. Highlighted region corresponds to the aperture in the liquid cell and is used for quantification purposes.

The relative transmitted intensity in each pixel (I) in the region of interest is given by Equation (4.1):

$$I = {I_{hydrated}}/{I_{dry}} \tag{4.1}$$

for different water thicknesses of 6, 12, 25, 50, 100, 200, 250 and 500 µm, as shown in Figure 4.2. This is plotted against the expected values from the Beer-Lambert law with variations in absorption coefficient. For the sake of clarity, the experimental relative transmitted intensity is calculated on a pixel-by-pixel basis, rather than pixel value averaging across the region of interest. The mean and standard deviation of the relative intensity of the region of interest pixels are then displayed as error bars in Figure 4.2. In addition, for each of the measured thicknesses, five repeats were taken.

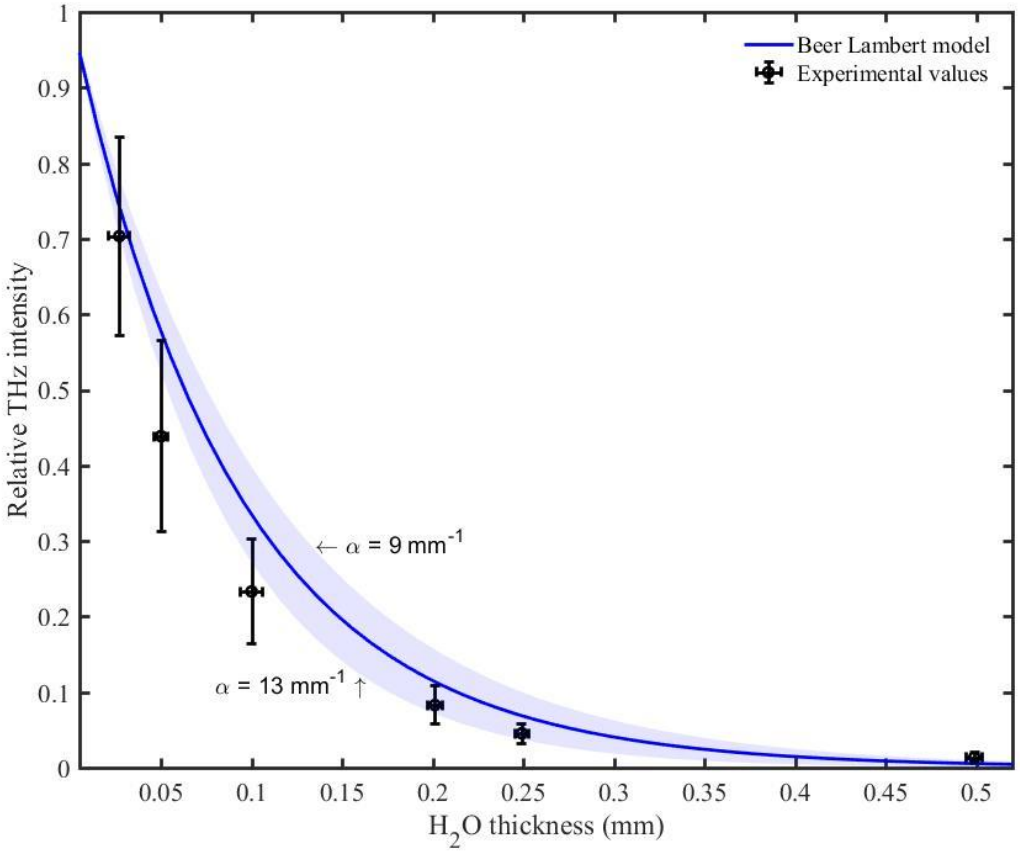

Figure 4.2–- Water quantitative analysis showing the measured relative transmitted terahertz intensities at a 25-500 µm range of liquid water thicknesses, against the expected values using Beer Lambert Law with absorption coefficients of 9-13 mm^{-1} at 100 GHz at 25°C, with maximum (13 mm^{-1}) and minimum (9 mm^{-1}) values displayed at the boundaries of shaded area. The vertical error bars refer to standard deviation between five experiments. The horizontal error bars refer to thickness tolerances of the spacer material.

It should be noted that, there were no discernible differences in pixel values between 'dry' and 'hydrated' terahertz intensity images for 6 and 12 µm spacer thicknesses due to the limited terahertz camera detection sensitivity, and thus these values are not shown in Figure 4.2. However, for increasing water thicknesses, there is an agreement against the expected values where terahertz transmission decays exponentially with increasing water. It is important to highlight that for 25 and 50 µm water thicknesses, there is a higher standard deviation between measurements when compared against 200 and 250 µm. This can be due to decreasing systems detection sensitivity with decreasing water content. In addition, although 500 µm water thickness presents low standard deviation (< 0.01 relative THz intensity), a water layer 500 µm-thick should theoretically attenuate over 99.5% of the incident terahertz beam and thus measurements in this region will have considerable uncertainty. Nevertheless, the data shows the system can quantify liquid water content, in the 25-500 µm detection range of water thicknesses, with a 25 µm limit of detection and 25 µm minimum sensitivity, given by the

smallest difference between calibration points (25 and 50 µm). Considering Schmidt-Rohr and Chen [287], it can be assumed that overall water thickness in the Nafion structure is comparable to the thickness of the membrane itself, and thus suggesting that liquid water quantification in Nafion membranes is possible.

4.2.2. Liquid water weight estimation in Nafion PEM

Following on water thickness estimation in a liquid cell, the thickness range estimated from relative intensity measurements is applied to estimate the mass change, during a water desorption test in ambient air, for distinct types of Nafion membranes benchmarked against gravimetric analysis. This in turn allows to show the ability of a simple terahertz imaging system to quantify water across Nafion membranes.

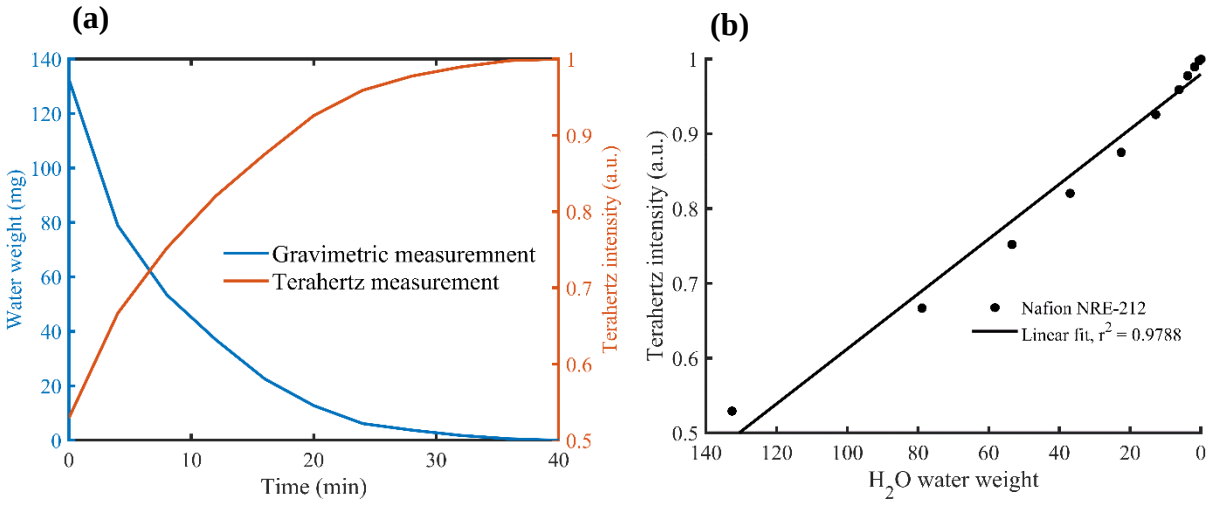

Figure 4.3 – Preliminary data on the evolution of (a) terahertz intensity and water weight during a water desorption process of a Nafion NRE-212 membrane, measured by non-simultaneous terahertz and gravimetric measurements. (b) Degree of correlation between the independent tests.

Preliminary experiments were performed using a non-simultaneous terahertz and gravimetric arrangement, to investigate the ability of the terahertz imaging system to estimate water thickness initially on a Nafion NRE-212 membrane. Figure 4.3a shows the terahertz intensity and water weight data obtained for a single measurement during the water desorption process. The curves present an exponential behaviour (growth in terahertz and decay in gravimetric), similar to observed in other water desorption studies in Nafion membranes [275], [276], [282], [283]. A correlation between the independent curves is studied through a linear fit, presented in Figure 4.3. Nafion NRE-212 exhibits a linear relationship between the two sets of data, with a coefficient of determination (r^2) 0f 0.9788 in the linear fit. These preliminary results are

important clues regarding the system's ability to quantify liquid water and its relationship to established gravimetric measurements.

Following these preliminary results, the next step was simultaneous terahertz and gravimetric measurements, acquired continuously over a specific period. This method is time efficient, robust and can provide a better agreement between the studied parameters. The membrane used to assess this new arrangement was Nafion NRE-212, due to its standard material status and reliable results obtained previously. Measured and estimated weights correspond to the weight change of water determined by simultaneous gravimetric analysis and terahertz intensity images, respectively. Four repeats were performed for this study. Figure 4.4 shows that the curves agree well in terms of water uptake and desorption slope. The curves also present an exponential decay consistent with previous studies on Nafion water desorption. An important detail is the high standard deviation between repeats in the gravimetric measurements, when compared to the terahertz measurements. The terahertz setup benefits from better physical stability due to all the components being rigidly fixed, while the suspended sample holder is a source of significant measurement noise. This introduces a large amount of uncertainty in the results, since it can be difficult to locate the timeframe when the gravimetric readings plateau and distinguish physical phenomena from measurement noise. In sum, the simultaneous setup showed a general correlation between the two distinct techniques. However, high standard deviation from distinct measurements means that improvements on the sample holder structure were still required.

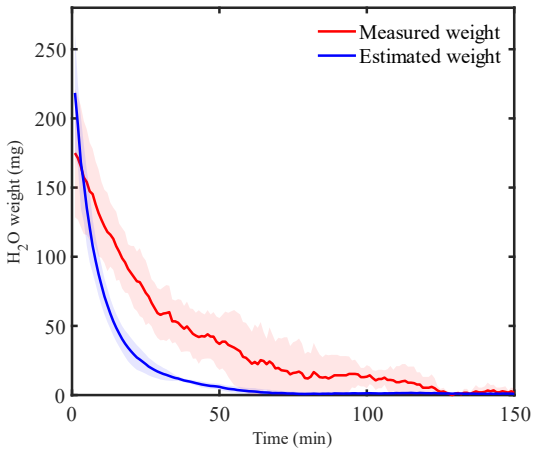

Figure 4.4 - Water desorption from saturated Nafion NRE-212. Blue and red line and shade represent the mean and standard deviation of estimated liquid water weight from terahertz intensities and actual measured liquid water weight from gravimetric analysis, respectively, from four repeated experiments.

Finally, a definitive experimental procedure was established. In this case, four types of Nafion with a wide array of thicknesses were investigated: Nafion NRE-212 (50 µm), N-115 (127 µm),

N-117 (180 µm) and N-1110 (254 µm). It should be noted that four repeats were performed for each of the membranes.

Fig. 4.5 shows a good agreement between the measurement and estimation curves, which shows an exponential decay behaviour, like Figure 4.4. However, there are notable differences between the curves, which can be consistently observed across the membranes. Firstly, the terahertz estimated weight overshoots the measured weight values. This can be attributed to the presence of residual liquid surface water that may be present in thicknesses outside the thickness range (25 – 500 µm) and the non-uniform water distribution across the membrane especially for a vertical sample mounting arrangement thus leading to higher estimated weight values. Secondly, differences are observed between the time constants. It can be noted that after the initial minutes, the curves overlap with discrepancies appearing close to the end of measurement. This effect is shown in Figure 4.5a, from around 15-20 minutes until the 40-minute mark. The divergence in time constants between the curves is due to significant surface water accumulation under the binder clips, outside of the measurement area of the terahertz camera. Water loss in Nafion is usually attributed to diffusion from the interior of the membrane to the membrane/gas interface and subsequent transport into the gas phase, the latter being considered the key mechanism to this desorption process [282]. The region under the binder clips used as part of the experimental setup also has limited membrane/gas interface, so water loss happens at a slower rate because it is governed by an internal diffusion process only. Furthermore, the terahertz imaging system measures liquid water in the Nafion structure across a small area corresponding to the terahertz camera aperture while the gravimetric setup is measuring the weight of the entire sample holder structure, and therefore it is likely that this accumulated water is responsible for the increase in time constant of the measured weight curve. A potential future solution would be assembling the terahertz imaging system in a vertical arrangement as this excludes the necessity for binder clips and the effect of gravity.

The NRE-212 membrane clearly presents a higher level of standard deviation across repeats when compared to other membranes. This can be due to the presence of significant surface water in this membrane, which was challenging to remove thoroughly and consistently, as illustrated by the large standard deviation in the terahertz measurement at the beginning of the experiment. The smaller thickness of Nafion NRE-212 at 50 µm also coincides with the system's reduced sensitivity at lower water thickness ranges as opposed to 100, 200 or 250 µm thus explaining why estimated weight values in Figure 4.5a present the highest variation.

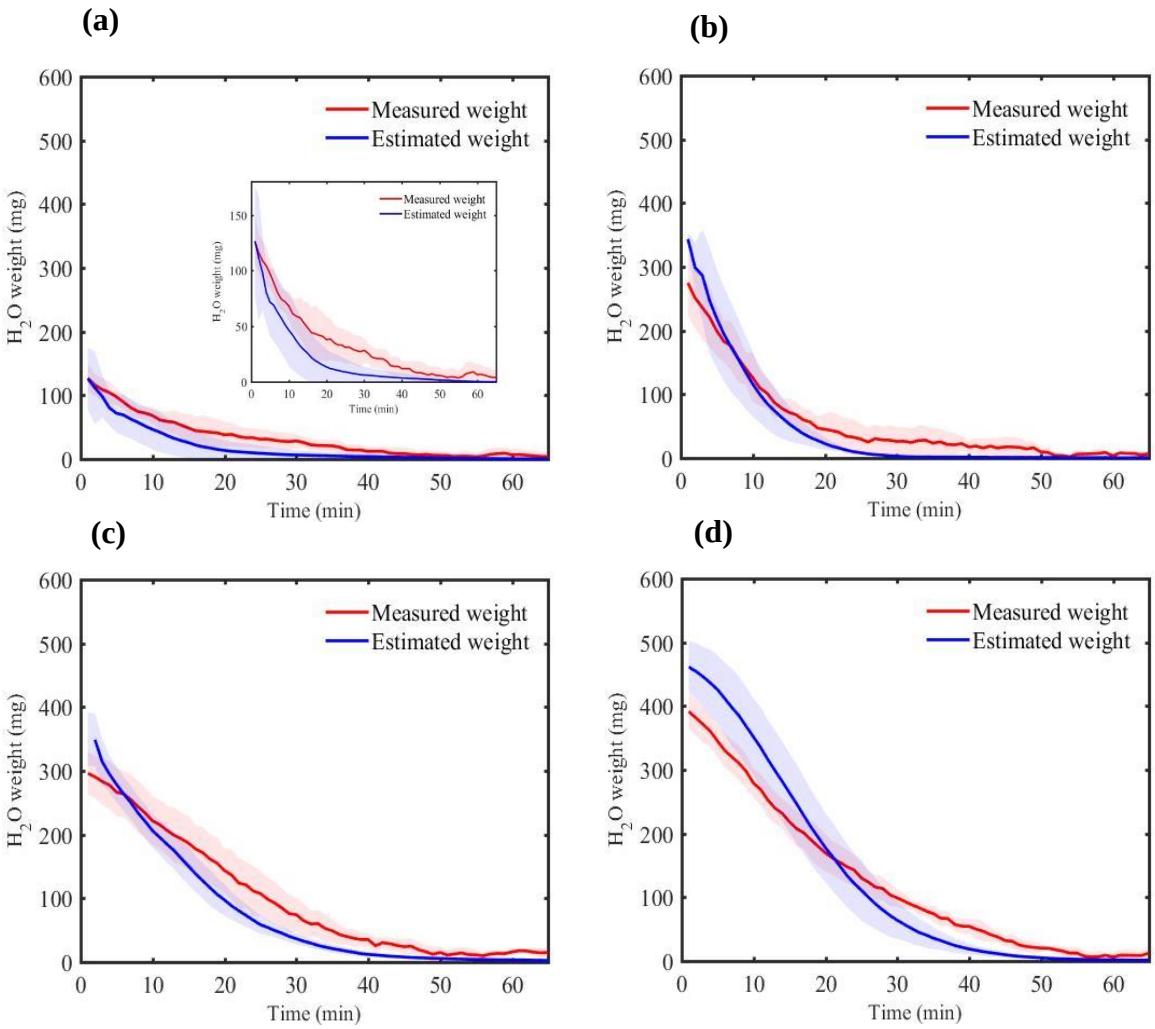

Figure 4.5 - Water desorption from saturated Nafion (a) NRE-212, (b) N-115, (c) N-117 and (d) N-1110. Blue and red line and shade represent the mean and standard deviation of estimated liquid water weight from terahertz intensities and actual measured liquid water weight from gravimetric analysis, respectively, from four repeated experiments. For clarity, a reduced scale inset is present on (a).

By examining the water uptake of the individual membranes, shown by the initial water measured weight values, it also increases as the membrane thickness increases, consistent with Schmidt-Rohr and Chen [287]. However, the increase is not proportional to thickness, for example there is a large difference in water uptake between 50 µm thick NRE-212 and 127 µm thick N-115 (125 and 275 mg, respectively) while the difference in water uptake between the N-115, 180 µm thick N-117 and 254 µm thick N-1110 is smaller (275, 295 and 395 mg). Although dispersion cast (NRE-212) and extruded membranes (N-115, N-117, N-1110) can display small differences in water uptake [288], these results nevertheless suggest that water desorption is not dependent on membrane thickness but rather on the water absorbed to sulfonic acid groups as asserted by Majsztrik et al [282]. This is also evident in water desorption time where NRE-212 and N-115 desorbed within 30 minutes, while N-117 and N-1110 took approximately 50 minutes.

4.2.3. Liquid water imaging on Nafion PEM

To demonstrate the ability to image hydration distribution across the membranes, here the liquid water content of a partially hydrated Nafion N-117 membrane was imaged using the proposed terahertz imaging system throughout the 120 min room temperature desorption process at 30 Hz framerate. Prior to measuring, the N-117 membrane was clamped to the sample holder and deionised water was administered directly to the lower portion of the standing membrane using a plastic squeeze bottle with a nozzle (~1 mm inner diameter). This was performed to ensure that only the lower half of the membrane is hydrated. Excess water on the surface of the hydrated area, binder clips and sample holder were carefully removed using paper wipes. Figure 4.6 shows snapshots of the acquired terahertz images of the Nafion membrane at different timestamps of water desorption process. In order to reduce image noise and improve smoothness for qualitative water visualisation [289], median filter and contrast enhancement, via image thresholding, were applied to the terahertz images.

Figure 4.6a displays two separate regions, ‘dry’ and ‘hydrated’ where the latter is represented by lower terahertz transmitted intensity due to beam attenuation by liquid water. Over time, as the membrane dries, the ‘hydrated’ region shrinks, as expected. Desorption is not uniform across the membrane area, as observed in Figure 4.6c, the left side of the ‘hydrated’ region (x = 1 to 8) has lower terahertz transmission compared to the right side (x = 10 to 16) after 30 minutes of operation. In addition, two areas on the lower side of the image (y = 12 to 16, x = 1 to 6 and x = 13 to 16) retains liquid water even after 120 minutes of operation, as seen in Fig. 3.11e. These zones are related to water accumulation by gravity effect around the binder clips used to clamp the membrane for imaging, during hydration of the lower half of the membrane. By closely examining the acquired images, various effects of noise can be observed. The extent of these effects is analysed in more detail on section 4.2.4. To be specific, the camera provides unreliable readings at corner pixels. Additionally, there are ‘dimmer’ pixels appearing randomly across the ‘dry’ region in Figures 4.6c-e. This is consistent with an independent measurement on a dry membrane where pixel intensities are also reduced around the camera edges in addition to terahertz attenuation by the Nafion membrane [244]. Further inspection of the ‘dimmer’ pixels’ shows that intensities tend to fluctuate around 10-30% of their maximum value during the water desorption process. This is likely to be caused by the through-plane structural change that the membrane experienced: from a swollen, hydrated state (Figure 4.7b) to a flat and dry state (Figure 4.7a) due to water uptake [11]. At the same time, it should also

be noted that this simple setup is also prone to vibrations from various environmental sources and the effect of which, can also propagate into the measurements.

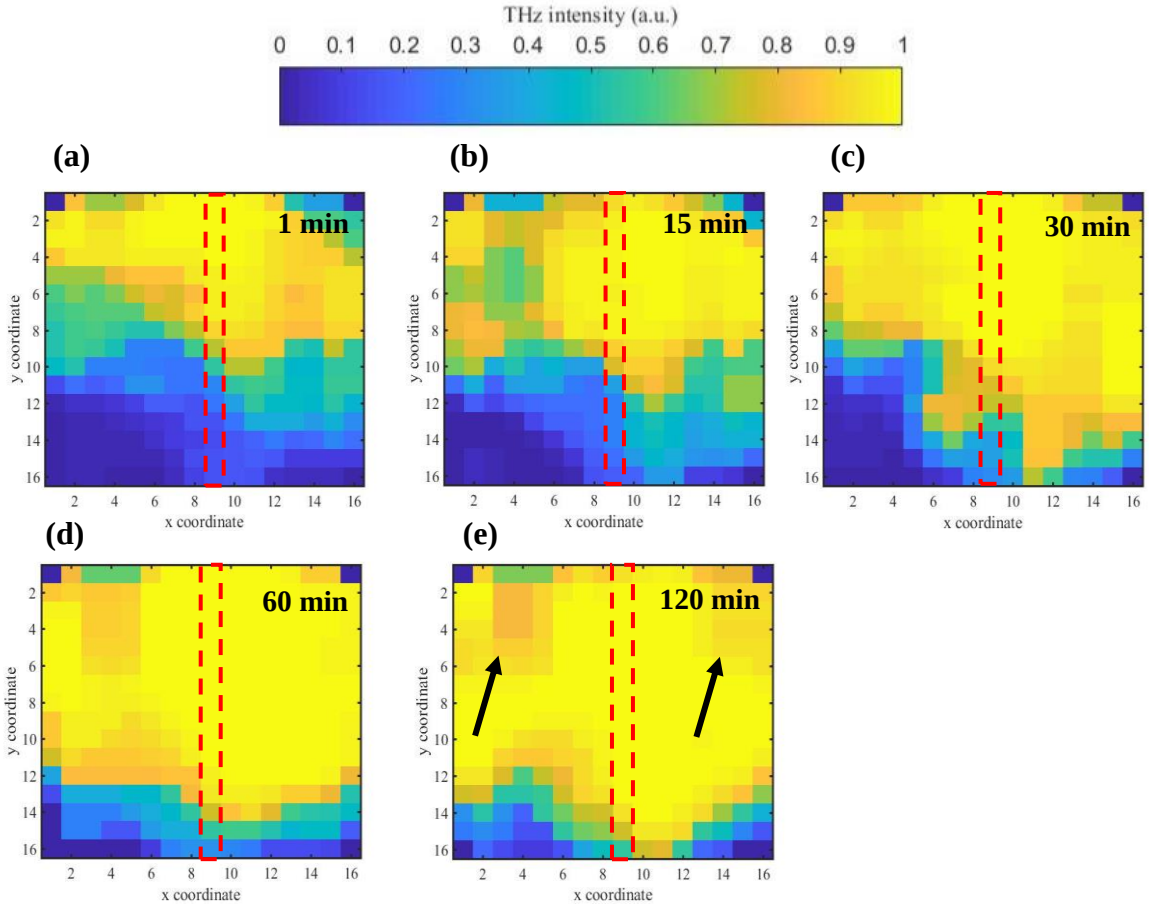

Figure 4.6 - Terahertz false colour images of a partially hydrated Nafion N-117 membrane during desorption process, timestamped at (a) 1min, (b) 15 min, (c) 30 min, (d) 60 min, (e) 120 min. Highlighted regions correspond to the selected pixels for further analysis in Fig. 3.7. Black arrows in (e) indicate 'dimmer' pixels related to the noise of the imaging setup.

To further illustrate spatial differences in water content across the Nafion membrane, Figure 4.8 shows the pixel intensity evolution across time in the highlighted sections in Figure 4.6. At the beginning of the experiment, the 'dry' region in the upper half of the image (y = 1 to 8) has intensity values close to 1 (full transmission), while the 'hydrated' region (y = 11 to 16) has lower intensity values. A transition zone between the regions (y = 9 to 10) bears an intermediate intensity value. Terahertz transmission on the 'hydrated' pixels increases gradually as the membrane approaches a dry state. The majority of 'dry' pixels values progressively plateau near full transmission, indicating that any small amount of water present in this region dries out quickly. An exception to this trend is shown in pixels in the 'dry' region (y = 1 to 4) decreasing in intensity values from 1 to 15 minutes of operation. This is caused by presence of the 'dimmer' pixels, observable in Figure 4.6b.

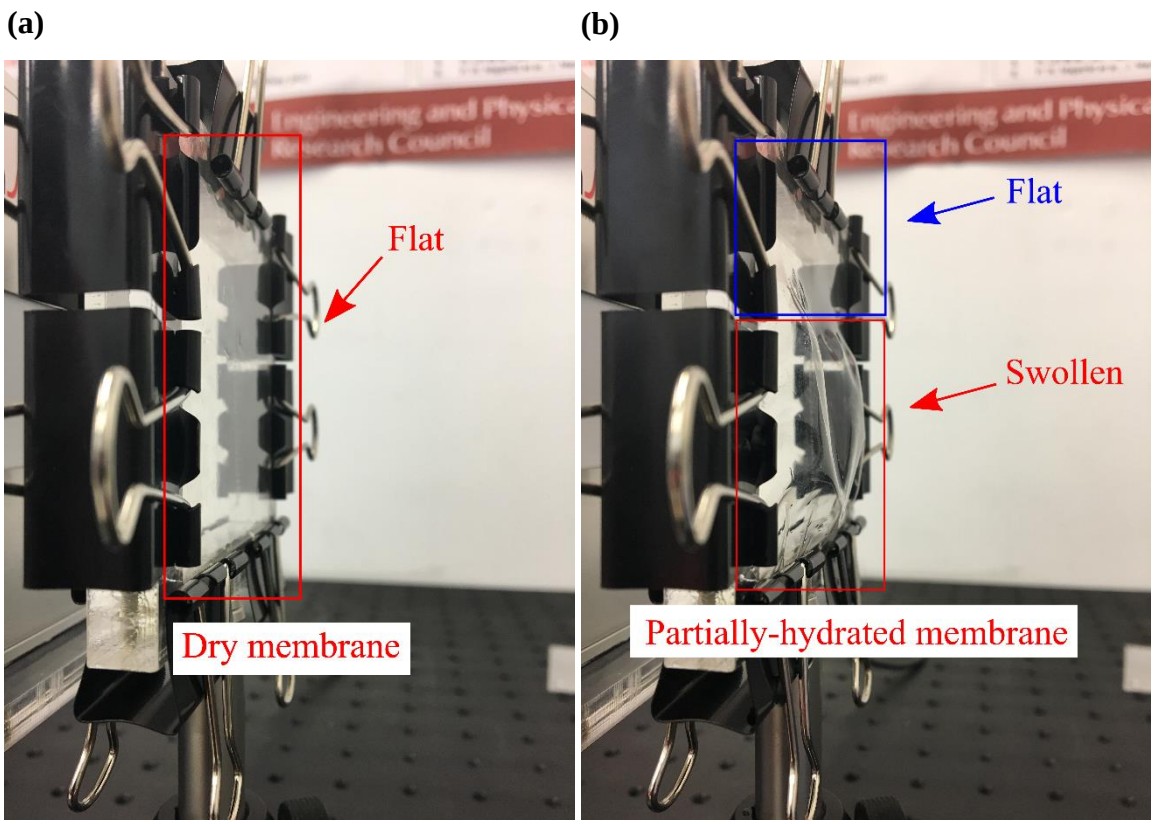

Figure 4.7 - Photographs of a (a) dry and (b) partially hydrated Nafion N-117 membrane.

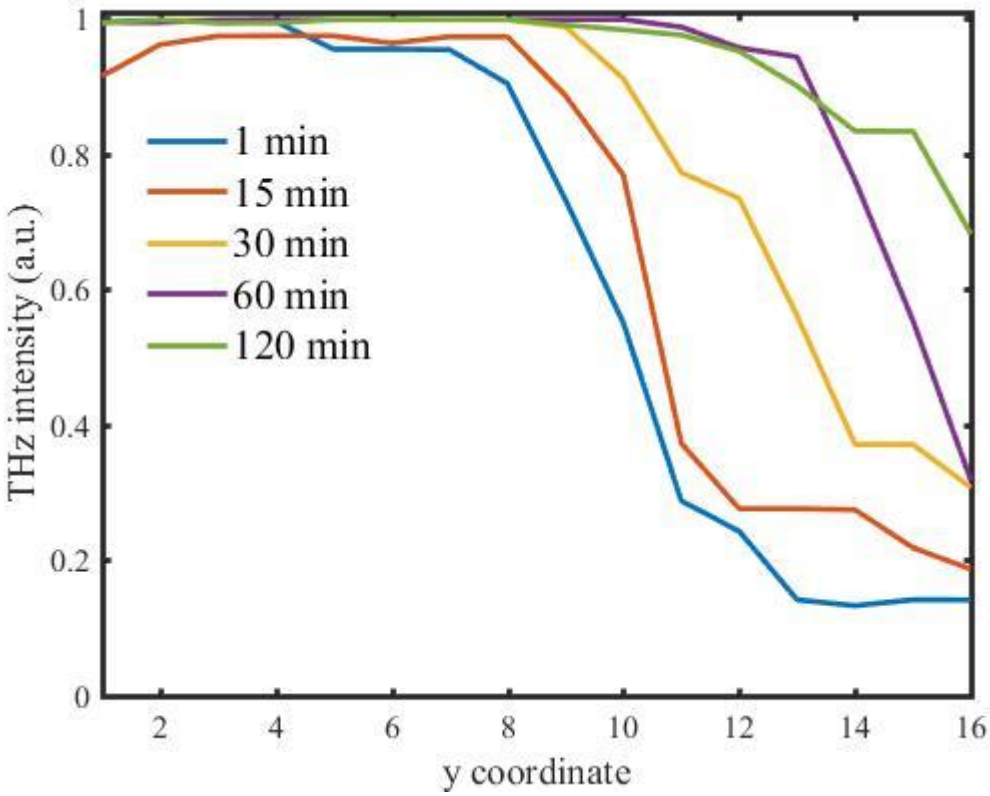

Figure 4.8 - Evolution of terahertz transmission in a specified pixel region along the y axis, highlighted in Figure 4.6.

4.2.4. Imaging noise analysis

During the examination of terahertz imaging of water presence in Nafion membranes, it was understood that the reliability of the proposed terahertz imaging system needed to be investigated. This concern is related to the imaging noise observed on the pixels around the edges of the camera, when analysing free space and the dry side of the membrane seen in Figure 4.6. Thus, the two tests were conducted on free space and on a dry Nafion N-117 membrane.

Free space

The intrinsic noise associated with the terahertz camera and source was analysed by capturing free space between them for 60 minutes. Figure 4.9 shows the terahertz images at the start (4.9a) and at the end (4.9b) of the process.

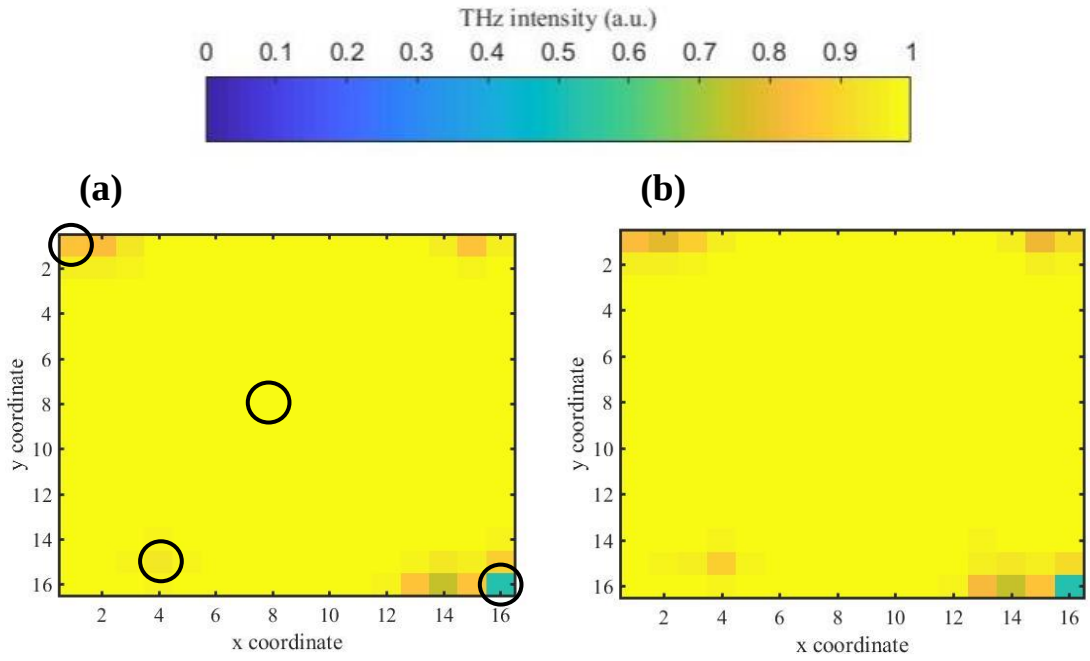

Figure 4.9 - Terahertz false colour images of free space at (a) 1 min and (b) 60 min. Black circles in (a) highlight 'dimmer' pixels selected for analysis.

It can be observed that the images are similar, and the majority of pixels stay at full transmission, except for 'dimmer' pixels located mostly at the corners of the image. Figure 4.10 shows intensity evolution throughout the measurement of 4 pixels to further explain the difference between 'brighter' and 'dimmer' pixels as well as showing differing levels of noise in 'dimmer' pixels. For the sake of clarity, specific pixels will be referred to as Pixel (x coordinate, y coordinate) and each pixel has a 1.5 mm size. The 'brighter' Pixel (8,8) maintains maximum terahertz intensity while 'dimmer' Pixel (16,16), Pixel (1,1) and Pixel (4,15) display

fluctuating values and lower average intensity compared to Pixel (8,8). Given the free space nature of this test and the oscillating pattern of the 'dimmer' pixels, it is unlikely that these pixels are displaying any physical effect, but artifacts related to the terahertz equipment itself.

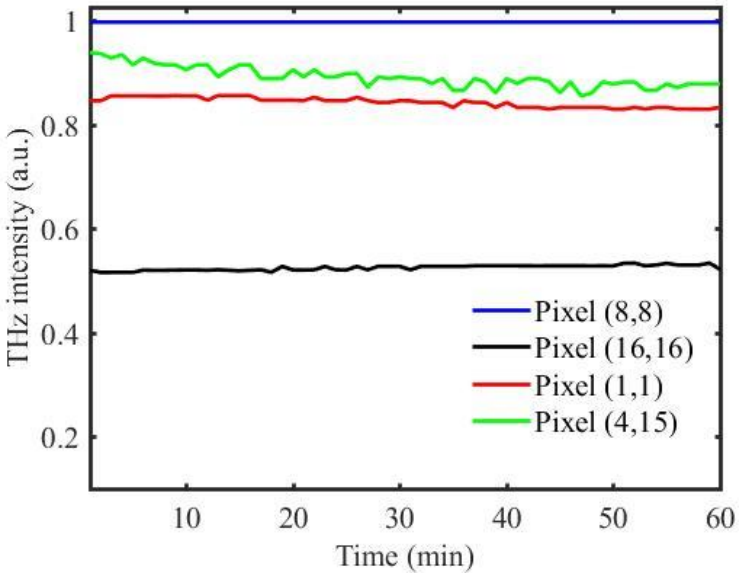

Figure 4.10 - Pixel intensity evolution of 4 selected pixels across 60 minutes. Legend should be read as Pixel (x coordinate, y coordinate).

Dry membrane

Imaging noise was further analysed using a Nafion N-117 membrane as a sample with an imaging time of 60 minutes. Figure 4.11 shows the terahertz images at the start (4.11a) and end (4.11b) of the process.

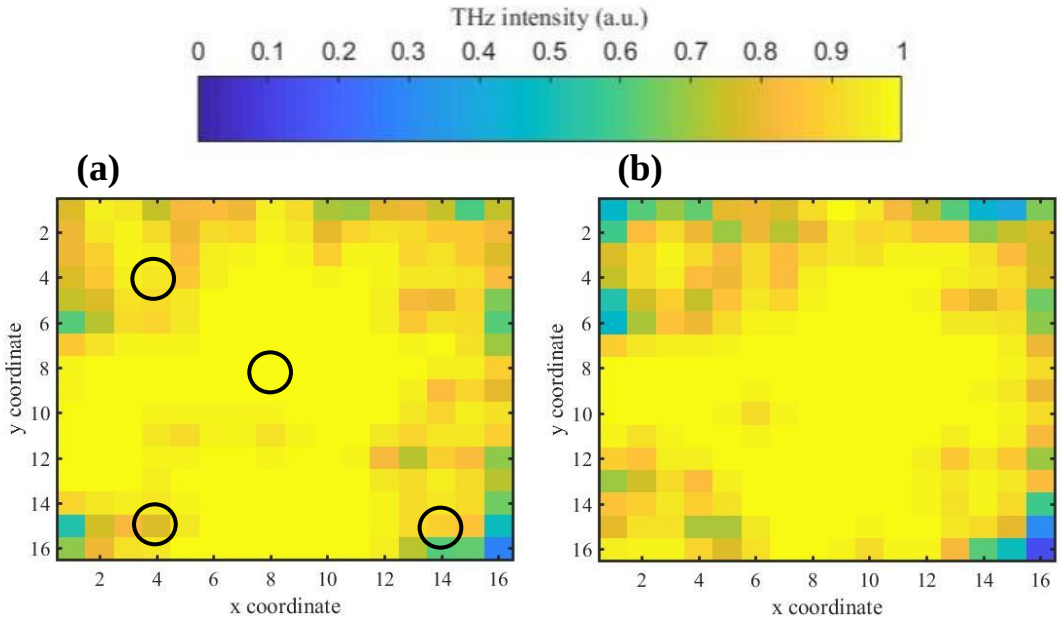

Figure 4.11 - Terahertz false colour images of a Nafion N-117 membrane at (a) 1 min and (b) 60 min. Black circles in (a) highlight 'dimmer' pixels selected for analysis.

The images show that the Nafion structure's interaction with the terahertz beam is manifested as a reduction in pixel intensity mostly around the camera's edges and corners. In addition, even though the sample is static, Figures 4.11a and 4.11b have noticeable discrepancies in pixel intensity distribution, resulting in different average pixel intensity (0.92 and 0.90, respectively). Figure 4.12 displays the intensity evolution of 4 selected pixels across time, with pixel (8,8) located at the centre of the image, Pixel (14,15) and Pixel (4,15) located near the edge of the image and pixel (4,4) in a noticeable 'dimmer' zone in the upper right-hand side. Identical to the free space analysis, Pixel (8,8) maintains maximum transmission throughout the measurement. However, the rest of the pixels present an oscillating pattern, fluctuating up to 20% of their maximum value. Since the membrane is clamped down to the sample holder with binder clips and thus significant movement is unlikely, it is hypothesised that this behaviour is related to imaging setup vibrations from miscellaneous environmental sources.

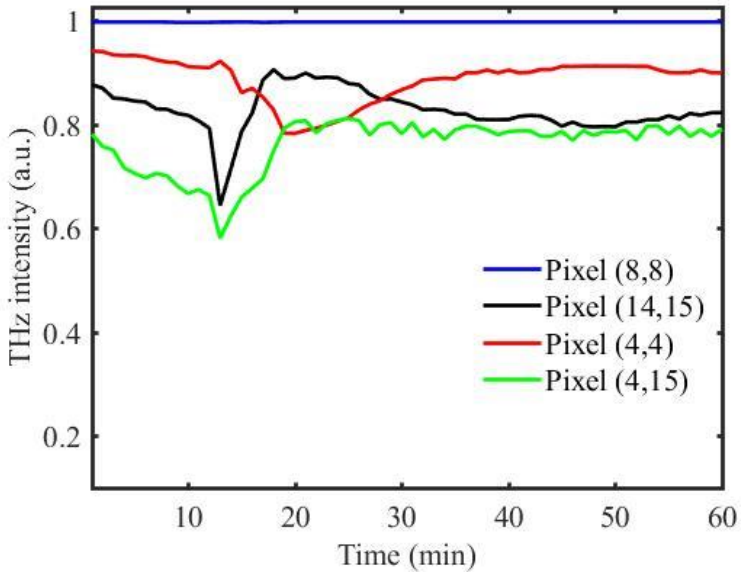

Figure 4.12 - Pixel intensity evolution of 4 selected pixels across 60 minutes. Legend should be read as Pixel (x coordinate, y coordinate).

To evaluate our hypothesis, the setup was moved to an optical table with vibration isolator supports and repeated the experiment with the N-117 membrane. Figure 4.13 shows the terahertz images at the start (4.13a) and end (4.13b) of the 60 minutes process.

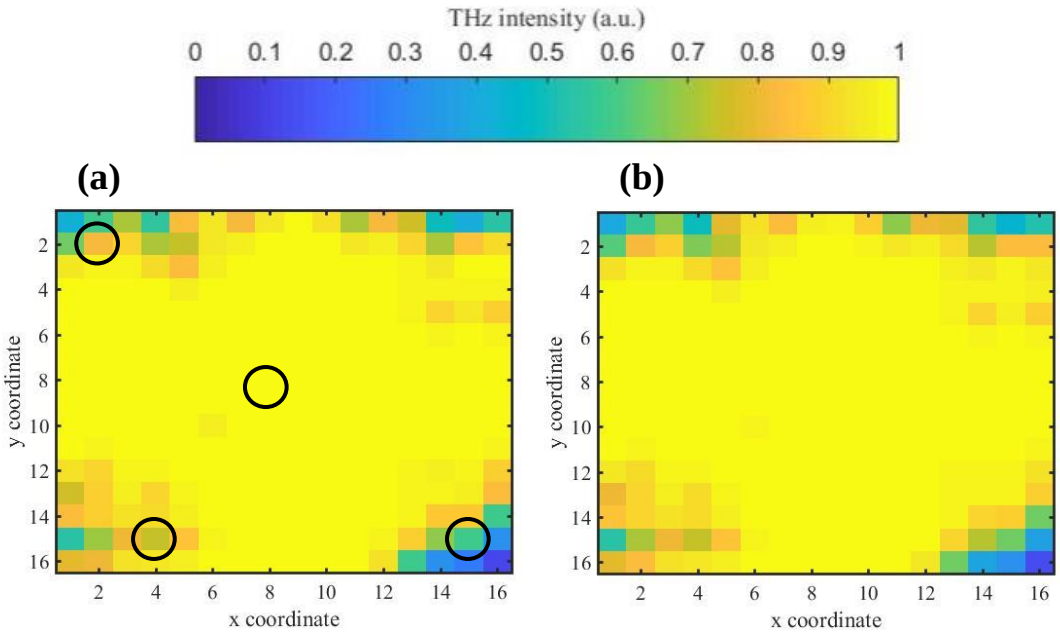

Figure 4.13 - Terahertz false colour images of a Nafion N-117 membrane at (a) 1 min and (b) 60 min. Black circles in (a) highlight 'dimmer' pixels selected for analysis.

Like Figure 4.11, attenuation occurs mostly around the edges and corners of the image. In addition, the images are similar, which implies that vibration isolation eliminates the intensity oscillations shown in Figure 4.12. This is further reinforced by Figure 4.14, as the pixels' intensity is mostly constant, with small fluctuations associated with system noise. These images confirm the previous hypothesis of vibration isolation reducing noise related to the imaging setup.

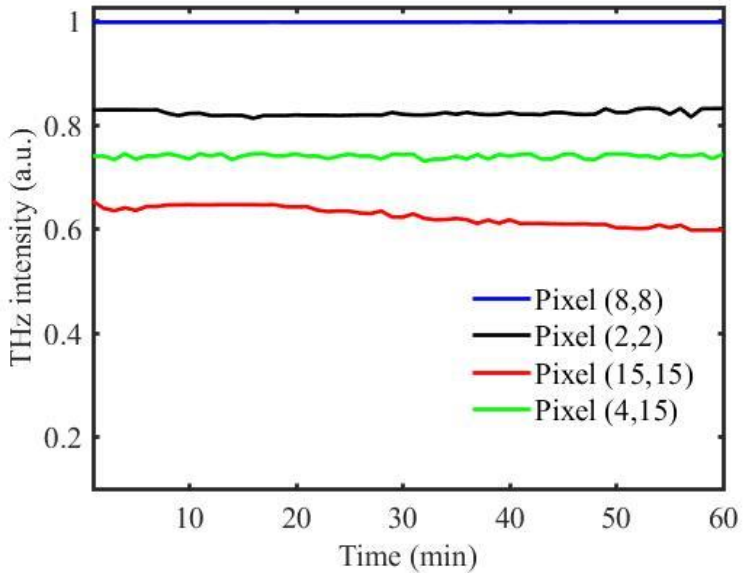

Figure 4.14 - Pixel intensity evolution of 4 selected pixels across 60 minutes. Legend should be read as Pixel (x coordinate, y coordinate)

4.3. Summary

In this chapter, the feasibility of a portable, inexpensive terahertz imaging system to quantify and image liquid water content across Nafion PEMs was investigated. The system's sensitivity to quantify liquid water in the 25-500 μm thickness range has been demonstrated, where the system is insensitive to thicknesses less than 25 μm. Under the assumption that membrane thickness can be taken as water thickness, water weight loss was estimated using terahertz measurements for a desorption process while simultaneously monitoring the weight change. The outcomes agree with gravimetric analysis and consistent with previously studies despite discrepancies due to residual surface water and liquid water outside the measurement window. Imaging of liquid water spatial distribution and movement across a partially hydrated Nafion N-117 membrane during a room temperature desorption process was also achieved, which is otherwise not possible with gravimetric techniques. Finally, the source of imaging noise observed around the camera's edges during measurement was identified as random vibrations from environmental sources, which can be improved by attaching the terahertz imaging system to a stabilized table with vibration isolator supports. Although the Nafion manufacturing industry for high-performance PEMFC applications is trending towards thinner membranes (~15 μm) [290], [291] due to reduced proton resistance and better fuel cell performance [7], the proposed system has been demonstrated to be suitable for thicker membranes (50-254 μm), which is still relevant for PEMFC-related scientific studies [292], [293], and electrochemical applications such as PEM-electrolysis [11], [294] or vanadium redox-flow batteries [295]. For thinner, state-of-the-art Nafion membranes for PEMFC, owing to the higher water sensitivity, THz-TDS is a more suitable alternative. Another advantage is the low-cost nature of the terahertz imaging system, especially compared to a commercial THz-TDS system. In summary, the proposed system offers an interesting modality, and can potentially be used with vibration isolation as a non-destructive, cost-effective complementary alternative for liquid water inspection of Nafion PEM as part of future Nafion manufacturing quality control strategy.

5. Observations of liquid water accumulation in PEMFC with terahertz radiation

Moving to the original goal of this Dissertation, this Chapter employs a similar terahertz imaging system to image water build-up inside an operating PEMFC. Using a custom-built laboratory-scale, terahertz and optically transparent PEMFC, phenomena of water accumulation and transport (membrane hydration, flooding) are imaged. Results agree with simultaneous optical imaging and electrochemical measurements. To demonstrate the potential use of the proposed terahertz imaging for process understanding, the effect of air gas flow rates on flooding is investigated.

5.1. Introduction

Widespread adoption of PEMFCs has been plagued by technical obstacles such as sluggish ORR kinetics, high cost and insufficient lifetime [5]. Water management plays a significant role in the operational performance and durability of PEMFCs. Water presence in a PEMFC is caused by electrochemical generation at the cathode by the oxygen reduction reaction and droplet condensation from humidified inlet gases along with water transport mechanisms across the PEM such as electro-osmotic drag and back diffusion [53]. Given that the vast majority of PEMFCs use perfluorinated sulfonic-acid ionomers as the solid PEM, insufficient hydration can lead to a reduced proton conductivity resulting in cell performance loss and possible permanent material damage [13]. On the other hand, where the cell's rate of water production surpasses inlet gases' transport capacity, flooding results potentially clogging up gas channels and filling up the pores of the catalyst layer or GDL further reducing cell performance [14]. Understanding the dynamics of water transport and distribution inside an operating PEMFC is therefore important for developing effective water management strategies [296].

The Chapter 2 of this Dissertation extensively presents and reviews the main water visualisation methods in PEMFCs. In general, MRI, neutron imaging and X-ray radiography can provide in-situ information on liquid water transport across optically opaque layers, but due to the excessive cost associated with these instruments, accessibility is not always guaranteed. Infrared imaging typically employs compact and video-rate devices to image samples with high spatial resolution (~ 5 μm) but suffers from a limited penetration depth. Fluorescence microscopy can visualise microscale water transport patterns inside the GDL but has not been demonstrated on an operating PEMFC to the authors' best knowledge. Using video-rate devices operating with a relatively high spatial resolution (1-10 μm), optical imaging has been applied to inspect liquid water within optically transparent PEMFCs [15], [16], often in reflection due to the opacity of GDL layers. This imaging modality can provide crucial insights into several two-phase flow phenomena inside channels, such as single-phase, droplet, film and slug flows [132]. This in turn can be used to study the impact of many parameters, such as GDL structures [117], [123], [127] cathode stoichiometry [126], flow field configurations [124] and process conditions [297] on water accumulation and transport inside PEMFC flow channels. However, processing a large dataset of optical images can quickly become prohibitively labour intensive [132], [298] and a lack of contrast [17] can lead to misinterpretation.

Building on Chapter 4's work on terahertz focal plane array imaging of hydrated Nafion PEMs [267], Chapter 5 presents an investigation on the feasibility of a similar video-rate terahertz imaging system for direct water visualisation inside of a custom-built PEMFC through a terahertz and optically transparent window supported by complementary high-resolution optical imaging and conventional electrochemical measurements.

5.2. Results and discussion

5.2.1. Electrochemical performance

Figure 5.1 shows a representative I-V polarization curve of the custom-built PEMFC under the conditions of Exp. 1. Although the performance is lower than an air breathing non-pressurized PEMFC [299], it is consistent and comparable to other transparent PEMFCs designed for water visualization, which also underperform compared to conventional counterparts [297], [300], which usually amounts to 1.5-2 A/cm^2 current density at 0.6 V cell voltage in state of the art fuel cells [301]. The reduced performance is likely to be caused by a combination of large flow channel/rib width [302], transparent cut-out and practical difficulties encountered in manual compression/seal of a large area PEMFC [303]. However, it is important to re-emphasize that the objective of the study was to maximize water production to be imaged with the terahertz setup while maintaining stable performance, rather than achieving an optimized, state of the art PEMFC. Thus, the current density of 0.04 A cm^{-2} was selected for operation, which is located at an unconventional position on the polarization curve (0.1-0.2 V).

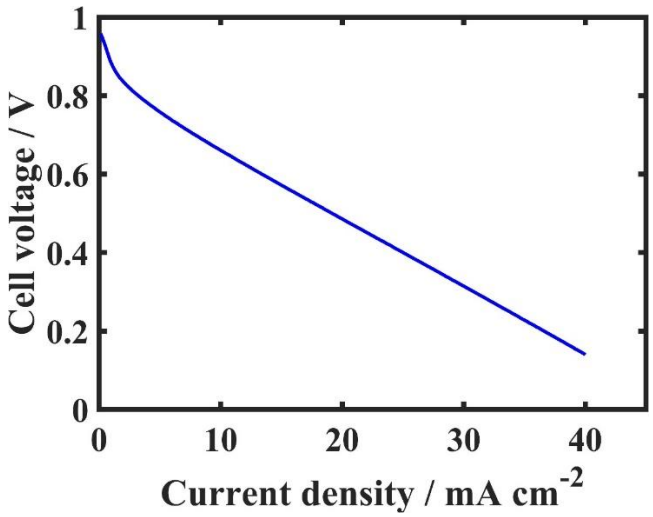

Figure 5.1 – PEMFC polarization curve under the operating conditions of Exp. 1.

5.2.2. Liquid water visualisation

Figure 5.2 shows the water accumulation measured by the respective techniques across 300 min. Faraday's law of electrolysis states that mass of elements deposited on an electrode is directly proportional to the charge Q (units: A.s). In the simple case of constant current:

$$Q = I * t \tag{5.1}$$

where *I* corresponds to applied current and *t* to total time the constant current was applied. This leads to:

$$\frac{V_{H_2O}}{t} = \mathrm{VG}_{H_2O} = \frac{I*M_{H_2O}}{F*\upsilon*\rho_{H_2O}} \tag{5.2}$$

where V_{H2O} is the water volume generated, VG_{H2O} is the water volume generated over time, M_{H2O} is the molar mass of water (18 g/mol), *F* is the Faraday's constant (96485.3329 A.s/mol), υ is the valency of the ions (2) and ρ_{H2O} is the water's density (1000 kg/m^3). Assuming no cell shorting or parasitic reactions, with a constant applied current of 4 A the amount of water generated electrochemically is 0.0224 cm^3/min. The volume of the transparent cut-out is approximately 0.5 cm^3 and the optical area occupied by water at 100 min and at the peak of 230 min was 20% and 65%, respectively. These therefore correspond to an estimated water volume of 0.1 cm^3 and 0.3 cm^3. At 100 and 230 min, water production amounted to approximately 2.2 cm^3 and 5.2 cm^3, which are an order of magnitude higher than the observed flooding. Furthermore, 2% (w/w) absolute humidity on the cathode inlet, means that 7.5 mg of water per minute (on a 300 cm^3/min gas flowrate) is entering the cathode flow channels. However, as the cell is operating at high cathode stoichiometry, excess gas is flowing part of the generated water out of the PEMFC. However, there is sufficient water build-up from downstream accumulation to observe flooding in the transparent cut-out. It is important to note that mechanisms such as water diffusion and back diffusion in the PEM are not accounted for, as only the condensed and electrochemically generated water on the cathode side are being studied.

Cell voltage displays several spontaneous fluctuations (electrochemical noise) outside of our observation region, caused by physical phenomena related to water mass transport and accumulation [304]. The imaging curves show a good agreement, and the overall trend is a continuous growth consistent with water build-up, except for a sharp decrease around 225 min. However, they present considerable complexity and slight discrepancies between them, indicating the occurrence of distinct water transport phenomena and divergences between the

measurements. For this reason, it has been divided into three sections according to the specific phenomena: membrane hydration (S1), main droplet appearance, water pool formation and flooding (S2), and flushing (S3). These chronological sections will be analysed in detail in the following sub-sections. Table 5.1 lists the time duration for each of the sections.

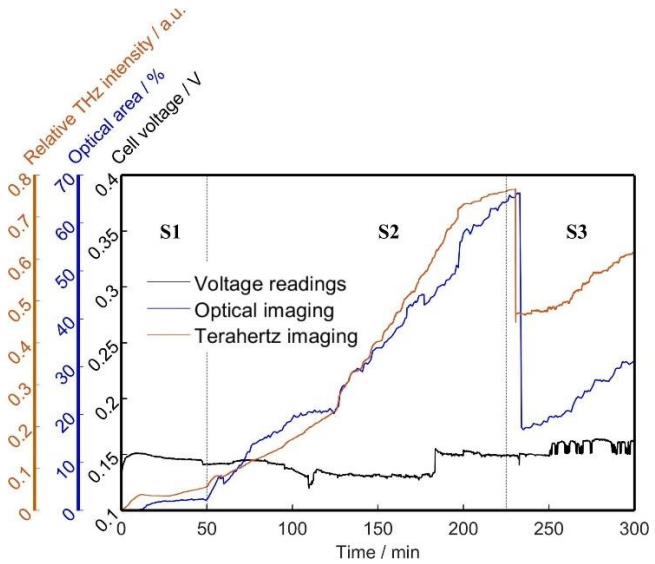

Figure 5.2 – Water accumulation during Exp. 1 probed by terahertz imaging, optical imaging, and cell voltage readings. Dashed lines and labels show the time stamps of the sections.

Table 5.1 - Periods for each of the sections of Exp. 1 presented in Figure 4.5.

Section	1	2	3
Time / min	0-50	50-225	225-300

Membrane hydration (S1)

Figures 5.3a-d show a sequence of images representing membrane hydration at 1 and 30 min. Optical images show curve and wedge-shaped deformations caused by Nafion swelling [305]–[308], gas pressure differentials pushing the membrane towards the anode and minor droplet condensation. During this time, processed terahertz images show an increased pixel intensity, whose curve pattern exhibits logarithmic growth. This is consistent with prior *ex situ* Nafion membrane hydration studies [267] and concurrent voltage readings. As the optical regime is less sensitive to water, the degree of hydration is inferred from the degree of swelling. This results in notable discrepancies between the terahertz and optical curves (Figure 5.4), particularly the 9 min delay and differing time constants (13 and 32 min, respectively). The former is related to the curve and wedge-shaped deformations used to quantify the degree of

swelling can only be tracked after 9 min of operation; the latter is an indication of unreliable tracking of membrane deformation via optical image processing for membrane hydration. This highlights the advantage terahertz being sensitive to membrane hydration where significant image processing are not required [267]. It should be noted that there is some discrepancy between terahertz and voltage data due to membrane deformation [267] and a mismatch in the region for measurement, as cell voltage is being taken across the entire membrane as opposed to a localized area viewed by terahertz and optical imaging.

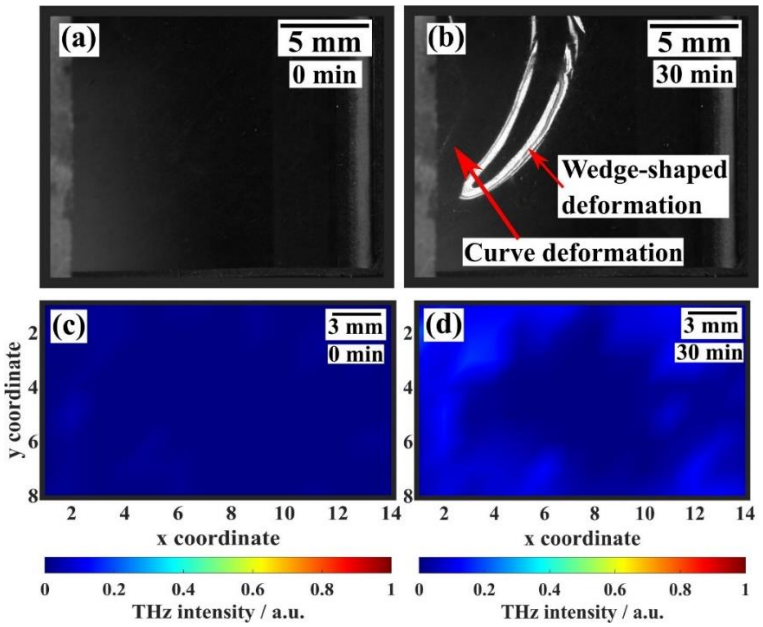

Figure 5.3 - Membrane hydration captured by optical images at (a) 1 min, and (b) 30 min and terahertz false colour images at (c) 1 min and (d) 30 min of Exp. 1. Curved and wedge-shaped deformations are highlighted in (b).

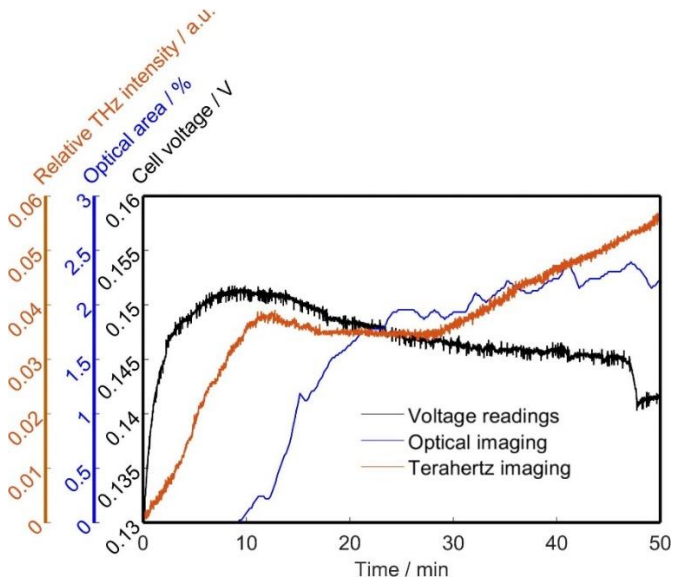

Figure 5.4 – Zoomed-in S1 of Figure 4.5.

Water pool formation and flooding (S2)

Figures 5.5a-f show the optical images capturing the main droplet (on the right-hand side), its growth into a water pool and eventual flooding causing gas flow blockage on the cathode. The main droplet occurrence typically manifests as droplets emerging from underneath the GDL surface once the membrane becomes saturated [120], [132], [300]. However, given the lack of a GDL here, the main droplet forms from the coalescence of small water films on the position farthest away from the transparent cut-out's gas entrance. Figure 5.6 shows a good agreement between optical area and terahertz intensity curves, demonstrating terahertz imaging's ability to efficiently track water accumulation in the cathode side of the transparent cut-out. Terahertz images for the time (Figures 5.5g-l) follow a pattern consistent with optical observations. In particular, the flooding progress can be observed and other events such as the main droplet appearance (Figure 5.5g) and sudden increase (61.3%) in water volume (Figures 5.5i-j) are identified. Furthermore, main droplet appearance can be determined by two pronounced dips between 50-60 min in Figure 5.6. These are caused by the physical descent of the droplet onto the bottom corner of the cut-out, limiting the visibility of both techniques twice, thus decreasing the terahertz signal and optical area. The slight time delay between the techniques is related to the difference of frame rates (30 Hz and 0.2 Hz for terahertz and optical, respectively). Additionally, it is hypothesized that the water volume surge between 125-130 min results from upstream flushing of excess water, but the mechanism is subject to further study. Although the increase in terahertz intensity associated with these subtle events can provide qualitative feedback, owing to the poor spatial resolution (1.5 mm) of the terahertz camera, interpretations of the state of PEMFC needs to also consider of the electrochemical and optical measurements despite challenges associated with optical imaging processing.

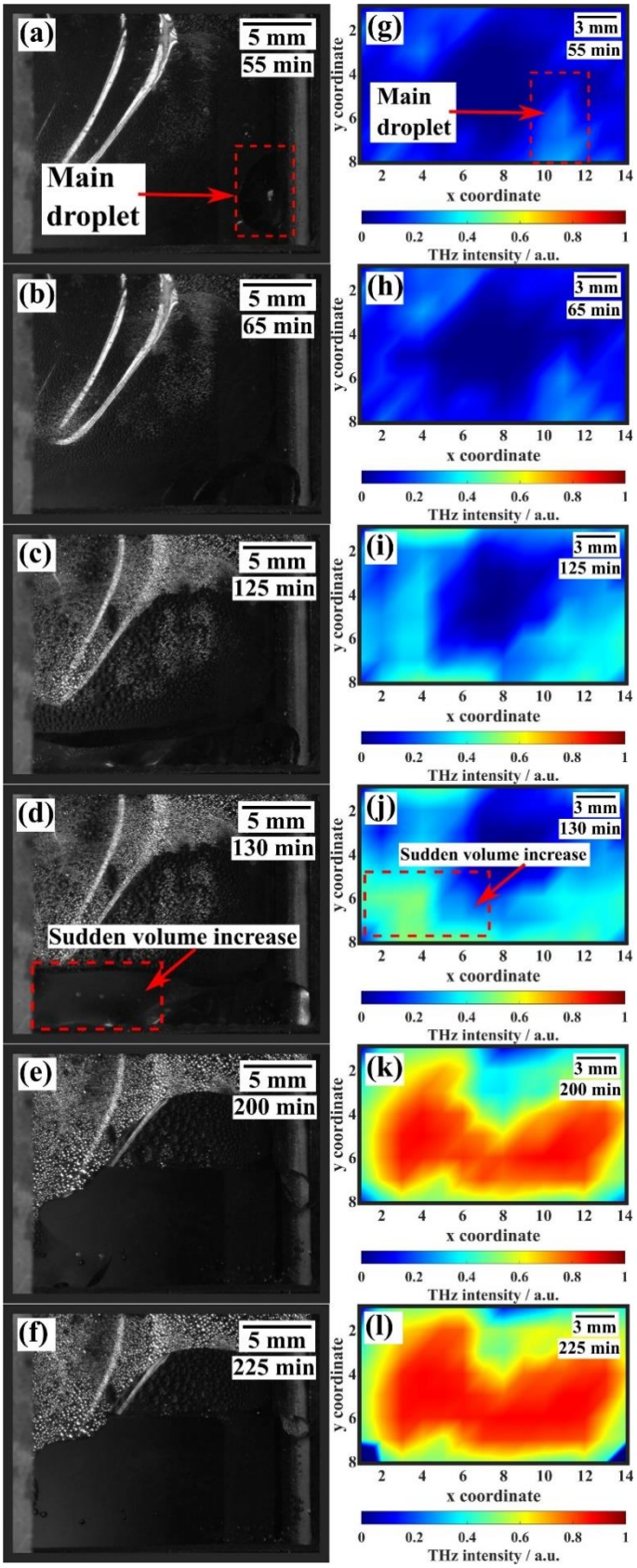

Figure 5.5 - Water pool formation and flooding captured by optical images at (a) 55 min, (b) 65 min, (c) 125 min, (d) 130 min, (e) 200 min and (f) 225 min and terahertz false colour images at (g) 55 min, (h) 65 min, (i) 125 min, (j) 130 min, (k) 200 min and (l) 225 min. Highlighted areas show the spatial locations of the main droplet and sudden increase in water volume.

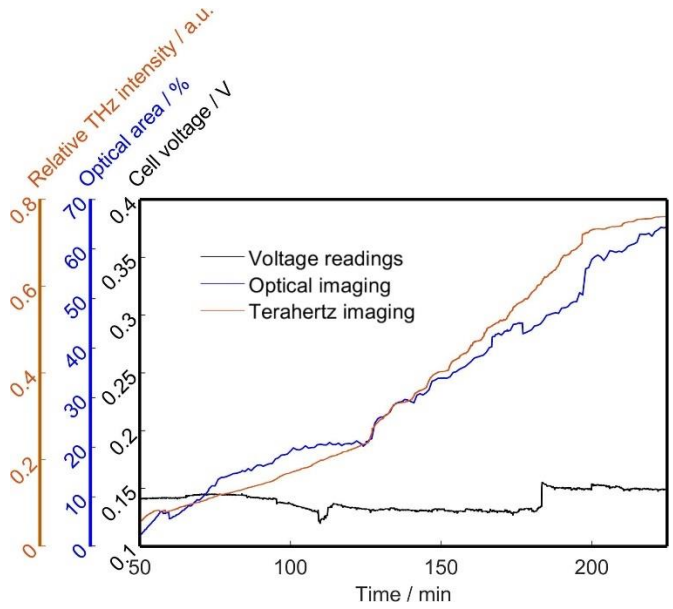

Figure 5.6 - Zoomed-in S2 of Figure 4.5.

Flushing of accumulated water (S3)

Figures 5.7a-c present optical evidence of accumulated water flushing between 225-235 min, which coincides to significant intensity decrease in terahertz difference images (Figures 5.7d-e). Both measurements report a decrease by approximately 42% and 74% for terahertz relative intensity and optical area, respectively (Figure 5.8). This is partly due to differences in the measurements taken: optical imaging analysis focusses solely on the water pool while the terahertz beam is probing water throughout the cell including membrane; droplet condensation and water pool. Thus, even though significant water is flushed away, other sources of water absorption remain resulting in a lower drop in terahertz intensity. This event also coincides with a sharp dip in cell voltage in Figure 5.8: as the gas path is blocked by flooding, there is a negative spike in cell voltage; this also results in a sudden build-up of gas pressure, which promptly removes accumulated water and restores the cell voltage.

Figure 5.7c shows vertical growth in water pool size which agrees well with the terahertz difference image (Figure 5.7f). Finally, the increase in terahertz intensity on the left side is attributed to significant droplet condensation, which can be challenging to quantify with the current optical imaging processing routine.

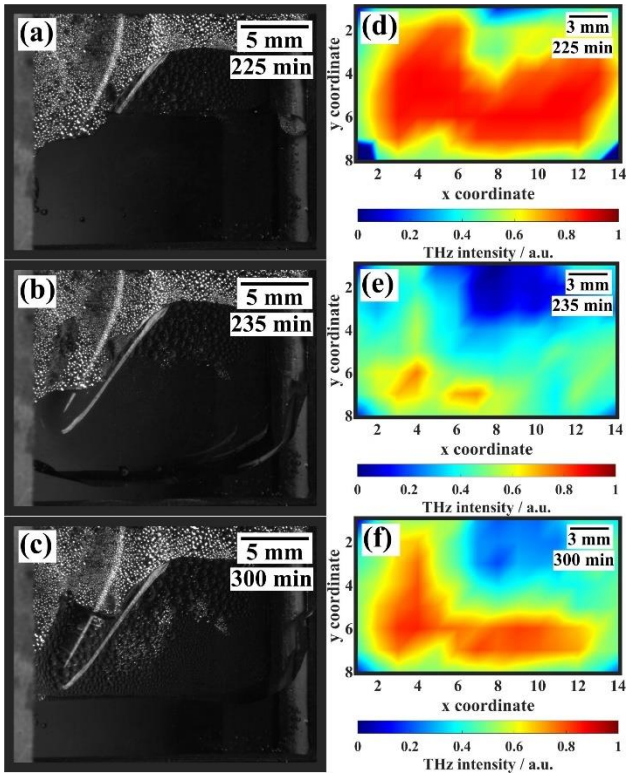

Figure 5.7 – Flushing of accumulated water, and continued water pool growth captured by optical images at (a) 225 min, (b) 235 min, (c) 300 min and terahertz false colour difference images at (d) 225 min, (e) 235 min, and (f) 300 min of Exp. 1.

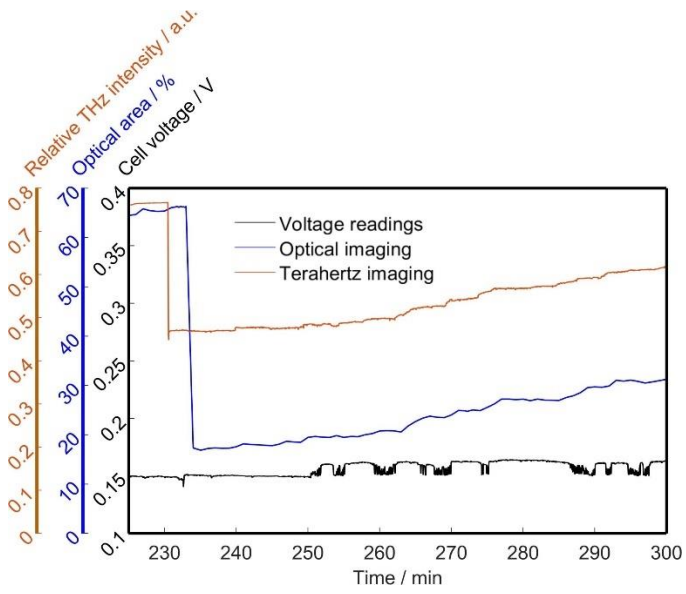

Figure 5.8 – Zoomed-in S3 of Figure 4.9.

5.2.3. Effect of air flow rates

Figure 5.9 compares terahertz intensities during the Exp.2 and 3, which correlate well with its respective optical measurements (Figure 5.10). The curves follow a similar pattern observed in Figure 5.2, particularly the sequence of membrane hydration followed by main droplet

appearance, growth into a water pool, flooding, and excess water flush out and further water accumulation. Additionally, they follow the general trend of lower operating humidified air flow leading to faster water accumulation in the transparent cut-out. This is clearly shown on the delay of accumulated water flushing, as the amount of water required to block the channel takes longer to accumulate if water build-up is slowed by stronger gas flow. These are plausible evidence that the proposed system can visualise variations in flooding patterns with increasing air flow rates. Nevertheless, there are instances of unexpected discrepancies, particularly in the membrane hydration times, main droplet formation and terahertz intensity slopes at certain time periods. Further explanation of the observed inconsistencies requires additional validation methods and a more detailed study, beyond the scope of the current work.

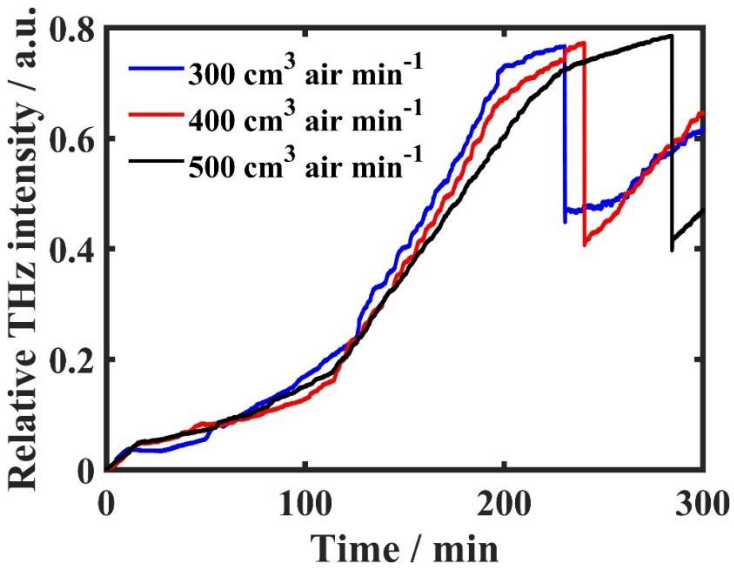

Figure 5.9 – Evolution of terahertz intensity under different flow rates.

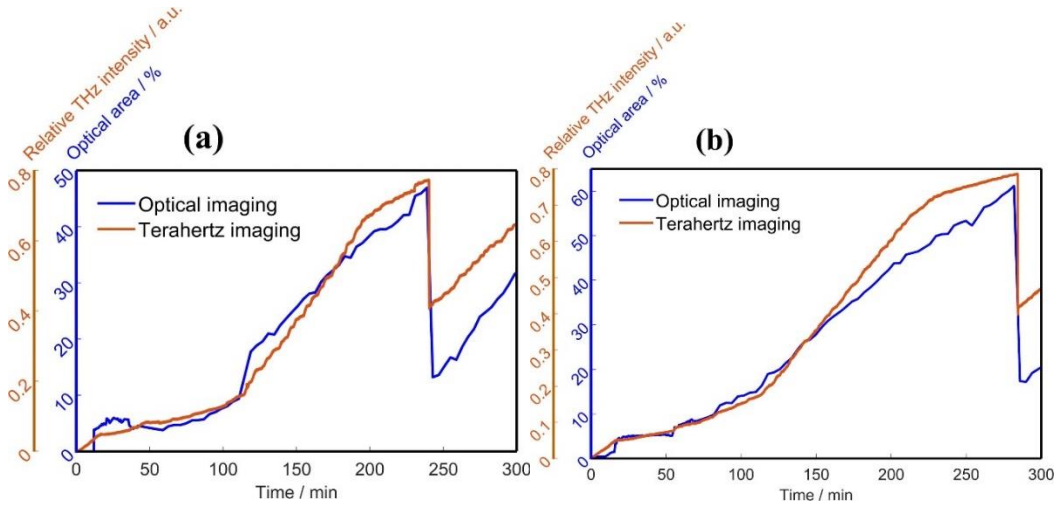

Figure 5.10 – Time evolution of water accumulation during Exp. 2 and 3 probed by terahertz and optical imaging.

5.3. Summary

In this Chapter, we have investigated the feasibility of a portable, inexpensive terahertz video-rate imaging to inspect water transport and accumulation inside a custom-built, operating PEMFC. We have observed various phenomena such as membrane hydration, main droplet appearance, water pool formation and growth as well as flushing of accumulated water. These results are in good agreement with simultaneous optical imaging and voltage readings. To demonstrate the sensitivity of terahertz imaging for process investigation, we have also monitored terahertz intensity changes in response to changing compressed air flow rates where there is agreement with the general trend of higher gas flowrates resulting in slower water accumulation. Thus, we state that the proposed system is a sensitive, contactless, non-destructive, and cost-effective technique with clear potential to complement existing characterization techniques for fuel cell operational understanding, particularly to assess novel flow field configurations. However, comparisons of the proposed terahertz imaging against the relatively more established optical measurements highlight potential areas of improvement, e.g. a need to reduce intrinsic and environmental noise, enhance sensitivity to small amounts of water (< 25 μm) [267] and improved spatial resolution, possibly via image interpolation methods such as Gouraud shading. With technological advances being made on higher resolution terahertz imaging cameras, such as microbolometers operating with sub-mm resolution [309], this will open up the possibility to image PEMFCs implemented with conventional designs operating under realistic scenarios, such as 1 mm wide channels.

6. Dissertation summary

This Chapter summarises the work described in this Dissertation by outlining the research described in previous chapters and discussing future work. Chapter 1 introduces the PhD topic and motivations. Chapter 2 discusses fundamentals of PEMFCs, terahertz science and technology and thoroughly reviews the state of the art of water visualisation techniques. Chapter 3 describes the methodology applied in the experimental studies reported in this Dissertation, Chapter 4 studies the feasibility of a simple terahertz imaging system to study hydration in Nafion PEMs. Chapter 5 employs the same imaging system to inspect flooding in a transparent PEMFC.

6.1. Conclusions

This Dissertation is aimed at investigating the potential of a novel terahertz imaging system for PEMFC-related applications. It has been demonstrated to investigate hydration levels in Nafion PEMs and diagnose flooding in a transparent PEMFC.

In terms of hydration imaging in Nafion PEMs, a simple terahertz imaging setup comprising a 0.1 THz IMPATT diode terahertz source, a FPA terahertz camera with 16x16 pixel array and TPX collimator lens was realised in transmission geometry and horizontal positioning. Through testing with an in-house made liquid cell, it was found that it could quantify water presence between 25 and 500 μm thickness values via Beer-Lambert law. It is important to note that the data followed theoretical values with minimal standard deviation between 200-250 μm water thicknesses. Thicknesses below these display a similar trend, but results are slightly deviated and present much higher deviation, leading to the conclusion that the system is less accurate in this region. Furthermore, at 500 μm water thickness, beam attenuation is approximately 99.5%, which is at the edge of camera detection limit and thus measurements incur a degree of uncertainty. This possibility of water thickness quantification led to a study of water weight quantification in Nafion membranes with thickness ranges between 50-254 μm, assuming that membrane thickness is comparable to the water thickness within itself, constant water density and uniform water content distribution. To validate the study, the system was supplemented with a weight balance to perform simultaneous gravimetric measurements. The independent measurements agreed well but displayed local discrepancies in slope and values related to residual surface water and limited membrane/gas interface at certain locations within the membrane, out of the camera's view. These discrepancies challenge the assumption of uniform water distribution in a vertically mounted sample, where gravity may have influence. It is important to inform that the author has realised a similar imaging system in a vertical arrangement, to eliminate the effect of gravity and the data discrepancies. Additionally, the membrane samples were larger (70x70 mm^2) than the camera (24x24 mm^2) to circumvent the limitation of adverse image effects around the sample's edges. If the investigated samples cannot be larger than the camera, these effects will be shown as darker pixels around the edges, erroneously showing water presence. The recommendation is to carefully select the pixels used for analysis and extrapolate the water weight estimation to the entire area. This method has been employed successfully in biomedical membrane studies performed by the author. Lastly, given the possibility of acquiring full images at video-rate, imaging of a partially hydrated

Nafion PEM where distinct dry and hydrated regions were clearly observed. Closer inspection of the acquired images revealed spatial variations in dehydration rates along with imaging noise effects. These effects were attributed to unrestrained in-plane membrane swelling and environmental vibrations. The former could be fixed by sandwich the membrane between plastic plates, thereby restricting its movement. However, this introduces the measurement uncertainty via the possibility of droplet condensation between the membrane and plastic plates. The latter can be mitigated by mounting on an optical table with suitable vibration isolation supports.

In terms of flooding diagnosis in a PEMFC, a transparent PEMFC was realised, and a similar terahertz imaging system was used in transmission geometry. The PEMFC's electrochemical performance was comparable to other fuel cells in visualisation studies and thus deemed suitable for the study. To minimise the effect of the terahertz camera's limited spatial resolution, high-resolution optical camera measurements were performed simultaneously. Two-phase flow phenomena were observed, such as membrane hydration, first droplet occurrence, water pool formation, growth, and subsequent flushing with good agreement between optical, terahertz and electrochemical readings. Additionally, the effect of increasing air flow rate was observed on the rates of water accumulation. This combined imaging system can provide interesting insight for flooding diagnostics and novel component testing, given that optical is able to spatially resolve water presence with high resolution on one side of the fuel cell, while terahertz is able to image water thickness across both sides with good sensitivity. In retrospective, it is clear to the author that a 100 cm^2 with a cut-out on active MEA area for water visualisation and 5 mm wide gas channels does not resemble an industry standard PEMFC or those described in PEMFC design and testing literature. Additionally, the terahertz water response is convoluted between anode channels, PEM hydration and cathode channels, which makes discrimination of contributions challenging. Ideally, the next step would be to realise a PEMFC closer to state-of-the-art status and perform in situ flooding diagnostics without the need for MEA cut-outs.

To be concluded, the objective of the PhD project has been fulfilled: to the author's knowledge, it is the first time a novel terahertz imaging system based on an FPA terahertz camera was demonstrated for PEMFC applications. Moreover, the results have been successfully benchmarked against established techniques such as gravimetric, optical imaging and electrochemical testing.

6.2. Future work

Recommendations on how the studies presented in this Dissertation can be expanded or improved upon are listed below:

- Higher spatial resolution: the most critical downside of this technique is the low spatial resolution (1.5 mm) of the FPA camera. As explained in Chapter 2.3.1, the evolution of terahertz science and technology over the last decade has resulted in a myriad of readily available table-top devices. A thirty-fold increase in spatial resolution can be achieved via FPA cameras based on micro-bolometer arrays (~ 50 μm), such as the Swiss Terahertz RIGI S2x. At a spatial resolution of tens of micrometres, minute details such as droplet formation on the GDL surface, film coalescence and slug blockage of gas flow could be observed. However, the IMPATT diode source employed in this study irradiates terahertz light at 0.1 THz, which is at the edge of the sensitivity range of the RIGI S2x, according to the manufacturer's specifications [309], and ideally higher frequency sources (0.3 THz) are preferred. This can pose a problem as water absorption coefficient rises sharply with increasing frequency in the terahertz band [264], and thus penetration may be limited. Additionally, higher resolution of micro-bolometer arrays comes with a two-fold price increase compared to the Terasense FPA camera employed in this study. Given the data presented in this Dissertation, the growth of terahertz science and technology and the possibility of sensing water transport mechanisms at microscale range, it will compensate for the increase in price.
- Reflection geometry terahertz measurement: water presence in distinct PEMFC layers can be difficult to discern with a terahertz imaging system in transmission geometry. Ideally, adopting a reflection geometry would allow terahertz light to reflect off the GDL carbon surface, where water transport and accumulation on the flow channels can be studied. Furthermore, water presence in the cathode and anode compartments could be differentiated. Thus, when designing the flooding observation studies in fuel cells with terahertz radiation (Chapter 5), imaging in reflection geometry was the natural choice. However, during preliminary studies beam alignment was challenging, time-consuming and thus never achieved to an adequate standard. This was the case for both normal and angle-incidence measurement modes. Sub-optimal beam alignment caused inconsistent results when performing ex-situ water imaging studies on rigs with acrylic windows featuring simple machined patterns (squares, single lines), reflecting off

polished metal surfaces. Therefore, moving to a reflection measurement on an operating fuel cell with complex channel features (ribs, U-turns) and non-ideal reflective surface (porous GDL) would have been problematic due to overlapping imaging noise from all these characteristics. Thus, given the limited time of a PhD project, reflection geometry measurements were abandoned and replaced with simpler transmission geometry measurements. Nevertheless, it is important to note that upon achieving a successful reflection terahertz imaging setup with micro-bolometer arrays, this technique could provide insight into water dynamics in the channels with greater sensitivity than optical imaging.

- Hydration imaging in miscellaneous planar and hydrophilic materials: the concept presented in Chapter 4 can be expanded into other types of materials, providing key insight into spatially resolved water absorption patterns. The single requirement is semi-transparency of the dry material at terahertz frequencies. Over the course of the PhD project, the author has successfully characterised eggshell membranes [310] and hydrogels modified with *aloe vera* [311] for wound dressing.
- Terahertz time-domain spectroscopy: compared video-rate terahertz imaging, THz-TDS can provide more in-depth information on material properties (including water content) due to the pulsed and broadband nature of the technique. This allows for simultaneous extraction of magnitude and phase of the terahertz waves, without resorting to complicated Kramers-Kronig relations, and access to higher frequencies. However, it is a single-point measurement (~ 1mm spot size), and thus measurements over large areas are achieved through raster scanning, which inadequate for monitoring dynamic processes. Thus, flooding observations in fuel cells with THz-TDS is unlikely to provide any advantage over optical, infrared and terahertz video-rate imaging.

  However, due to its characteristics, this technique can still be useful for fuel cell related studies. For example, for deeper examination of water content in Nafion, particularly the degree of hydrogen bonding to the sulfonic acid sites and water states (bulk, bound, free) inside the membranes [247]. This can provide critical feedback loop information for Nafion manufacturing from a table-top instrument. Additionally, terahertz sensitivity to hydrogen bonds and conductive materials, it could potentially be used for in-line monitoring of inkjet printing of catalyst layers and perform off-line quality control. The studied parameters can include residual solvent presence after printing, as

well surface roughness and spatially resolved defects of optically opaque printed catalyst layers.

References

[1] T. Zhang, P. Wang, H. Chen, and P. Pei, “A review of automotive proton exchange membrane fuel cell degradation under start-stop operating condition,” *Applied Energy*. 2018, doi: 10.1016/j.apenergy.2018.04.049.

[2] H. W. Wu, “A review of recent development: Transport and performance modeling of PEM fuel cells,” *Applied Energy*. 2016, doi: 10.1016/j.apenergy.2015.12.075.

[3] P. Pei and H. Chen, “Main factors affecting the lifetime of Proton Exchange Membrane fuel cells in vehicle applications: A review,” *Applied Energy*. 2014, doi: 10.1016/j.apenergy.2014.03.048.

[4] H. Chen, S. Xu, P. Pei, B. Qu, and T. Zhang, “Mechanism analysis of starvation in PEMFC based on external characteristics,” *Int. J. Hydrogen Energy*, 2019, doi: 10.1016/j.ijhydene.2018.11.135.

[5] X. X. Wang, M. T. Swihart, and G. Wu, “Achievements, challenges and perspectives on cathode catalysts in proton exchange membrane fuel cells for transportation,” *Nature Catalysis*. 2019, doi: 10.1038/s41929-019-0304-9.

[6] X. R. Wang, Y. Ma, J. Gao, T. Li, G. Z. Jiang, and Z. Y. Sun, “Review on water management methods for proton exchange membrane fuel cells,” *Int. J. Hydrogen Energy*, 2020, doi: 10.1016/j.ijhydene.2020.06.211.

[7] A. Kusoglu and A. Z. Weber, “New Insights into Perfluorinated Sulfonic-Acid Ionomers,” *Chem. Rev.*, vol. 117, no. 3, pp. 987–1104, 2017, doi: 10.1021/acs.chemrev.6b00159.

[8] M. B. Karimi, F. Mohammadi, and K. Hooshyari, “Recent approaches to improve Nafion performance for fuel cell applications: A review,” *Int. J. Hydrogen Energy*, vol. 44, no. 54, pp. 28919–28938, 2019, doi: 10.1016/j.ijhydene.2019.09.096.

[9] T. Xiao, R. Wang, Z. Chang, Z. Fang, Z. Zhu, and C. Xu, “Electrolyte membranes for intermediate temperature proton exchange membrane fuel cell,” *Progress in Natural Science: Materials International*. 2020, doi: 10.1016/j.pnsc.2020.08.014.

[10] A. Siu, J. Schmeisser, and S. Holdcroft, “Effect of water on the low temperature conductivity of polymer electrolytes,” *J. Phys. Chem. B*, 2006, doi: 10.1021/jp0531208.

[11] H. Ito, T. Maeda, A. Nakano, and H. Takenaka, “Properties of Nafion membranes

under PEM water electrolysis conditions," *Int. J. of Hydrog. Energy*, vol. 36, no. 17. pp. 10527–10540, 2011, doi: 10.1016/j.ijhydene.2011.05.127.

[12] M. Schalenbach, W. Lueke, W. Lehnert, and D. Stolten, "The influence of water channel geometry and proton mobility on the conductivity of Nafion®," *Electrochim. Acta*, vol. 214, pp. 362–369, 2016, doi: 10.1016/j.electacta.2016.08.010.

[13] J. Wu *et al.*, "A review of PEM fuel cell durability: Degradation mechanisms and mitigation strategies," *J. Power Sources*, vol. 184, no. 1. pp. 104–119, 2008, doi: 10.1016/j.jpowsour.2008.06.006.

[14] P. Pei, Y. Li, H. Xu, and Z. Wu, "A review on water fault diagnosis of PEMFC associated with the pressure drop," *Appl. Energy*, vol. 173, pp. 366–385, 2016, doi: 10.1016/j.apenergy.2016.04.064.

[15] A. Bazylak, "Liquid water visualization in PEM fuel cells: A review," *Int. J. Hydrog. Energy*, vol. 34, no. 9, pp. 3845–3857, 2009, doi: 10.1016/j.ijhydene.2009.02.084.

[16] S. Tsushima and S. Hirai, "In situ diagnostics for water transport in proton exchange membrane fuel cells," *Prog. Energy Combust. Sci.*, vol. 37, no. 2, pp. 204–220, 2011, doi: 10.1016/j.pecs.2010.06.001.

[17] J. St-Pierre, "PEMFC In Situ Liquid-Water-Content Monitoring Status," *J. Electrochem. Soc.*, vol. 154, no. 7, p. B724, 2007, doi: 10.1149/1.2737542.

[18] H. Elayan, O. Amin, B. Shihada, R. M. Shubair, and M. S. Alouini, "Terahertz band: The last piece of rf spectrum puzzle for communication systems," *arXiv*. 2019, doi: 10.1109/ojcoms.2019.2953633.

[19] G. A. Mourou and K. E. Meyer, "Subpicosecond electro-optic sampling using coplanar strip transmission lines," *Appl. Phys. Lett.*, 1984, doi: 10.1063/1.95312.

[20] P. R. Smith, D. H. Auston, and M. C. Nuss, "Subpicosecond Photoconducting Dipole Antennas," *IEEE J. Quantum Electron.*, 1988, doi: 10.1109/3.121.

[21] C. Fattinger and D. Grischkowsky, "Point source terahertz optics," *Appl. Phys. Lett.*, 1988, doi: 10.1063/1.99971.

[22] M. van Exter and D. R. Grischkowsky, "Characterization of an Optoelectronic Terahertz Beam System," *IEEE Trans. Microw. Theory Tech.*, 1990, doi:

10.1109/22.60016.

[23] J. Neu and C. A. Schmuttenmaer, “Tutorial: An introduction to terahertz time domain spectroscopy (THz-TDS),” *J. Appl. Phys.*, 2018, doi: 10.1063/1.5047659.

[24] L. Thrane, R. H. Jacobsen, P. Uhd Jepsen, and S. R. Keiding, “THz reflection spectroscopy of liquid water,” *Chem. Phys. Lett.*, vol. 240, no. 4, pp. 330–333, 1995, doi: 10.1016/0009-2614(95)00543-D.

[25] A. Y. Pawar, D. D. Sonawane, K. B. Erande, and D. V. Derle, “Terahertz technology and its applications,” *Drug Invention Today*. 2013, doi: 10.1016/j.dit.2013.03.009.

[26] L. You and H. Liu, “A two-phase flow and transport model for the cathode of PEM fuel cells,” *Int. J. Heat Mass Transf.*, vol. 45, no. 11, pp. 2277–2287, 2002, doi: 10.1016/S0017-9310(01)00322-2.

[27] T. E. Springer, “Polymer Electrolyte Fuel Cell Model,” *J. Electrochem. Soc.*, vol. 138, no. 8, p. 2334, 1991, doi: 10.1149/1.2085971.

[28] S. H. Mirfarsi, M. J. Parnian, and S. Rowshanzamir, “Self-humidifying proton exchange membranes for fuel cell applications: Advances and challenges,” *Processes*, vol. 8, no. 9, 2020, doi: 10.3390/pr8091069.

[29] Z. Zheng, M. C. Péra, D. Hissel, M. Becherif, K. S. Agbli, and Y. Li, “A double-fuzzy diagnostic methodology dedicated to online fault diagnosis of proton exchange membrane fuel cell stacks,” *J. Power Sources*, vol. 271, pp. 570–581, 2014, doi: 10.1016/j.jpowsour.2014.07.157.

[30] J. St-Pierre, A. Wong, J. Diep, and D. Kiel, “Demonstration of a residence time distribution method for proton exchange membrane fuel cell evaluation,” *J. Power Sources*, vol. 164, no. 1, pp. 196–202, 2007, doi: 10.1016/j.jpowsour.2006.09.103.

[31] J. Diep, D. Kiel, J. St-Pierre, and A. Wong, “Development of a residence time distribution method for proton exchange membrane fuel cell evaluation,” *Chem. Eng. Sci.*, vol. 62, no. 3, pp. 846–857, 2006, doi: 10.1016/j.ces.2006.10.015.

[32] G. Hoogers, *Fuel cell technology handbook*. 2002.

[33] S. J. Peighambardoust, S. Rowshanzamir, and M. Amjadi, “Review of the proton exchange membranes for fuel cell applications,” in *International Journal of Hydrogen*

Energy, 2010, vol. 35, no. 17, pp. 9349–9384, doi: 10.1016/j.ijhydene.2010.05.017.

[34] R. W. Ramette, "Outmoded terminology: The normal hydrogen electrode," *J. Chem. Educ.*, vol. 64, no. 10, p. 885, 1987, doi: https://doi.org/10.1021/ed064p885.

[35] S. G. Bratsch, "Standard Electrode Potentials and Temperature Coefficients in Water at 298.15 K," *J. Phys. Chem. Ref. Data*, vol. 18, no. 1–21, 1989, doi: https://doi.org/10.1063/1.555839.

[36] U. R. Farooqui, A. L. Ahmad, and N. A. Hamid, "Graphene oxide: A promising membrane material for fuel cells," *Renew. Sustain. Energy Rev.*, vol. 82, no. July 2017, pp. 714–733, 2018, doi: 10.1016/j.rser.2017.09.081.

[37] B. Smitha, S. Sridhar, and A. A. Khan, "Solid polymer electrolyte membranes for fuel cell applications - A review," *J. Memb. Sci.*, vol. 259, no. 1–2, pp. 10–26, 2005, doi: 10.1016/j.memsci.2005.01.035.

[38] S. Litster and G. McLean, "PEM fuel cell electrodes," *Journal of Power Sources*, vol. 130, no. 1–2. pp. 61–76, 2004, doi: 10.1016/j.jpowsour.2003.12.055.

[39] P. R. Kumar, P. L. Suryawanshi, S. P. Gumfekar, B. A. Bhanvase, and S. Sonawane, "Sonochemical synthesis of Pt-Co/C electrocatalyst for PEM fuel cell applications," *Surfaces and Interfaces*, vol. 12, pp. 116–123, 2018, doi: 10.1016/j.surfin.2018.04.002.

[40] R. Othman, A. L. Dicks, and Z. Zhu, "Non precious metal catalysts for the PEM fuel cell cathode," *International Journal of Hydrogen Energy*, vol. 37, no. 1. pp. 357–372, 2012, doi: 10.1016/j.ijhydene.2011.08.095.

[41] P. J. Rheinländer, J. Herranz, J. Durst, and H. A. Gasteiger, "Kinetics of the Hydrogen Oxidation/Evolution Reaction on Polycrystalline Platinum in Alkaline Electrolyte Reaction Order with Respect to Hydrogen Pressure," *J. Electrochem. Soc.*, vol. 161, no. 14, pp. F1448–F1457, 2014, doi: 10.1149/2.0501414jes.

[42] F. T. Wagner, B. Lakshmanan, and M. F. Mathias, "Electrochemistry and the future of the automobile," *J. Phys. Chem. Lett.*, vol. 1, no. 14, pp. 2204–2219, 2010, doi: 10.1021/jz100553m.

[43] A. Jayakumar, S. P. Sethu, M. Ramos, J. Robertson, and A. Al-Jumaily, "A technical review on gas diffusion, mechanism and medium of PEM fuel cell," *Ionics*, vol. 21, no. 1. pp. 1–18, 2015, doi: 10.1007/s11581-014-1322-x.

[44] F. Barbir, “Main Cell Components, Material Properties, and Processes,” in *PEM Fuel Cells*, 2013, pp. 73–117.

[45] R. Omrani and B. Shabani, “Gas diffusion layer modifications and treatments for improving the performance of proton exchange membrane fuel cells and electrolysers: A review,” *Int. J. Hydrogen Energy*, vol. 42, no. 47, pp. 28515–28536, 2017, doi: 10.1016/j.ijhydene.2017.09.132.

[46] M. S. Ismail, K. J. Hughes, D. B. Ingham, L. Ma, and M. Pourkashanian, “Effect of PTFE loading of gas diffusion layers on the performance of proton exchange membrane fuel cells running at high-efficiency operating conditions,” *Int. J. Energy Res.*, vol. 37, no. 13, pp. 1592–1599, 2013, doi: 10.1002/er.2968.

[47] G. Velayutham, J. Kaushik, N. Rajalakshmi, and K. S. Dhathathreyan, “Effect of PTFE content in gas diffusion media and microlayer on the performance of PEMFC tested under ambient pressure,” *Fuel Cells*, 2007, doi: 10.1002/fuce.200600032.

[48] H. Li *et al.*, “A review of water flooding issues in the proton exchange membrane fuel cell,” *J. Power Sources*, vol. 178, no. 1, pp. 103–117, 2008, doi: 10.1016/j.jpowsour.2007.12.068.

[49] X. Xie, R. Wang, K. Jiao, G. Zhang, J. Zhou, and Q. Du, “Investigation of the effect of micro-porous layer on PEM fuel cell cold start operation,” *Renew. Energy*, vol. 117, pp. 125–134, 2018, doi: 10.1016/j.renene.2017.10.039.

[50] A. Hermann, T. Chaudhuri, and P. Spagnol, “Bipolar plates for PEM fuel cells: A review,” in *International Journal of Hydrogen Energy*, 2005, vol. 30, no. 12, pp. 1297–1302, doi: 10.1016/j.ijhydene.2005.04.016.

[51] S. Shimpalee *et al.*, “Investigation of bipolar plate materials for proton exchange membrane fuel cells,” *Int. J. Hydrogen Energy*, vol. 41, no. 31, pp. 13688–13696, 2016, doi: 10.1016/j.ijhydene.2016.05.163.

[52] A. Kumar and R. G. Reddy, “Materials and design development for bipolar/end plates in fuel cells,” in *Journal of Power Sources*, 2004, vol. 129, no. 1 SPEC. ISS., pp. 62–67, doi: 10.1016/j.jpowsour.2003.11.011.

[53] W. Dai *et al.*, “A review on water balance in the membrane electrode assembly of proton exchange membrane fuel cells,” *Int. J. Hydrog. Energy*, vol. 34, no. 23, pp.

9461–9478, 2009, doi: 10.1016/j.ijhydene.2009.09.017.

[54] K. Jiao and X. Li, “Water transport in polymer electrolyte membrane fuel cells,” *Prog. Energy Combust. Sci.*, vol. 37, no. 3, pp. 221–291, 2011, doi: 10.1016/j.pecs.2010.06.002.

[55] C. Spiegel, *Designing and Building Fuel Cells*. 2007.

[56] C. Spiegel, *PEM Fuel Cell Modeling and Simulation Using Matlab*. 2008.

[57] I. Pilatowsky, R. J. Romero, C. A. Isaza, S. A. Gamboa, P. J. Sebastian, and W. Rivera, “Cogeneration Fuel Cell - Sorption Air Conditioning Systems,” *Green Energy Technol.*, 2011, doi: 10.1007/978-1-84996-028-1.

[58] J. T. Gostick and A. Z. Weber, “Resistor-Network Modeling of Ionic Conduction in Polymer Electrolytes,” *Electrochim. Acta*, vol. 179, pp. 137–145, 2015, doi: 10.1016/j.electacta.2015.03.126.

[59] Y. Cai, T. Chen, T. Yang, and J. Xiao, “Mechanism of water transport in serpentine cathode channels of proton exchange membrane fuel cells,” *J. Power Sources*, vol. 209, pp. 90–104, 2012, doi: 10.1016/j.jpowsour.2012.02.095.

[60] M. Hu and G. Cao, “Research on the long-term stability of a PEMFC stack: Analysis of pinhole evolution,” *Int. J. Hydrogen Energy*, vol. 39, no. 15, pp. 7940–7954, 2014, doi: 10.1016/j.ijhydene.2014.03.072.

[61] B. Carnes and N. Djilali, “Analysis of coupled proton and water transport in a PEM fuel cell using the binary friction membrane model,” *Electrochim. Acta*, vol. 52, no. 3, pp. 1038–1052, 2006, doi: 10.1016/j.electacta.2006.07.006.

[62] P. A. García-Salaberri, D. G. Sánchez, P. Boillat, M. Vera, and K. A. Friedrich, “Hydration and dehydration cycles in polymer electrolyte fuel cells operated with wet anode and dry cathode feed: A neutron imaging and modeling study,” *J. Power Sources*, 2017, doi: 10.1016/j.jpowsour.2017.03.155.

[63] T. Geva, “Magnetic resonance imaging: Historical perspective,” *Journal of Cardiovascular Magnetic Resonance*. 2006, doi: 10.1080/10976640600755302.

[64] I. I. Rabi, J. R. Zacharias, S. Millman, and P. Kusch, “A new method of measuring nuclear magnetic moment,” *Physical Review*, vol. 53, no. 4. p. 318, 1938, doi:

10.1103/PhysRev.53.318.

[65] N. Dombey, “The Nobel prize in physics,” *Nature*, 1982, doi: 10.1038/300106a0.

[66] J. N. Dumez, “Spatial encoding and spatial selection methods in high-resolution NMR spectroscopy,” *Progress in Nuclear Magnetic Resonance Spectroscopy*. 2018, doi: 10.1016/j.pnmrs.2018.08.001.

[67] S. Tsushima, K. Teranishi, and S. Hirai, “Magnetic Resonance Imaging of the Water Distribution within a Polymer Electrolyte Membrane in Fuel Cells,” *Electrochem. Solid-State Lett.*, vol. 7, no. 9, p. A269, 2004, doi: 10.1149/1.1774971.

[68] K. W. Feindel, L. P. A. LaRocque, D. Starke, S. H. Bergens, and R. E. Wasylishen, “In situ observations of water production and distribution in an operating H2/O2 PEM fuel cell assembly using 1H NMR microscopy,” *J. Am. Chem. Soc.*, vol. 126, no. 37, pp. 11436–11437, 2004, doi: 10.1021/ja0461116.

[69] S. Tsushima, K. Teranishi, K. Nishida, and S. Hirai, “Water content distribution in a polymer electrolyte membrane for advanced fuel cell system with liquid water supply,” in *Magnetic Resonance Imaging*, 2005, vol. 23, no. 2 SPEC. ISS., pp. 255–258, doi: 10.1016/j.mri.2004.11.059.

[70] S. Tsushima, K. Teranishi, and S. Hirai, “Water diffusion measurement in fuel-cell SPE membrane by NMR,” in *Energy*, 2005, vol. 30, no. 2-4 SPEC. ISS., pp. 235–245, doi: 10.1016/j.energy.2004.04.013.

[71] S. Tsushima, S. Hirai, K. Kitamura, M. Yamashita, and S. Takase, “MRI application for clarifying fuel cell performance with variation of polymer electrolyte membranes: Comparison of water content of a hydrocarbon membrane and a perfluorinated membrane,” *Appl. Magn. Reson.*, vol. 32, no. 1–2, pp. 233–241, 2007, doi: 10.1007/s00723-007-0009-0.

[72] K. Teranishi, S. Tsushima, and S. Hirai, “Study of the effect of membrane thickness on the performance of polymer electrolyte fuel cells by water distribution in a membrane,” *Electrochem. Solid-State Lett.*, vol. 8, no. 6, 2005, doi: 10.1149/1.1897343.

[73] T. Kotaka, S. Tsushima, and S. Hirai, “Visualization of Membrane Hydration Path in an Operating PEMFC by Nuclei-Labeling MRI,” 2007, pp. 445–450, doi:

10.1149/1.2780958.

[74] “Investigation of Hydrogen Cross-leak Behaviors in a Polymer Electrolyte Membrane by Direct Gas Mass Spectroscopy and Magnetic Resonance Imaging,” *ECS Meet. Abstr.*, 2007, doi: 10.1149/ma2007-02/9/408.

[75] K. W. Feindel, S. H. Bergens, and R. E. Wasylishen, “Insights into the distribution of water in a self-humidifying H 2/O2 proton-exchange membrane fuel cell using 1H NMR microscopy,” *J. Am. Chem. Soc.*, 2006, doi: 10.1021/ja064389n.

[76] K. W. Feindel, S. H. Bergens, and R. E. Wasylishen, “The use of 1H NMR microscopy to study proton-exchange membrane fuel cells,” *ChemPhysChem*. 2006, doi: 10.1002/cphc.200500504.

[77] K. W. Feindel, S. H. Bergens, and R. E. Wasylishen, “The influence of membrane electrode assembly water content on the performance of a polymer electrolyte membrane fuel cell as investigated by 1H NMR microscopy,” *Phys. Chem. Chem. Phys.*, 2007, doi: 10.1039/b617551a.

[78] J. Bedet *et al.*, “Magnetic resonance imaging of water distribution and production in a 6 cm2 PEMFC under operation,” *Int. J. Hydrog. Energy*, vol. 33, no. 12, pp. 3146–3149, 2008, doi: 10.1016/j.ijhydene.2008.01.053.

[79] K. R. Minard, V. V. Viswanathan, P. D. Majors, L. Q. Wang, and P. C. Rieke, “Magnetic resonance imaging (MRI) of PEM dehydration and gas manifold flooding during continuous fuel cell operation,” *J. Power Sources*, vol. 161, no. 2, pp. 856–863, 2006, doi: 10.1016/j.jpowsour.2006.04.125.

[80] K. W. Feindel, S. H. Bergens, and R. E. Wasylishen, “Use of hydrogen-deuterium exchange for contrast in 1H NMR microscopy investigations of an operating PEM fuel cell,” *J. Power Sources*, 2007, doi: 10.1016/j.jpowsour.2007.04.079.

[81] N. Kardjilov, I. Manke, A. Hilger, M. Strobl, and J. Banhart, “Neutron imaging in materials science,” *Materials Today*. 2011, doi: 10.1016/S1369-7021(11)70139-0.

[82] O. Peter, “Neutronen-durchleuchtung,” *Zeitschrift fur Naturforsch. - Sect. A J. Phys. Sci.*, 1946, doi: 10.1515/zna-1946-1002.

[83] E. Lehmann, D. Mannes, A. Kaestner, and C. Grünzweig, “Recent Applications of Neutron Imaging Methods,” in *Physics Procedia*, 2017, vol. 88, no. September 2016,

pp. 5–12, doi: 10.1016/j.phpro.2017.06.055.

[84] R. J. Bellows, “Neutron Imaging Technique for In Situ Measurement of Water Transport Gradients within Nafion in Polymer Electrolyte Fuel Cells,” *J. Electrochem. Soc.*, vol. 146, no. 3, p. 1099, 1999, doi: 10.1149/1.1391727.

[85] A. B. Geiger, A. Tsukada, E. Lehmann, P. Vontobel, A. Wokaun, and G. G. Scherer, “In Situ Investigation of Two-Phase Flow Patterns in Flow Fields of PEFC’s Using Neutron Radiography,” *Fuel Cells*, 2002, doi: 10.1002/fuce.200290007.

[86] R. Satija, D. L. Jacobson, M. Arif, and S. A. Werner, “In situ neutron imaging technique for evaluation of water management systems in operating PEM fuel cells,” *J. Power Sources*, 2004, doi: 10.1016/j.jpowsour.2003.11.068.

[87] P. Boillat, E. H. Lehmann, P. Trtik, and M. Cochet, “Neutron imaging of fuel cells – Recent trends and future prospects,” *Curr. Opin. Electrochem.*, vol. 5, no. 1, pp. 3–10, 2017, doi: 10.1016/j.coelec.2017.07.012.

[88] D. Kramer *et al.*, “In situ diagnostic of two-phase flow phenomena in polymer electrolyte fuel cells by neutron imaging: Part A. Experimental, data treatment, and quantification,” *Electrochim. Acta*, 2005, doi: 10.1016/j.electacta.2004.11.005.

[89] K. Yoshizawa, K. Ikezoe, Y. Tasaki, D. Kramer, E. H. Lehmann, and G. G. Scherer, “Analysis of Gas Diffusion Layer and Flow-Field Design in a PEMFC Using Neutron Radiography,” *J. Electrochem. Soc.*, 2008, doi: 10.1149/1.2823003.

[90] J. P. Owejan, T. A. Trabold, D. L. Jacobson, D. R. Baker, D. S. Hussey, and M. Arif, “In situ investigation of water transport in an operating PEM fuel cell using neutron radiography: Part 2 - Transient water accumulation in an interdigitated cathode flow field,” *Int. J. Heat Mass Transf.*, 2006, doi: 10.1016/j.ijheatmasstransfer.2006.07.004.

[91] A. Turhan, K. Heller, J. S. Brenizer, and M. M. Mench, “Passive control of liquid water storage and distribution in a PEFC through flow-field design,” *J. Power Sources*, 2008, doi: 10.1016/j.jpowsour.2008.02.028.

[92] T. A. Trabold, J. P. Owejan, D. L. Jacobson, M. Arif, and P. R. Huffman, “In situ investigation of water transport in an operating PEM fuel cell using neutron radiography: Part 1 - Experimental method and serpentine flow field results,” *Int. J. Heat Mass Transf.*, 2006, doi: 10.1016/j.ijheatmasstransfer.2006.07.003.

[93] N. Pekula *et al.*, “Study of water distribution and transport in a polymer electrolyte fuel cell using neutron imaging,” *Nucl. Instrum. Methods Phys. Res. A*, vol. 542, no. 1–3, pp. 134–141, 2005, doi: 10.1016/j.nima.2005.01.090.

[94] A. Iranzo and P. Boillat, “Liquid water distribution patterns featuring back-diffusion transport in a PEM fuel cell with neutron imaging,” *Int. J. Hydrogen Energy*, 2014, doi: 10.1016/j.ijhydene.2014.08.042.

[95] J. P. Owejan, T. A. Trabold, D. L. Jacobson, M. Arif, and S. G. Kandlikar, “Effects of flow field and diffusion layer properties on water accumulation in a PEM fuel cell,” *Int. J. Hydrogen Energy*, 2007, doi: 10.1016/j.ijhydene.2007.05.044.

[96] Q. Meyer *et al.*, “Effect of gas diffusion layer properties on water distribution across air-cooled, open-cathode polymer electrolyte fuel cells: A combined ex-situ X-ray tomography and in-operando neutron imaging study,” *Electrochim. Acta*, 2016, doi: 10.1016/j.electacta.2016.06.068.

[97] E. Coz *et al.*, “Water management in a planar air-breathing fuel cell array using operando neutron imaging,” *J. Power Sources*, 2016, doi: 10.1016/j.jpowsour.2016.09.041.

[98] M. A. Hickner *et al.*, “Real-Time Imaging of Liquid Water in an Operating Proton Exchange Membrane Fuel Cell,” *J. Electrochem. Soc.*, vol. 153, no. 5, p. A902, 2006, doi: 10.1149/1.2184893.

[99] M. A. Hickner, N. P. Siegel, K. S. Chen, D. S. Hussey, and D. L. Jacobson, “Observations of Transient Flooding in a Proton Exchange Membrane Fuel Cell Using Time-Resolved Neutron Radiography,” *J. Electrochem. Soc.*, vol. 157, no. 1, p. B32, 2009, doi: 10.1149/1.3250864.

[100] S. Gößling *et al.*, “Analysis of liquid water formation in polymer electrolyte membrane (PEM) fuel cell flow fields with a dry cathode supply,” *J. Power Sources*, vol. 306, pp. 658–665, 2016, doi: 10.1016/j.jpowsour.2015.12.060.

[101] P. Boillat *et al.*, “Impact of Water on PEFC Performance Evaluated by Neutron Imaging Combined with Pulsed Helox Operation,” *J. Electrochem. Soc.*, 2012, doi: 10.1149/2.017207jes.

[102] J. Kätzel *et al.*, “Effect of ageing of gas diffusion layers on the water distribution in

flow field channels of polymer electrolyte membrane fuel cells," *J. Power Sources*, 2016, doi: 10.1016/j.jpowsour.2015.10.004.

[103] J. D. Fairweather *et al.*, "Effects of Cathode Corrosion on Through-Plane Water Transport in Proton Exchange Membrane Fuel Cells," *J. Electrochem. Soc.*, 2013, doi: 10.1149/2.024309jes.

[104] P. Boillat, G. Frei, E. H. Lehmann, G. G. Scherer, and A. Wokaun, "Neutron imaging resolution improvements optimized for fuel cell applications," *Electrochem. Solid-State Lett.*, vol. 13, no. 3, p. B25, 2010, doi: 10.1149/1.3279636.

[105] D. S. Hussey, J. M. LaManna, E. Baltic, and D. L. Jacobson, "Neutron Imaging Detector with Scintillation Light Magnification and Amplification," *ECS Trans.*, 2016, doi: 10.1149/07514.0245ecst.

[106] A. Heider, J. Sollinger, F. Abt, M. Boley, R. Weber, and T. Graf, "High-speed X-ray analysis of spatter formation in laser welding of copper," 2013, doi: 10.1016/j.phpro.2013.03.058.

[107] W. Visser *et al.*, "Automated comparison of X-ray images for cargo scanning," 2017, doi: 10.1109/CCST.2016.7815714.

[108] A. M. K. Thomas, "The first 50 years of military radiology 1895-1945," *Eur. J. Radiol.*, 2007, doi: 10.1016/j.ejrad.2007.05.024.

[109] O. Heid *et al.*, "Liquid jet target x-ray tube with field emission cathode," 2015, doi: 10.1117/12.2187036.

[110] I. Manke *et al.*, "Investigation of water evolution and transport in fuel cells with high resolution synchrotron x-ray radiography," *Appl. Phys. Lett.*, vol. 90, no. 17, p. 174105, 2007, doi: 10.1063/1.2731440.

[111] C. Hartnig, I. Manke, R. Kuhn, S. Kleinau, J. Goebbels, and J. Banhart, "High-resolution in-plane investigation of the water evolution and transport in PEM fuel cells," *J. Power Sources*, vol. 188, no. 2, pp. 468–474, 2009, doi: 10.1016/j.jpowsour.2008.12.023.

[112] P. Krüger *et al.*, "Synchrotron X-ray tomography for investigations of water distribution in polymer electrolyte membrane fuel cells," *J. Power Sources*, vol. 196, no. 12, pp. 5250–5255, 2011, doi: 10.1016/j.jpowsour.2010.09.042.

[113] T. Mukaide *et al.*, “In situ observation of water distribution and behaviour in a polymer electrolyte fuel cell by synchrotron X-ray imaging,” *J. Synchrotron Radiat.*, vol. 15, no. 4, pp. 329–334, 2008, doi: 10.1107/S0909049508006638.

[114] S. J. Lee, S. G. Kim, G. G. Park, and C. S. Kim, “Quantitative visualization of temporal water evolution in an operating polymer electrolyte fuel cell,” *Int. J. Hydrog. Energy*, vol. 35, no. 19, pp. 10457–10463, 2010, doi: 10.1016/j.ijhydene.2010.07.173.

[115] J. Lee *et al.*, “Synchrotron Investigation of Microporous Layer Thickness on Liquid Water Distribution in a PEM Fuel Cell,” *J. Electrochem. Soc.*, vol. 162, no. 7, pp. F669–F676, 2015, doi: 10.1149/2.0221507jes.

[116] M. M. Daino and S. G. Kandlikar, “Evaluation of Imaging Techniques Applied to Water Management Research in PEMFCs,” in *Proceedings of the 7th International Conference on Nanochannels, Microchannels, and Minichannels 2009, ICNMM2009*, 2010, no. January, pp. 467–479, doi: 10.1115/icnmm2009-82031.

[117] K. Tüber, D. Pócza, and C. Hebling, “Visualization of water buildup in the cathode of a transparent PEM fuel cell,” *J. Power Sources*, vol. 124, no. 2, pp. 403–414, 2003, doi: 10.1016/S0378-7753(03)00797-3.

[118] A. Hakenjos, H. Muenter, U. Wittstadt, and C. Hebling, “A PEM fuel cell for combined measurement of current and temperature distribution, and flow field flooding,” *J. Power Sources*, 2004, doi: 10.1016/j.jpowsour.2003.11.081.

[119] T. Murahashi, H. Kobayashi, and E. Nishiyama, “In situ visualization of water droplets in polymer electrolyte fuel cell cathode,” *Electrochemistry*, 2007, doi: 10.5796/electrochemistry.75.261.

[120] X. G. Yang, F. Y. Zhang, A. L. Lubawy, and C. Y. Wang, “Visualization of liquid water transport in a PEFC,” *Electrochem. Solid-State Lett.*, vol. 7, no. 11, p. A408, 2004, doi: 10.1149/1.1803051.

[121] J. Borrelli, T. Trabold, S. G. Kandlikar, and J. Owejan, “Water transport visualization and two-phase pressure drop measurements in a simulated PEMFC cathode minichannel,” 2005, doi: 10.1115/icmm2005-75118.

[122] K. Sugiura, M. Nakata, T. Yodo, Y. Nishiguchi, M. Yamauchi, and Y. Itoh, “Evaluation of a cathode gas channel with a water absorption layer/waste channel in a

PEFC by using visualization technique," *J. Power Sources*, 2005, doi: 10.1016/j.jpowsour.2005.02.037.

[123] S. Ge and C.-Y. Wang, "Liquid Water Formation and Transport in the PEFC Anode," *J. Electrochem. Soc.*, vol. 154, no. 10, p. B998, 2007, doi: 10.1149/1.2761830.

[124] Z. Liu, Z. Mao, and C. Wang, "A two dimensional partial flooding model for PEMFC," *J. Power Sources*, vol. 158, no. 2 SPEC. ISS., pp. 1229–1239, 2006, doi: 10.1016/j.jpowsour.2005.10.060.

[125] A. Theodorakakos, T. Ous, M. Gavaises, J. M. Nouri, N. Nikolopoulos, and H. Yanagihara, "Dynamics of water droplets detached from porous surfaces of relevance to PEM fuel cells," *J. Colloid Interface Sci.*, 2006, doi: 10.1016/j.jcis.2006.04.021.

[126] F. B. Weng, A. Su, C. Y. Hsu, and C. Y. Lee, "Study of water-flooding behaviour in cathode channel of a transparent proton-exchange membrane fuel cell," *J. Power Sources*, vol. 157, no. 2, pp. 674–680, 2006, doi: 10.1016/j.jpowsour.2006.01.002.

[127] D. Spernjak, A. K. Prasad, and S. G. Advani, "Experimental investigation of liquid water formation and transport in a transparent single-serpentine PEM fuel cell," *J. Power Sources*, vol. 170, no. 2, pp. 334–344, 2007, doi: 10.1016/j.jpowsour.2007.04.020.

[128] E. C. Kumbur, K. V. Sharp, and M. M. Mench, "Liquid droplet behavior and instability in a polymer electrolyte fuel cell flow channel," *J. Power Sources*, 2006, doi: 10.1016/j.jpowsour.2006.04.093.

[129] A. Bazylak, D. Sinton, and N. Djilali, "Dynamic water transport and droplet emergence in PEMFC gas diffusion layers," *J. Power Sources*, 2008, doi: 10.1016/j.jpowsour.2007.10.066.

[130] E. Kimball, T. Whitaker, Y. G. Kevrekidis, and J. B. Benziger, "Drops, slugs, and flooding in polymer electrolyte membrane fuel cells," *AIChE J.*, 2008, doi: 10.1002/aic.11464.

[131] B. Gao, T. S. Steenhuis, Y. Zevi, J. Y. Parlange, R. N. Carter, and T. A. Trabold, "Visualization of unstable water flow in a fuel cell gas diffusion layer," *J. Power Sources*, 2009, doi: 10.1016/j.jpowsour.2008.12.135.

[132] I. S. Hussaini and C. Y. Wang, "Visualization and quantification of cathode channel

flooding in PEM fuel cells," *J. Power Sources*, vol. 187, no. 2, pp. 444–451, 2009, doi: 10.1016/j.jpowsour.2008.11.030.

[133] S. Litster, D. Sinton, and N. Djilali, "Ex situ visualization of liquid water transport in PEM fuel cell gas diffusion layers," *J. Power Sources*, vol. 154, no. 1, pp. 95–105, 2006, doi: 10.1016/j.jpowsour.2005.03.199.

[134] A. Bazylak, D. Sinton, Z. S. Liu, and N. Djilali, "Effect of compression on liquid water transport and microstructure of PEMFC gas diffusion layers," *J. Power Sources*, vol. 163, no. 2, pp. 784–792, 2007, doi: 10.1016/j.jpowsour.2006.09.045.

[135] Y. Ishikawa, T. Morita, K. Nakata, K. Yoshida, and M. Shiozawa, "Behavior of water below the freezing point in PEFCs," *J. Power Sources*, vol. 163, no. 2, pp. 708–712, 2007, doi: 10.1016/j.jpowsour.2006.08.026.

[136] Y. Ishikawa, H. Hamada, M. Uehara, and M. Shiozawa, "Super-cooled water behavior inside polymer electrolyte fuel cell cross-section below freezing temperature," *J. Power Sources*, vol. 179, no. 2, pp. 547–552, 2008, doi: 10.1016/j.jpowsour.2008.01.031.

[137] R. Shimoi, M. Masuda, K. Fushinobu, Y. Kozawa, and K. Okazaki, "Visualization of the membrane temperature field of a polymer electrolyte fuel cell," *J. Energy Resour. Technol. Trans. ASME*, 2004, doi: 10.1115/1.1811119.

[138] I. H. Son, A. M. Lane, and D. T. Johnson, "The study of the deactivation of water-pretreated Pt/γ-Al 2O3 for low-temperature selective CO oxidation in hydrogen," *J. Power Sources*, 2003, doi: 10.1016/S0378-7753(03)00807-3.

[139] M. M. Daino, Z. Lu, J. M. LaManna, J. P. Owejan, T. A. Trabold, and S. G. Kandlikar, "Through-Plane Water Transport Visualization in a PEMFC by Visible and Infrared Imaging," *Electrochem. Solid-State Lett.*, vol. 14, no. 6, p. B51, 2011, doi: 10.1149/1.3560163.

[140] A. Chandan *et al.*, "High temperature (HT) polymer electrolyte membrane fuel cells (PEMFC)-A review," *Journal of Power Sources*. 2013, doi: 10.1016/j.jpowsour.2012.11.126.

[141] G. J. Wilmink and J. E. Grundt, "Invited review article: Current state of research on biological effects of terahertz radiation," 2011, doi: 10.1007/s10762-011-9794-5.

[142] W. Withayachumnankul and M. Naftaly, “Fundamentals of measurement in terahertz time-domain spectroscopy,” *Journal of Infrared, Millimeter, and Terahertz Waves*. 2014, doi: 10.1007/s10762-013-0042-z.

[143] C. Sirtori, “Bridge for the terahertz gap,” *Nature*, 2002, doi: 10.1038/417132b.

[144] B. Ferguson and X. C. Zhang, “Materials for terahertz science and technology,” *Nature Materials*. 2002, doi: 10.1038/nmat708.

[145] A. Ren *et al.*, “State-of-the-art in terahertz sensing for food and water security – A comprehensive review,” *Trends in Food Science and Technology*. 2019, doi: 10.1016/j.tifs.2019.01.019.

[146] T. H. Maiman, “Laser applications,” *Phys. Today*, 1967, doi: 10.1063/1.3034397.

[147] L. E. Hargrove, R. L. Fork, and M. A. Pollack, “Locking of hene laser modes induced by synchronous intracavity modulation,” *Appl. Phys. Lett.*, 1964, doi: 10.1063/1.1754025.

[148] A. Crocker, H. A. Gebbie, M. F. Kimmitt, and L. E. S. Mathias, “Stimulated emission in the far infra-red,” *Nature*, 1964, doi: 10.1038/201250a0.

[149] T. Y. Chang and T. J. Bridges, “Laser action at 452, 496, and 541 μm in optically pumped CH3F,” *Opt. Commun.*, 1970, doi: 10.1016/0030-4018(70)90169-0.

[150] K. H. Yang, P. L. Richards, and Y. R. Shen, “Generation of Far-infrared radiation by picosecond light pulses in LiNbO3,” *Appl. Phys. Lett.*, 1971, doi: 10.1063/1.1653935.

[151] Y. R. Shen, “Self-focusing: Experimental,” *Prog. Quantum Electron.*, vol. 4, no. PART 1, pp. 1–34, 1975, doi: 10.1016/0079-6727(75)90002-6.

[152] M. Naftaly, *Terahertz Metrology*. 2015.

[153] S. S. Dhillon *et al.*, “The 2017 terahertz science and technology roadmap,” *Journal of Physics D: Applied Physics*. 2017, doi: 10.1088/1361-6463/50/4/043001.

[154] J.-L. Coutaz, F. Garet, and V. P. Wallace, *Principles of Terahertz Time-Domain Spectroscopy*. 2018.

[155] C. Jansen *et al.*, “Terahertz imaging: applications and perspectives,” *Appl. Opt.*, vol. 49, no. 19, p. E48, 2010, doi: 10.1364/ao.49.000e48.

[156] N. Karpowicz, H. Zhong, J. Xu, K. I. Lin, J. S. Hwang, and X. C. Zhang, “Comparison between pulsed terahertz time-domain imaging and continuous wave terahertz imaging,” *Semicond. Sci. Technol.*, 2005, doi: 10.1088/0268-1242/20/7/021.

[157] R. Safian, G. Ghazi, and N. Mohammadian, “Review of photomixing continuous-wave terahertz systems and current application trends in terahertz domain,” *Opt. Eng.*, 2019, doi: 10.1117/1.oe.58.11.110901.

[158] D. H. Auston, “Picosecond optoelectronic switching and gating in silicon,” *Appl. Phys. Lett.*, vol. 26, no. 3, pp. 101–103, 1975, doi: 10.1063/1.88079.

[159] W. Withayachumnankul, B. M. Fischer, H. Lin, and D. Abbott, “Uncertainty in terahertz time-domain spectroscopy measurement,” *J. Opt. Soc. Am. B*, 2008, doi: 10.1364/josab.25.001059.

[160] M. Naftaly, N. Vieweg, and A. Deninger, “Industrial applications of terahertz sensing: State of play,” *Sensors (Switzerland)*. 2019, doi: 10.3390/s19194203.

[161] M. Wan, J. J. Healy, and J. T. Sheridan, “Terahertz phase imaging and biomedical applications,” *Optics and Laser Technology*. 2020, doi: 10.1016/j.optlastec.2019.105859.

[162] H. Lin *et al.*, “Measurement of the Intertablet Coating Uniformity of a Pharmaceutical Pan Coating Process With Combined Terahertz and Optical Coherence Tomography In-Line Sensing,” *J. Pharm. Sci.*, vol. 106, no. 4, pp. 1075–1084, 2017, doi: 10.1016/j.xphs.2016.12.012.

[163] J. Faist, F. Capasso, D. L. Sivco, C. Sirtori, A. L. Hutchinson, and A. Y. Cho, “Quantum cascade laser,” *Science (80-.).*, 1994, doi: 10.1126/science.264.5158.553.

[164] R. Paiella, “Intersubband Transitions In Quantum Structures,” *Intersubband Transitions Quantum Struct.*, 2006.

[165] R. F. Kazarinov and R. A. Suris, “Possibility of the amplification of electromagnetic waves in a semiconductor with a superlattice,” *Sov. Phys. Semicond*, 1971.

[166] R. Köhler *et al.*, “Terahertz semiconductor-heterostructure laser,” *Nature*, 2002, doi: 10.1038/417156a.

[167] T. Edwards, D. Walsh, M. Spurr, C. Rae, M. Dunn, and P. Browne, “Compact source

of continuously and widely-tunable terahertz radiation.," *Opt. Express*, 2006, doi: 10.1364/oe.14.001582.

[168] A. Maestrini *et al.*, "Schottky diode-based terahertz frequency multipliers and mixers," *Comptes Rendus Phys.*, 2010, doi: 10.1016/j.crhy.2010.05.002.

[169] A. . Fallis and S. A. Maas, *Nonlinear microwave and RF circuits*. 2003.

[170] W. W. Gray, L. Kikushima, R. J. Wagner, and N. P. Morenc, "Applying IMPATT Power Sources to Modern Microwave Systems," *IEEE J. Solid-State Circuits*, 1969, doi: 10.1109/JSSC.1969.1050046.

[171] A. Acharyya and J. P. Banerjee, "Prospects of IMPATT devices based on wide bandgap semiconductors as potential terahertz sources," *Appl. Nanosci.*, 2014, doi: 10.1007/s13204-012-0172-y.

[172] R. L. Bernick, "Millimeter-Wave CW IMPATT Diodes and Oscillators," *IEEE Trans. Microw. Theory Tech.*, 1979, doi: 10.1109/TMTT.1979.1129653.

[173] Q. Wu, T. D. Hewitt, and X. C. Zhang, "Two-dimensional electro-optic imaging of THz beams," *Appl. Phys. Lett.*, 1996, doi: 10.1063/1.116920.

[174] Z. Jiang and X.-C. Zhang, "Single-shot spatiotemporal terahertz field imaging," *Opt. Lett.*, 1998, doi: 10.1364/ol.23.001114.

[175] M. Usami, T. Iwamoto, R. Fukasawa, M. Tani, M. Watanabe, and K. Sakai, "Development of a THz spectroscopic imaging system," *Phys. Med. Biol.*, 2002, doi: 10.1088/0031-9155/47/21/311.

[176] A. Nahata, J. T. Yardley, and T. F. Heinz, "Two-dimensional imaging of continuous-wave terahertz radiation using electro-optic detection," *Appl. Phys. Lett.*, 2002, doi: 10.1063/1.1497190.

[177] A. W. Lee and Q. Hu, "Real-time, continuous-wave terahertz imaging by use of a microbolometer focal-plane array," *Opt. Lett.*, 2005, doi: 10.1364/ol.30.002563.

[178] H. Guerboukha, K. Nallappan, and M. Skorobogatiy, "Toward real-time terahertz imaging," *Adv. Opt. Photonics*, 2018, doi: 10.1364/aop.10.000843.

[179] R. Han *et al.*, "Active terahertz imaging using schottky diodes in CMOS: Array and 860-ghz pixel," *IEEE J. Solid-State Circuits*, 2013, doi: 10.1109/JSSC.2013.2269856.

[180] S.-P. Han *et al.*, “Real-time continuous-wave terahertz line scanner based on a compact 1 × 240 InGaAs Schottky barrier diode array detector,” *Opt. Express*, 2014, doi: 10.1364/oe.22.028977.

[181] E. Hack, L. Valzania, G. Gäumann, M. Shalaby, C. P. Hauri, and P. Zolliker, “Comparison of thermal detector arrays for off-axis THz holography and real-time THz imaging,” *Sensors (Switzerland)*, 2016, doi: 10.3390/s16020221.

[182] S.-H. Ding, Q. Li, Y.-D. Li, and Q. Wang, “Continuous-wave terahertz digital holography by use of a pyroelectric array camera,” *Opt. Lett.*, 2011, doi: 10.1364/ol.36.001993.

[183] Q. Li, S.-H. Ding, R. Yao, and Q. Wang, “Real-time terahertz scanning imaging by use of a pyroelectric array camera and image denoising,” *J. Opt. Soc. Am. A*, 2010, doi: 10.1364/josaa.27.002381.

[184] Y. Zhang, S. Hosono, N. Nagai, S. H. Song, and K. Hirakawa, “Fast and sensitive bolometric terahertz detection at room temperature through thermomechanical transduction,” *J. Appl. Phys.*, 2019, doi: 10.1063/1.5045256.

[185] G. C. Messina *et al.*, “High-TC Superconducting Kinetic Inductance Detectors for Terahertz Imaging,” 2019, doi: 10.1109/IRMMW-THz.2019.8874002.

[186] Y. H. Tao, A. J. Fitzgerald, and V. P. Wallace, “Non-contact, non-destructive testing in various industrial sectors with terahertz technology,” *Sensors*, vol. 20, no. 3. p. 712, 2020, doi: 10.3390/s20030712.

[187] V. Ryzhii and M. S. Shur, “Resonant terahertz detector utilizing plasma oscillations in two-dimensional electron system with lateral Schottky junction,” *Japanese J. Appl. Physics, Part 2 Lett.*, vol. 45, no. 42–45, 2006, doi: 10.1143/JJAP.45.L1118.

[188] V. M. Muravev and I. V. Kukushkin, “Plasmonic detector/spectrometer of subterahertz radiation based on two-dimensional electron system with embedded defect,” *Appl. Phys. Lett.*, 2012, doi: 10.1063/1.3688049.

[189] Y. C. Shen and P. F. Taday, “Development and application of terahertz pulsed imaging for nondestructive inspection of pharmaceutical tablet,” *IEEE J. Sel. Top. Quantum Electron.*, vol. 14, no. 2, pp. 407–415, 2008, doi: 10.1109/JSTQE.2007.911309.

[190] I. S. Russe, D. Brock, K. Knop, P. Kleinebudde, and J. A. Zeitler, “Validation of

terahertz coating thickness measurements using X-ray microtomography," *Mol. Pharm.*, vol. 9, no. 12, pp. 3551–3559, 2012, doi: 10.1021/mp300383y.

[191] A. J. Fitzgerald, B. E. Cole, and P. F. Taday, "Nondestructive analysis of tablet coating thicknesses using Terahertz pulsed imaging," *J. Pharm. Sci.*, vol. 94, no. 1, pp. 177–183, 2005, doi: 10.1002/jps.20225.

[192] J. A. Zeitler, Y. Shen, C. Baker, P. F. Taday, M. Pepper, and T. Rades, "Analysis of coating structures and interfaces in solid oral dosage forms by three dimensional terahertz pulsed imaging," *J. Pharm. Sci.*, vol. 96, no. 2, pp. 330–340, 2007, doi: 10.1002/jps.20789.

[193] J. A. Spencer *et al.*, "Delayed release tablet dissolution related to coating thickness by terahertz pulsed image mapping," *J. Pharm. Sci.*, vol. 97, no. 4, pp. 1543–1550, 2008, doi: 10.1002/jps.21051.

[194] L. Ho *et al.*, "Analysis of sustained-release tablet film coats using terahertz pulsed imaging," *J. Control. Release*, vol. 119, no. 3, pp. 253–261, 2007, doi: 10.1016/j.jconrel.2007.03.011.

[195] M. Niwa, Y. Hiraishi, N. Iwasaki, and K. Terada, "Quantitative analysis of the layer separation risk in bilayer tablets using terahertz pulsed imaging," *Int. J. Pharm.*, vol. 452, no. 1–2, pp. 249–256, 2013, doi: 10.1016/j.ijpharm.2013.05.010.

[196] W. Momose *et al.*, "Applying terahertz technology for nondestructive detection of crack initiation in a film-coated layer on a swelling tablet," *Results Pharma Sci.*, vol. 2, no. 1, pp. 29–37, 2012, doi: 10.1016/j.rinphs.2012.04.001.

[197] M. Niwa, Y. Hiraishi, and K. Terada, "Evaluation of coating properties of enteric-coated tablets using terahertz pulsed imaging," *Pharm. Res.*, vol. 31, no. 8, pp. 2140–2151, 2014, doi: 10.1007/s11095-014-1314-6.

[198] A. K. Vynckier *et al.*, "Calendering as a direct shaping tool for the continuous production of fixed-dose combination products via co-extrusion," *Eur. J. Pharm. Biopharm.*, vol. 96, pp. 125–131, 2015, doi: 10.1016/j.ejpb.2015.07.023.

[199] D. Alves-Lima *et al.*, "Review of terahertz pulsed imaging for pharmaceutical film coating analysis," *Sensors*, vol. 20, no. 5. p. 1441, 2020, doi: 10.3390/s20051441.

[200] J. Federici and L. Moeller, "Review of terahertz and subterahertz wireless

communications," *Journal of Applied Physics*. 2010, doi: 10.1063/1.3386413.

[201] L. Moeller, J. Federici, and K. Su, "2.5Gbit/s duobinary signalling with narrow bandwidth 0.625 terahertz source," *Electron. Lett.*, 2011, doi: 10.1049/el.2011.1451.

[202] S. Wietzke *et al.*, "Terahertz spectroscopy on polymers: A review of morphological studies," *J. Mol. Struct.*, vol. 1006, no. 1–3, pp. 41–51, 2011, doi: 10.1016/j.molstruc.2011.07.036.

[203] D. Banerjee, W. von Spiegel, M. D. Thomson, S. Schabel, and H. G. Roskos, "Diagnosing water content in paper by terahertz radiation," *Opt. Express*, 2008, doi: 10.1364/oe.16.009060.

[204] Y. Carts-Powell, "Terahertz imaging brings new capabilities to QC applications," *Laser Focus World*. 2005.

[205] P. Mousavi, F. Haran, D. Jez, F. Santosa, and J. S. Dodge, "Simultaneous composition and thickness measurement of paper using terahertz time-domain spectroscopy," *Appl. Opt.*, 2009, doi: 10.1364/AO.48.006541.

[206] T. Hattori, H. Kumon, and H. Tamazumi, "Terahertz spectroscopic characterization of paper," 2010, doi: 10.1109/ICIMW.2010.5612460.

[207] H. Merbold, D. J. H. C. Maas, and J. L. M. Van Mechelen, "Multiparameter sensing of paper sheets using terahertz time-domain spectroscopy: Caliper, fiber orientation, moisture, and the role of spatial inhomogeneity," 2017, doi: 10.1109/ICSENS.2016.7808683.

[208] J. L. M. van Mechelen, A. B. Kuzmenko, and H. Merbold, "Stratified dispersive model for material characterization using terahertz time-domain spectroscopy," *Opt. Lett.*, 2014, doi: 10.1364/ol.39.003853.

[209] J. L. M. Van Mechelen, D. J. H. C. Maas, and H. Merbold, "Paper sheet parameter determination using terahertz spectroscopy," 2016, doi: 10.1109/IRMMW-THz.2016.7758544.

[210] M. Fan, B. Cao, and G. Tian, "Enhanced Measurement of Paper Basis Weight Using Phase Shift in Terahertz Time-Domain Spectroscopy," *J. Sensors*, 2017, doi: 10.1155/2017/3520967.

[211] B. Khani, Y. Hu, V. Rymanov, C. Brenner, M. Hofmann, and A. Sto¨hr, “Compact optoelectronic continuous wave terahertz spectroscopy system (230-400 GHz) for paper sorting and characterization,” 2017, doi: 10.1109/cleoe-eqec.2017.8086453.

[212] V. Vassilev, B. Stoew, J. Blomgren, and G. Andersson, “A mm-Wave Sensor for Remote Measurement of Moisture in Thin Paper Layers,” *IEEE Trans. Terahertz Sci. Technol.*, 2015, doi: 10.1109/TTHZ.2015.2462716.

[213] T. Inagaki, I. D. Hartley, S. Tsuchikawa, and M. Reid, “Prediction of oven-dry density of wood by time-domain terahertz spectroscopy,” *Holzforschung*, 2014, doi: 10.1515/hf-2013-0013.

[214] T. Inagaki, B. Ahmed, I. D. Hartley, S. Tsuchikawa, and M. Reid, “Simultaneous prediction of density and moisture content of wood by terahertz time domain spectroscopy,” *J. Infrared, Millimeter, Terahertz Waves*, 2014, doi: 10.1007/s10762-014-0095-7.

[215] Y. Oyama, L. Zhen, T. Tanabe, and M. Kagaya, “Sub-terahertz imaging of defects in building blocks,” *NDT E Int.*, vol. 42, no. 1, pp. 28–33, 2009, doi: 10.1016/j.ndteint.2008.08.002.

[216] M. Reid and R. Fedosejevs, “Terahertz birefringence and attenuation properties of wood and paper,” *Appl. Opt.*, vol. 45, no. 12, pp. 2766–2772, 2006, doi: 10.1364/AO.45.002766.

[217] T. M. Todoruk, I. D. Hartley, and M. E. Reid, “Origin of birefringence in wood at terahertz frequencies,” in *IEEE Transactions on Terahertz Science and Technology*, 2012, vol. 2, no. 1, pp. 123–130, doi: 10.1109/TTHZ.2011.2177692.

[218] M. E. Reid, I. D. Hartley, and T. M. Todoruk, “Terahertz applications in the wood products industry,” in *Handbook of Terahertz Technology for Imaging, Sensing and Communications*, 2013, pp. 547–578.

[219] K. Krügener, E.-M. Stübling, R. Jachim, B. Kietz, M. Koch, and W. Viöl, “THz tomography for detecting damages on wood caused by insects,” *Appl. Opt.*, vol. 58, no. 22, p. 6063, 2019, doi: 10.1364/ao.58.006063.

[220] M. Koch, S. Hunsche, P. Schuacher, M. C. Nuss, J. Feldmann, and J. Fromm, “THz-imaging: A new method for density mapping of wood,” *Wood Sci. Technol.*, 1998, doi:

10.1007/BF00702799.

[221] Y. Fujii *et al.*, “Nondestructive detection of termites using a millimeter-wave imaging technique,” *For. Prod. J.*, 2007.

[222] Y. Fujii *et al.*, “Feasibility of millimeter wave imaging as tool for nondestructive inspection of wood and wooden structures,” 2010, doi: 10.1109/ICIMW.2010.5612351.

[223] S. Signorelli, F. J. Corpas, O. Borsani, J. B. Barroso, and J. Monza, “Water stress induces a differential and spatially distributed nitro-oxidative stress response in roots and leaves of Lotus japonicus,” *Plant Sci.*, vol. 201–202, no. 1, pp. 137–146, 2013, doi: 10.1016/j.plantsci.2012.12.004.

[224] M. J. Gómez-Bellot, P. A. Nortes, M. F. Ortuño, C. Romero, N. Fernández-García, and M. J. Sánchez-Blanco, “Influence of arbuscular mycorrhizal fungi and treated wastewater on water relations and leaf structure alterations of Viburnum tinus L. plants during both saline and recovery periods,” *J. Plant Physiol.*, vol. 188, pp. 96–105, 2015, doi: 10.1016/j.jplph.2015.09.007.

[225] D. Ferrante, G. E. Oliva, and R. J. Fernández, “Soil water dynamics, root systems, and plant responses in a semiarid grassland of Southern Patagonia,” *J. Arid Environ.*, vol. 104, pp. 52–58, 2014, doi: 10.1016/j.jaridenv.2014.01.009.

[226] S. Hadjiloucas, L. S. Karatzas, and J. W. Bowen, “Measurements of leaf water content using terahertz radiation,” *IEEE Trans. Microw. Theory Tech.*, vol. 47, no. 2, pp. 142–149, 1999, doi: 10.1109/22.744288.

[227] P. U. Jepsen, D. G. Cooke, and M. Koch, “Terahertz spectroscopy and imaging - Modern techniques and applications,” *Laser Photonics Rev.*, vol. 5, no. 1, pp. 124–166, 2011, doi: 10.1002/lpor.201000011.

[228] U. Siciliani de Cumis *et al.*, “Terahertz confocal microscopy with a quantum cascade laser source,” *Opt. Express*, vol. 20, no. 20, p. 21924, 2012, doi: 10.1364/oe.20.021924.

[229] L. Baldacci *et al.*, “Non-invasive absolute measurement of leaf water content using terahertz quantum cascade lasers,” *Plant Methods*, vol. 13, no. 1, 2017, doi: 10.1186/s13007-017-0197-z.

[230] G. M. Hale and M. R. Querry, “Optical Constants of Water in the 200-nm to 200-µm Wavelength Region,” *Appl. Opt.*, vol. 12, no. 3, p. 555, 1973, doi: 10.1364/ao.12.000555.

[231] R. Gente and M. Koch, “Monitoring leaf water content with THz and sub-THz waves,” *Plant Methods*, vol. 11, no. 1. 2015, doi: 10.1186/s13007-015-0057-7.

[232] C. Jördens, M. Scheller, B. Breitenstein, D. Selmar, and M. Koch, “Evaluation of leaf water status by means of permittivity at terahertz frequencies,” *J. Biol. Phys.*, vol. 35, no. 3, pp. 255–264, 2009, doi: 10.1007/s10867-009-9161-0.

[233] A. Zahid *et al.*, “Characterization and water content estimation method of living plant leaves using terahertz waves,” *Appl. Sci.*, vol. 9, no. 14, 2019, doi: 10.3390/app9142781.

[234] P. Nie *et al.*, “Detection of water content in rapeseed leaves using terahertz spectroscopy,” *Sensors (Switzerland)*, vol. 17, no. 12, 2017, doi: 10.3390/s17122830.

[235] K. Smart *et al.*, “A practical and portable solids-state electronic terahertz imaging system,” *Sensors (Switzerland)*, vol. 16, no. 4, 2016, doi: 10.3390/s16040579.

[236] E. Castro-Camus, M. Palomar, and A. A. Covarrubias, “Leaf water dynamics of Arabidopsis thaliana monitored in-vivo using terahertz time-domain spectroscopy,” *Sci. Rep.*, vol. 3, 2013, doi: 10.1038/srep02910.

[237] L. G. Santesteban, I. Palacios, C. Miranda, J. C. Iriarte, J. B. Royo, and R. Gonzalo, “Terahertz time domain spectroscopy allows contactless monitoring of grapevine water status,” *Front. Plant Sci.*, vol. 6, no. June, 2015, doi: 10.3389/fpls.2015.00404.

[238] N. Born *et al.*, “Monitoring plant drought stress response using terahertz time-domain spectroscopy,” *Plant Physiol.*, vol. 164, no. 4, pp. 1571–1577, 2014, doi: 10.1104/pp.113.233601.

[239] M. R. Mobasheri and S. B. Fatemi, “Leaf Equivalent Water Thickness assessment using reflectance at optimum wavelengths,” *Theor. Exp. Plant Physiol.*, vol. 25, no. 3, pp. 196–202, 2013, doi: 10.1590/s2197-00252013005000001.

[240] M. Möller *et al.*, “Use of thermal and visible imagery for estimating crop water status of irrigated grapevine,” *J. Exp. Bot.*, vol. 58, no. 4, pp. 827–838, 2007, doi: 10.1093/jxb/erl115.

[241] Y. Ge, G. Bai, V. Stoerger, and J. C. Schnable, “Temporal dynamics of maize plant growth, water use, and leaf water content using automated high throughput RGB and hyperspectral imaging,” *Comput. Electron. Agric.*, vol. 127, pp. 625–632, 2016, doi: 10.1016/j.compag.2016.07.028.

[242] C. T. Nemes, J. R. Swierk, and C. A. Schmuttenmaer, “A Terahertz-Transparent Electrochemical Cell for in Situ Terahertz Spectroelectrochemistry,” *Anal. Chem.*, vol. 90, no. 7, pp. 4389–4396, 2018, doi: 10.1021/acs.analchem.7b04204.

[243] W. Kaim and J. Fiedler, “Spectroelectrochemistry: The best of two worlds,” *Chem. Soc. Rev.*, vol. 38, no. 12, pp. 3373–3382, 2009, doi: 10.1039/b504286k.

[244] S. O. Yurchenko and K. I. Zaytsev, “Spectroscopy of nafion in terahertz frequency range,” *J. Appl. Phys.*, vol. 116, no. 11, p. 113508, 2014, doi: 10.1063/1.4896194.

[245] S. Ray, J. Dash, K. Nallappan, S. Meenakshi, S. D. Bhat, and B. Pesala, “Comparative study of water absorption and retention of nafion and its hybrid polymer electrolytic membranes using terahertz spectroscopy,” 2013, doi: 10.1109/IRMMW-THz.2013.6665680.

[246] S. Ray, N. Devi, J. Dash, G. Rambabu, S. D. Bhat, and B. Pesala, “Enhancement of water retention in UV-exposed fuel-cell proton exchange membranes studied using terahertz spectroscopy,” in *Terahertz, RF, Millimeter, and Submillimeter-Wave Technology and Applications IX*, 2016, vol. 9747, p. 97470P, doi: 10.1117/12.2212388.

[247] N. Devi, S. Ray, A. Shukla, S. D. Bhat, and B. Pesala, “Non-invasive macroscopic and molecular quantification of water in Nafion® and SPEEK Proton Exchange Membranes using terahertz spectroscopy,” *J. Memb. Sci.*, vol. 588, p. 117183, 2019, doi: 10.1016/j.memsci.2019.117183.

[248] N. Devi, S. Ray, A. Shukla, S. D. Bhat, and B. Pesala, “Tracking the hydration dynamics of Nafion fuel cell membranes using terahertz spectroscopy,” in *Proc. of SPIE Vol. 10917*, 2019, p. 64, doi: 10.1117/12.2511029.

[249] T. Hagiwara, T. Kusaka, T. Kiwa, K. Sakai, and K. Tsukada, “Visualization of the catalytic reactions in the fuel cells using THz chemical microscope,” in *International Conference on Infrared, Millimeter, and Terahertz Waves, IRMMW-THz*, 2013, vol. 2,

pp. 2–3, doi: 10.1109/IRMMW-THz.2013.6665916.

[250] P. Buaphad, P. Thamboon, N. Kangrang, M. W. Rhodes, and C. Thongbai, “Femtoelectron-Based Terahertz Imaging of Hydration State in a Proton Exchange Membrane Fuel Cell,” *J. Infrared, Millimeter, Terahertz Waves*, vol. 36, no. 8, pp. 745–755, 2015, doi: 10.1007/s10762-015-0166-4.

[251] P. Thamboon *et al.*, “Investigation of water distribution in proton exchange membrane fuel cells via Terahertz imaging,” *Nucl. Instruments Methods Phys. Res. Sect. A Accel. Spectrometers, Detect. Assoc. Equip.*, vol. 637, no. 1, pp. S161–S164, 2011, doi: 10.1016/j.nima.2010.02.047.

[252] M. A. Hickner, N. P. Siegel, K. S. Chen, D. S. Hussey, D. L. Jacobson, and M. Arif, “Understanding Liquid Water Distribution and Removal Phenomena in an Operating PEMFC via Neutron Radiography,” *J. Electrochem. Soc.*, vol. 155, no. 3, p. B294, 2008, doi: 10.1149/1.2825298.

[253] W. Acree Jr. and J. S. Chickos, “Phase Transition Enthalpy Measurements of Organic and Organometallic Compounds and Ionic Liquids. Sublimation, Vaporization and Fusion Enthalpies from 1880 to 2015. Part 2. C11-C192,” *J. Phys. Chem. Ref. Data*, vol. 45, p. 033101, 2017.

[254] S. Pujiastuti and H. Onggo, “Effect of various concentration of sulfuric acid for Nafion membrane activation on the performance of fuel cell,” *AIP Conf. Proc.*, vol. 1711, no. February 2016, 2016, doi: 10.1063/1.4941639.

[255] A. P. Manso, F. F. Marzo, J. Barranco, X. Garikano, and M. Garmendia Mujika, “Influence of geometric parameters of the flow fields on the performance of a PEM fuel cell. A review,” *Int. J. of Hydrog. Energy*, vol. 37, no. 20. pp. 15256–15287, 2012, doi: 10.1016/j.ijhydene.2012.07.076.

[256] M. Mortazavi and K. Tajiri, “Two-phase flow pressure drop in flow channels of proton exchange membrane fuel cells: Review of experimental approaches,” *Renew. Sustain. Energy Rev.*, vol. 45. pp. 296–317, 2015, doi: 10.1016/j.rser.2015.01.044.

[257] A. Iranzo, P. Boillat, J. Biesdorf, and A. Salva, “Investigation of the liquid water distributions in a 50cm2 PEM fuel cell: Effects of reactants relative humidity, current density, and cathode stoichiometry,” *Energy*, vol. 82, pp. 914–921, 2015, doi:

10.1016/j.energy.2015.01.101.

[258] J. Kang and J. Kim, “Membrane electrode assembly degradation by dry/wet gas on a PEM fuel cell,” *Int. J. Hydrogen Energy*, vol. 35, no. 23, pp. 13125–13130, 2010, doi: 10.1016/j.ijhydene.2010.04.077.

[259] M. Naftaly and R. E. Miles, “Terahertz time-domain spectroscopy for material characterization,” 2007, doi: 10.1109/JPROC.2007.898835.

[260] H. Kita, K. Okamoto, and S. Mukai, “Dielectric properties of polymers containing dispersed TCNQ salts,” *J. Appl. Polym. Sci.*, vol. 31, no. 5, pp. 1383–1392, 1986, doi: 10.1002/app.1986.070310522.

[261] Q. Duan, H. Wang, and J. Benziger, “Transport of liquid water through Nafion membranes,” *J. Memb. Sci.*, vol. 392–393, pp. 88–94, 2012, doi: 10.1016/j.memsci.2011.12.004.

[262] J. T. Hinatsu, “Water Uptake of Perfluorosulfonic Acid Membranes from Liquid Water and Water Vapor,” *J. Electrochem. Soc.*, vol. 141, no. 6, p. 1493, 2006, doi: 10.1149/1.2054951.

[263] C. B. Reid, E. Pickwell-Macpherson, J. G. Laufer, A. P. Gibson, J. C. Hebden, and V. P. Wallace, “Accuracy and resolution of THz reflection spectroscopy for medical imaging,” *Phys. Med. Biol.*, vol. 55, no. 16, pp. 4825–4838, 2010, doi: 10.1088/0031-9155/55/16/013.

[264] J. Xu, K. W. Plaxco, and S. J. Allen, “Absorption spectra of liquid water and aqueous buffers between 0.3 and 3. 72 THz,” *J. Chem. Phys.*, vol. 124, no. 3, 2006, doi: 10.1063/1.2151267.

[265] J. T. Kindt and C. A. Schmuttenmaer, “ Far-Infrared Dielectric Properties of Polar Liquids Probed by Femtosecond Terahertz Pulse Spectroscopy † ,” *J. Phys. Chem.*, vol. 100, no. 24, pp. 10373–10379, 2002, doi: 10.1021/jp960141g.

[266] J. E. Bertie and Z. Lan, “Infrared intensities of liquids XX: The intensity of the OH stretching band of liquid water revisited, and the best current values of the optical constants of H2O(1) at 25 °C between 15,000 and 1 cm-1,” *Appl. Spectrosc.*, vol. 50, no. 8, pp. 1047–1057, 1996, doi: 10.1366/0003702963905385.

[267] D. F. Alves-Lima, R. Letizia, R. Degl’Innocenti, R. Dawson, and H. Lin, “Quantitative

video-rate hydration imaging of Nafion proton exchange membranes with terahertz radiation," *J. Power Sources*, vol. 450, p. 227665, 2020, doi: 10.1016/j.jpowsour.2019.227665.

[268] C. Yin *et al.*, "Thermal annealing on free volumes, crystallinity and proton conductivity of Nafion membranes," *J. Phys. Chem. Solids*, vol. 120, pp. 71–78, 2018, doi: 10.1016/j.jpcs.2018.04.028.

[269] W. H. J. Hogarth and J. B. Benziger, "Operation of polymer electrolyte membrane fuel cells with dry feeds: Design and operating strategies," *J. Power Sources*, vol. 159, no. 2, pp. 968–978, 2006, doi: 10.1016/j.jpowsour.2005.11.079.

[270] D. J. Burnett, A. R. Garcia, and F. Thielmann, "Measuring moisture sorption and diffusion kinetics on proton exchange membranes using a gravimetric vapor sorption apparatus," *J. Power Sources*, 2006, doi: 10.1016/j.jpowsour.2005.12.096.

[271] P. Krtil, A. Trojánek, and Z. Samec, "Kinetics of water sorption in nafionthin films - Quartz crystal microbalance study," *J. Phys. Chem. B*, 2001, doi: 10.1021/jp004162t.

[272] F. M. Collette, C. Lorentz, G. Gebel, and F. Thominette, "Hygrothermal aging of Nafion®," *J. Memb. Sci.*, 2009, doi: 10.1016/j.memsci.2008.11.048.

[273] P. Huguet, A. Morin, G. Gebel, S. Deabate, A. K. Sutor, and Z. Peng, "In situ analysis of water management in operating fuel cells by confocal Raman spectroscopy," *Electrochem. commun.*, 2011, doi: 10.1016/j.elecom.2011.02.008.

[274] S. Deabate, R. Fatnassi, P. Sistat, and P. Huguet, "In situ confocal-Raman measurement of water and methanol concentration profiles in Nafion® membrane under cross-transport conditions," *J. Power Sources*, 2008, doi: 10.1016/j.jpowsour.2007.10.044.

[275] B. Legros, P.-X. Thivel, Y. Bultel, M. Boinet, and R. P. Nogueira, "Electrochemical Impedance and Acoustic Emission Survey of Water Desorption in Nafion Membranes," *Electrochem. Solid-State Lett.*, vol. 12, no. 7, p. B116, 2009, doi: 10.1149/1.3131728.

[276] Y. Tabuchi, R. Ito, S. Tsushima, and S. Hirai, "Analysis of in situ water transport in Nafion® by confocal micro-Raman spectroscopy," *J. Power Sources*, 2011, doi: 10.1016/j.jpowsour.2010.07.078.

[277] D. R. Morris and X. Sun, “Water-sorption and transport properties of Nafion 117 H,” *J. Appl. Polym. Sci.*, 1993, doi: 10.1002/app.1993.070500816.

[278] D. Rivin, C. E. Kendrick, P. W. Gibson, and N. S. Schneider, “Solubility and transport behavior of water and alcohols in Nafion^{TM},” *Polymer (Guildf).*, 2001, doi: 10.1016/S0032-3861(00)00350-5.

[279] T. Takamatsu, M. Hashiyama, and A. Eisenberg, “Sorption phenomena in nafion membranes,” *J. Appl. Polym. Sci.*, 1979, doi: 10.1002/app.1979.070241101.

[280] C. Tsonos, L. Apekis, and P. Pissis, “Water sorption and dielectric relaxation spectroscopy studies in hydrated Nafion (-SO3K) membranes,” *J. Mater. Sci.*, vol. 35, no. 23, pp. 5957–5965, 2000, doi: 10.1023/A:1026782509106.

[281] S. C. Yeo and A. Eisenberg, “Physical properties and supermolecular structure of perfluorinated ion-containing (nafion) polymers,” *J. Appl. Polym. Sci.*, 1977, doi: 10.1002/app.1977.070210401.

[282] P. W. Majsztrik, M. B. Satterfield, A. B. Bocarsly, and J. B. Benziger, “Water sorption, desorption and transport in Nafion membranes,” *J. Memb. Sci.*, vol. 301, no. 1–2, pp. 93–106, 2007, doi: 10.1016/j.memsci.2007.06.022.

[283] M. B. Satterfleld and J. B. Benziger, “Non-Fickian water vapor sorption dynamics by nafion membranes,” *J. Phys. Chem. B*, vol. 112, no. 12, pp. 3693–3704, 2008, doi: 10.1021/jp7103243.

[284] B. Mecheri, V. Felice, Z. Zhang, A. D’Epifanio, S. Licoccia, and A. C. Tavares, “DSC and DVS investigation of water mobility in Nafion/zeolite composite membranes for fuel cell applications,” *J. Phys. Chem. C*, 2012, doi: 10.1021/jp301762h.

[285] W. F. G. Saleha, R. Ramesh, N. Nalajala, A. Chakraborty, B. P. Ladewig, and M. Neergat, “Broadband dielectric spectroscopy of Nafion-117, sulfonated polysulfone (sPSF) and sulfonated polyether ketone (sPEK) membranes,” *J. Appl. Polym. Sci.*, vol. 134, no. 18, pp. 1–12, 2017, doi: 10.1002/app.44790.

[286] Z. Lu, G. Polizos, D. D. Macdonald, and E. Manias, “State of Water in Perfluorosulfonic Ionomer (Nafion 117) Proton Exchange Membranes,” *J. Electrochem. Soc.*, vol. 155, no. 2, p. B163, 2008, doi: 10.1149/1.2815444.

[287] K. Schmidt-Rohr and Q. Chen, “Parallel cylindrical water nanochannels in Nafion

fuel-cell membranes," *Nat. Mater.*, vol. 7, no. 1, pp. 75–83, 2008, doi: 10.1038/nmat2074.

[288] J. Peron *et al.*, "Properties of Nafion ® NR-211 membranes for PEMFCs," *J. Memb. Sci.*, vol. 356, no. 1–2, pp. 44–51, 2010, doi: 10.1016/j.memsci.2010.03.025.

[289] H. Zhang *et al.*, "Non-destructive Investigation of Paintings on Canvas by Continuous Wave Terahertz Imaging and Flash Thermography," *J. Nondestruct. Eval.*, vol. 36, no. 2, 2017, doi: 10.1007/s10921-017-0414-8.

[290] A. Orfanidi, P. Madkikar, H. A. El-Sayed, G. S. Harzer, T. Kratky, and H. A. Gasteiger, "The key to high performance low pt loaded electrodes," *J. Electrochem. Soc.*, 2017, doi: 10.1149/2.1621704jes.

[291] V. Yarlagadda *et al.*, "Boosting Fuel Cell Performance with Accessible Carbon Mesopores," *ACS Energy Letters*. 2018, doi: 10.1021/acsenergylett.8b00186.

[292] D. Cha, S. W. Jeon, W. Yang, D. Kim, and Y. Kim, "Comparative performance evaluation of self-humidifying PEMFCs with short-side-chain and long-side-chain membranes under various operating conditions," *Energy*, vol. 150, pp. 320–328, 2018, doi: 10.1016/j.energy.2018.02.133.

[293] F. Trombetta, D. W. Lima, F. Fiegenbaum, M. R. Becker, M. O. de Souza, and E. M. A. Martini, "C 16 MI.OTf ionic liquid on Pt/C and PtMo/C anodes improves the PEMFC performance," *Int. J. Hydrogen Energy*, vol. 43, no. 14, pp. 6945–6953, 2018, doi: 10.1016/j.ijhydene.2018.02.104.

[294] L. A. King *et al.*, "Non-precious metal hydrogen catalyst in commercial polymer electrolyte membrane electrolysers," *Nat. Nanotechnol.*, vol. Accepted, no. November, 2019, doi: 10.1038/s41565-019-0550-7.

[295] Y. Lee *et al.*, "Nafion membranes with a sulfonated organic additive for the use in vanadium redox flow batteries," *J. Appl. Polym. Sci.*, vol. 136, no. 21, pp. 8–13, 2019, doi: 10.1002/app.47547.

[296] R. Anderson, L. Zhang, Y. Ding, M. Blanco, X. Bi, and D. P. Wilkinson, "A critical review of two-phase flow in gas flow channels of proton exchange membrane fuel cells," *J. Power Sources*, vol. 195, no. 15, pp. 4531–4553, 2010, doi: 10.1016/j.jpowsour.2009.12.123.

[297] R. M. Aslam, D. B. Ingham, M. S. Ismail, K. J. Hughes, L. Ma, and M. Pourkashanian, “Simultaneous direct visualisation of liquid water in the cathode and anode serpentine flow channels of proton exchange membrane (PEM) fuel cells,” *J. Energy Inst.*, vol. 91, no. 6, pp. 1057–1070, 2018, doi: 10.1016/j.joei.2017.07.003.

[298] M. Yamauchi, K. Sugiura, T. Yamauchi, T. Taniguchi, and Y. Itoh, “Proposal for an optimum water management method using two-pole simultaneous measurement,” *J. Power Sources*, vol. 193, no. 1, pp. 1–8, 2009, doi: 10.1016/j.jpowsour.2009.02.078.

[299] O. A. Obeisun *et al.*, “Development of open-cathode polymer electrolyte fuel cells using printed circuit board flow-field plates: Flow geometry characterisation,” *Int. J. Hydrog. Energy*, vol. 39, no. 32, pp. 18326–18336, 2014, doi: 10.1016/j.ijhydene.2014.08.106.

[300] T. Ous and C. Arcoumanis, “Visualisation of water droplets during the operation of PEM fuel cells,” *J. Power Sources*, vol. 173, no. 1, pp. 137–148, 2007, doi: 10.1016/j.jpowsour.2007.04.075.

[301] F. Jaouen, D. Jones, N. Coutard, V. Artero, P. Strasser, and A. Kucernak, “Toward platinum group metal-free catalysts for hydrogen/air proton-exchange membrane fuel cells,” *Johnson Matthey Technol. Rev.*, vol. 62, no. 2, pp. 231–255, 2018, doi: 10.1595/205651318X696828.

[302] X. D. Wang, W. M. Yan, Y. Y. Duan, F. B. Weng, G. Bin Jung, and C. Y. Lee, “Numerical study on channel size effect for proton exchange membrane fuel cell with serpentine flow field,” *Energy Convers. Manag.*, vol. 51, no. 5, pp. 959–968, 2010, doi: 10.1016/j.enconman.2009.11.037.

[303] S. Xing, C. Zhao, W. Liu, J. Zou, M. Chen, and H. Wang, “Effects of bolt torque and gasket geometric parameters on open-cathode polymer electrolyte fuel cells,” *Appl. Energy*, vol. 303, no. April, p. 117632, 2021, doi: 10.1016/j.apenergy.2021.117632.

[304] E. S. Denisov, Y. K. Evdokimov, S. Martemianov, A. Thomas, and N. Adiutantov, “Electrochemical Noise as a Diagnostic Tool for PEMFC,” *Fuel Cells*, vol. 17, no. 2, pp. 225–237, 2017, doi: 10.1002/fuce.201600077.

[305] S. Kundu, L. C. Simon, M. Fowler, and S. Grot, “Mechanical properties of Nafion^{TM} electrolyte membranes under hydrated conditions,” *Polymer*, vol. 46, no. 25. pp.

11707–11715, 2005, doi: 10.1016/j.polymer.2005.09.059.

[306] Y. Tang, A. M. Karlsson, M. H. Santare, M. Gilbert, S. Cleghorn, and W. B. Johnson, "An experimental investigation of humidity and temperature effects on the mechanical properties of perfluorosulfonic acid membrane," *Mater. Sci. Eng. A*, vol. 425, no. 1–2, pp. 297–304, 2006, doi: 10.1016/j.msea.2006.03.055.

[307] M. B. Satterfield, P. W. Majsztrik, H. Ota, J. B. Benziger, and A. B. Bocarsly, "Mechanical properties of Nafion and titania/Nafion composite membranes for polymer electrolyte membrane fuel cells," *J. Polym. Sci. Part B Polym. Phys.*, vol. 44, no. 16, pp. 2327–2345, 2006, doi: 10.1002/polb.20857.

[308] P. W. Majsztrik, A. B. Bocarsly, and J. B. Benziger, "Viscoelastic response of nafion. effects of temperature and hydration on tensile creep," *Macromolecules*, vol. 41, no. 24, pp. 9849–9862, 2008, doi: 10.1021/ma801811m.

[309] P. Zolliker, M. Shalaby, E. Söllinger, E. Mavrona, and E. Hack, "Real-time high resolution thz imaging with a fiber-coupled photo conductive antenna and an uncooled microbolometer camera," *Sensors*, 2021, doi: 10.3390/s21113757.

[310] R. A. Mensah *et al.*, "The eggshell membrane: A potential biomaterial for corneal wound healing," *J. Biomater. Appl.*, vol. 36, no. 5, pp. 912–929, 2021, doi: 10.1177/08853282211024040.

[311] S. Kudłacik-Kramarczyk *et al.*, "Investigations on the impact of the introduction of the Aloe vera into the hydrogel matrix on cytotoxic and hydrophilic properties of these systems considered as potential wound dressings," *Mater. Sci. Eng. C*, 2021, doi: 10.1016/j.msec.2021.111977.

Appendix A

Adequate data acquisition processing is essential to terahertz systems and experiments. This Appendix outlines the Matlab code listings for data extraction and processing used in this Dissertation.

A.1. Water quantification in PEMs

The following Matlab code extracts the frames from a terahertz video, estimates the water weight in each pixel, and adds up all individual pixels for the total membrane water weight. Additionally, it provides the gravimetric measured water weight in the membrane.

```
% Water quantification in PEMs %

%----------------------------------%

%       By: Decio Alves de Lima     %
%       Date: 10 October 2018       %

%----------------------------------%

clc;
close all;
clear all;

% Measured weight calculations
% ===================================

mw_dry = 351.829 % Dry membrane weight (g)

mw = xlsread('mw.xlsx',1); % Loading data spreadsheet
mw_sampled = mw(1:490:end); % 1 min sub sampling
mw_water = 1000*(mw_sampled-mw_dry) % Membrane water weight (mg)

% Terahertz water weight estimations
% ====================================

fps = 23; % Camera framerate (Hz)

v1 = VideoReader('thzvideo.avi'); % Loading terahertz camera video
v2 = read(v1); % Reading the video frames
v3 = v2(:,:,:,1:fps*60:end); % 1 min sub sampling

nframes = size(v3,4); % Number of frames
vheight = get(v3,'Height'); % Number of pixels in Y direction
vwidth = get(v3,'Width'); % Number of pixels in X direction

% Pre-allocating for speed
frames_raw = zeros(vheight,vwidth,nframes);
frames_resized = zeros(16,16,nframes);


% Video frame extraction loop
for i = 1:nframes

    frames_aux = im2double(rgb2gray(v3(:,:,:,i))); % Converting frames from RGB
matrix to grayscale, double precision values
    frames_raw(:,:,i) = frames_aux; % Storing converted frames
    frames_resized(:,:,i) = imresize(frames_raw(:,:,i),...
```

```
        [size(frames_resized,1),size(frames_resized,2)]); % Resizing to frames to
correct size

end

% Water weight calculations
L = 70; % Membrane characteristic dimension (mm)
aout = L^2; % Membrane area (mm2)
alfa = 11; % Absorption coefficient of liquid water at 100 GHz (mm-1)
rho = 1; % Liquid water density (mg mm-3)
pix = 1.5; % Pixel size (mm)
npix = 14; % Number of pixels considered on X and Y directions
apix = pix^2; % Single pixel area (mm2)
ain = (pix*npix)^2 % 14x14 pixel area (mm2)

ew_dry = load('dry membrane.dat'); % Matrix corresponding to terahertz image of
dry membrane

% Calculation loop
for j = 1:nframes

    ew_aux = sum(sum(abs(-
((log(frames_resized(2:15,2:15,j)./ew_dry(2:15,2:15,1)))./alfa)...
        .*rho.*apix.*(aout/ain)))); % Terahertz estimated water weight (mg)
    ew(1,j) = ew_aux; % Storing calculated values

end
```

A.2. Flooding observations in operating PEMFCs

The following Matlab code extracts the frames from a terahertz video, generates difference images and plots them with Gouraud shading.

```
% Flooding observations in an operating PEMFC %

%-----------------------------------%

%       By: Decio Alves de Lima     %
%       Date: 28 October 2020       %

%-----------------------------------%

clc;
close all;
clear all;

% Terahertz image processing (differencing and Gouraud shading)
% ====================================

fps = 23; % Camera framerate (Hz)

v1 = VideoReader('thzvideo.avi'); % Loading terahertz camera video
v2 = read(v1); % Reading the video frames
v3 = v2(:,:,:,1:fps*60:end); % 1 min sub sampling
```

```
nframes = size(v3,4); % Number of frames
vheight = get(v3,'Height'); % Number of pixels in Y direction
vwidth = get(v3,'Width'); % Number of pixels in X direction

% Pre-allocating for speed
frames_raw = zeros(vheight,vwidth,nframes);
frames_resized = zeros(16,16,nframes);


% Video frame extraction loop
for i = 1:nframes

    frames_aux = im2double(rgb2gray(v3(:,:,:,i))); % Converting frames from RGB
matrix to grayscale, double precision values
    frames_raw(:,:,i) = frames_aux; % Storing converted frames
    frames_resized(:,:,i) = imresize(frames_raw(:,:,i),...
        [size(frames_resized,1),size(frames_resized,2)]); % Resizing to frames to
correct size

end

% Differencing
diff = frames_resized(:,:,1) - frames_resized; % Frame matrix as difference images

% Plotting images with Gouraud shading
pcolor(diff(3:10,:,68))
set(gca,'ydir','reverse','linewidth',10,'fontname','times new
roman','fontsize',20,'fontweight','bold')
colormap 'jet', caxis([0 1]), h = colorbar, h.location = 'southoutside'
xlabel('x coordinate'), ylabel('y coordinate'), ylabel(h, 'THz intensity
(a.u.)','fontsize',20,'fontweight','bold')
shading interp % Gouraud shading
```